Reconstruction of microturbulence wave number spectra from radial correlation reflectometry data

Natalia Kosolapova

Université de Lorraine
Collegium Sciences et Technologies
Ecole doctorale EMMA

Ioffe Physical-Technical Institute
of the Russian Academy of Sciences
Division of Plasma Physics,
Atomic Physics and Astrophysics
High Temperature Plasma Physics Laboratory

Thèse

présentée pour l'obtention du titre de

Docteur de l'Université de Lorraine

en Physique

par **Natalia KOSOLAPOVA**

Recontruction du spectre en nombre d'ondes radiaux à partir des données de la réflectométrie de corrélation radiale

Soutenance publique le **16 Novembre 2012**

Membres du Jury :

Rapporteurs :	Dr. Victor BULANIN	SPbSPU, Saint-Petersburg, Russie
	Dr. Dominique GRESILLON	CNRS, Palaiseau, France
Examinateurs :	Dr. Alexey POPOV	Ioffe Institute, Saint-Petersburg, Russie
	Dr. Michael IRZAK	Ioffe Institute, Saint-Petersburg, Russie
	Dr. Roland SABOT	CEA, Saint-Paul-lès-Durance, France
Directeur de thèse :	Pr. Stéphane HEURAUX	Institute Jean Lamour, Nancy, France
Co-directeur de thèse :	Pr. Evgeniy GUSAKOV	Ioffe Institute, Saint-Petersburg, Russie

Institute Jean Lamour UMR 7198 CNRS
Laboratoire de Physique des Milieux Ionisés et Applications
Faculté des Sciences & Techniques - 54500 Vandœuvre-lès-Nancy

Université de Lorraine
Collegium Sciences et Technologies
Ecole doctorale EMMA

Ioffe Physical-Technical Institute
of the Russian Academy of Sciences
Division of Plasma Physics,
Atomic Physics and Astrophysics
High Temperature Plasma Physics Laboratory

Thesis

presented for obtaining the title of

Doctor of the University of Lorraine

in Physics

by **Natalia KOSOLAPOVA**

Reconstruction of microturbulence wave number spectra from radial correlation reflectometry data

Public defense on the **16th of November 2012**

Members of the Jury :

Referees :	Dr. Victor BULANIN	SPbSPU, Saint-Petersburg, Russia
	Dr. Dominique GRESILLON	CNRS, Palaiseau, France
Examinators :	Dr. Aleksey POPOV	Ioffe Institute, Saint-Petersburg, Russia
	Dr. Mikhail IRZAK	Ioffe Institute, Saint-Petersburg, Russia
	Dr. Roland SABOT	CEA, Saint-Paul-lès-Durance, France
Supervisor :	Pr. Stéphane HEURAUX	Institute Jean Lamour, Nancy, France
Co-Supervisor :	Pr. Evgeniy GUSAKOV	Ioffe Institute, Saint-Petersburg, Russia

Institute Jean Lamour UMR 7198 CNRS
Laboratoire de Physique des Milieux Ionisés et Applications
Faculté des Sciences & Techniques - 54500 Vandœuvre-lès-Nancy

Natalia Kosolapova

email : n.kosolapova@mail.ioffe.ru

Nancy, France
November 16, 2012

Reconstruction of microturbulence wave number spectra from radial correlation reflectometry data

Summary: Turbulence is supposed to be the main source of anomalous transport in tokamaks which leads to loss of heat much faster than as it is predicted by neoclassical theory. Development of plasma turbulence diagnostics is one of the key issues of nuclear fusion to control turbulent particles and energy transport in a future fusion power station. Diagnostics based on microwaves scattered from plasma attract attention of researchers as non-disturbing and requiring just a single access to plasma. The phase of the reflected wave contains information on the position of the cut-off layer and density fluctuations. Correlation reflectometry is now a routinely used technique providing information on plasma microturbulence. Although the diagnostics is widely spread data interpretation remains quite a complicated task. Thus, it was supposed that the distance at which the correlation of two signals received from plasma is suppressed is equal to the turbulence correlation length. However this approach is incorrect and introduces huge errors to determined plasma microturbulence parameters.

The aim of this thesis is to develop an analytical theory, to give a correct interpretation of radial correlation reflectometry (RCR) data and to provide researchers with simple formulae for extracting information on microturbulence parameters from RCR experiments. Numerical simulations based on the theory prove applicability of this theoretical method and give an insight for experimentalists on its capability and on optimized diagnostic parameters to use. Furthermore the results obtained on three different machines are carefully analyzed and compared with theoretical predictions and numerical simulations as well.

Keywords: Tokamaks – Plasmas – Turbulence – Reflectometry – Correlation

Recontruction des spectres microturbulence en nombre d'ondes à partir des données de la réflectométrie de corrélation radiale

Résumé : La turbulence est supposée être la source principale du transport anormal dans les tokamaks, qui conduit à la perte de chaleur beaucoup plus rapidement que celui prédit par la théorie néoclassique. Développement de diagnostics dédiés à la caractérisation de la turbulence du plasma est l'un des principaux enjeux de la fusion nucléaire pour contrôler les flux de particules et de transport d'énergie de la centrale électrique de fusion avenir. Les diagnostics basés sur la diffusion des micro-ondes induite par le plasma ont focalisé l'attention des chercheurs comme outils non perturbants, et nécessitant seulement un accès unique de faible encombrement au plasma. Le principe de base est lié à la phase de l'onde réfléchie qui contient des informations sur la position de la couche de coupure et les fluctuations de densité. La réflectométrie corrélation considérée ici, maintenant couramment utilisée dans les expériences, est la technique fournissant de l'information sur le plasma microturbulence. Bien que le diagnostic soit largement répandu l'interprétation des données reste une tâche assez compliquée. Ainsi, il a été supposé que la distance à laquelle la corrélation des deux signaux reçus à partir du plasma est supprimée est égale à la longueur de corrélation de turbulence. Toutefois, cette approche est erronée et introduit des erreurs énormes sur l'évaluation des paramètres de la microturbulence du plasma.

L'objectif de cette thèse fut d'abord le développement d'une théorie analytique, puis de fournir une interprétation correcte des données de la réflectométrie de corrélation radiale (RCR) et enfin d'offrir aux chercheurs des formules simples pour extraire des informations sur les paramètres de turbulence à partir d'expériences utilisant la RCR. Des simulations numériques basées sur la théorie ont été utilisées pour prouver l'applicabilité de la méthode théorique, pour donner un aperçu aux expérimentateurs sur ses capacités et pour optimiser les paramètres du diagnostic lors de son utilisation en fonction des conditions de plasma. De plus, les résultats obtenus sur trois machines différentes sont soigneusement analysés et comparés avec les prédictions théoriques et des simulations numériques.

Mots clés : Tokamaks – Plasmas – Turbulence – Spectroscopie de réflectance – Corrélation

Определение спектров микротурбулентности по данным радиальной корреляционной рефлектометрии

Аннотация: Турбулентность считается основной причиной аномального переноса в токамаках, что приводит к потере тепла намного быстрее, чем это предсказывает неоклассическая теория. Развитие диагностики турбулентности плазмы с целью контроля турбулентных частиц и переноса энергии в будущей термоядерной электростанции является одной из основных задач термоядерного синтеза. Диагностики, основанные на отражении микроволн, привлекают внимание исследователей как невозмущающие плазму и требующие только одного доступа к плазме. Фаза отраженной волны содержит информацию о позиции отсечки и флуктуациях плотности. Корреляционная рефлектометрия в настоящее время – повсеместно используемая диагностика, дающая информацию о микротурбулентности плазмы. Хотя диагностика широко распространена, интерпретация ее данных остается довольно сложной задачей. Так, предполагалось, что расстояние, на котором корреляция двух сигналов, принятых из плазмы, падает в *e* раз, эквивалентно корреляционной длине турбулентности. Однако, этот подход неверен и приводит к большим ошибкам в определении параметров плазмы.

Цель этой диссертации – разработать аналитическую теорию и метод, позволяющий корректно интерпретировать данные радиальной корреляционной рефлектометрии (РКР), вывести простую формулу для определения параметров микротурбулентности из РКР экспериментов. Численное моделирование, основанное на теории, подтверждает применимость данного теоретического метода и дает представление экспериментаторам о его возможностях и оптимальных экспериментальных параматрах. Более того, результаты, полученные на трех различных машинах, детально проанализированы и были сопоставлены с теоретическими выкладками и численным моделированием.

Ключевые слова: Токамак – Плазма – Турбулентность – Рефлектометрия – Корреляция

Contents

Chapter I

Introduction

In this Chapter we give a short overview of world energy resources and estimate the future energy needs of the world. The most reliable future energy source, nuclear fusion, is briefly surveyed. One of the ways to produce energy from fusion – magnetic confinement – and the tokamak, the most likely device for the future power station are reviewed. We also describe the impact of anomalous transport caused by microturbulence on the fusion device performance and discuss advantages and disadvantages of contemporary turbulence diagnostics. We conclude the Chapter I by describing the scope of this work.

1.1. The world energy problem

As the population of the world has passed the 7 billion mark and continues to grow more than linearly in time [1], the demand for energy is becoming an ever more critical challenge. At present day the world annual primary energy (before any conversion to secondary forms of energy) consumption is about 15TWyr [2]. The World Energy Council [3] projects that by the year 2050 the world wide energy demand will be double its present level. Therefore in the 21st century the prevalent task is to satisfy the need for new long-term sources of energy.

About 90% of energy consumption is satisfied nowadays by burning fossil fuels such as coal, natural gas, and crude oil [4, 5]. These sources are not considered environment friendly for creating air pollution due to the release of gigantic quantities of CO_2.

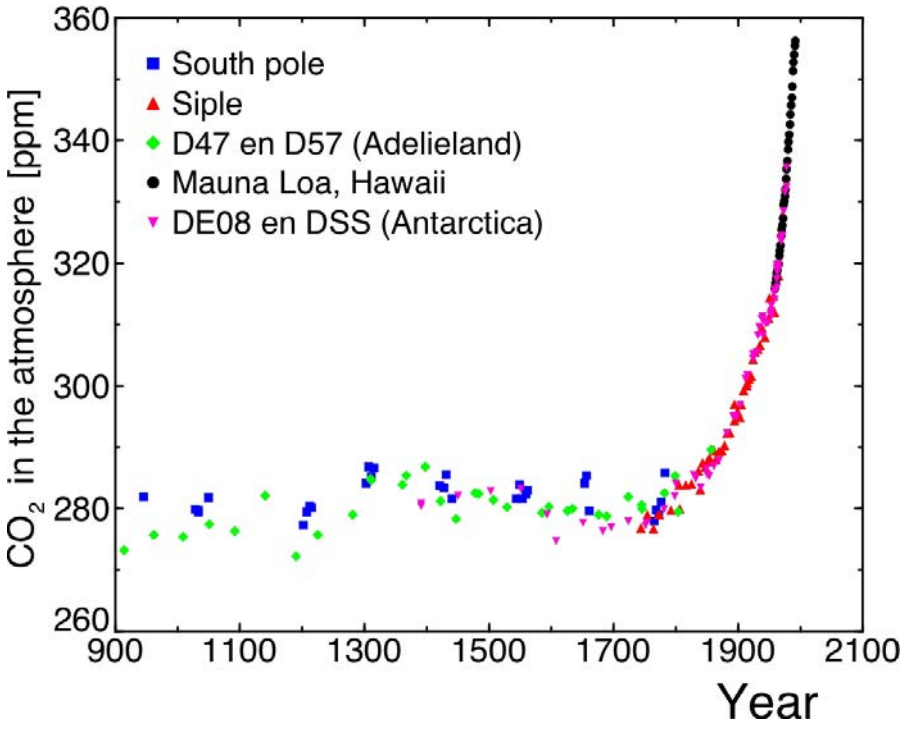

Figure 1.1. Evolution of the CO_2 concentration in the atmosphere. The level of CO_2 has increased rapidly during the last 200 years. Data points are measurements on air bubbles entrapped in Antarctic ice cores. Ice core data overlap nicely with the atmospheric record taken at Manua Loa, Hawaii since 1958 [5, 6].

CO_2 is a greenhouse gas, a higher concentration of it in the atmosphere leads to a continuous increase of the world's average temperature during the two last centuries, from the beginning of industrialization in the 19th century when steam engines have been invented (see figure 1.1.). In the year 2008 the CO_2 concentration has reached the value of $\approx$385ppm and continues to grow [5]. Consequently, this changes the ecosystem in a very short geological timescale what is a very risky geophysics experiment. Moreover, at the current rate of

consumption the world's stock of oil will end in the nearest 40-50 years, of natural gas in 60-70 years. The estimated source of coal is enough for next 250 years however this won't satisfy the world's future energy demand [2, 4, 5].

The first alternative to burning fossil fuels is renewable energy sources, among them are: solar heating, ocean thermal, wind, waves, hydro electricity, tidal power, geothermal heat, biofuel, wood, etc. Currently the contribution of this kind of sources to the world primary energy production is only about 1.3% [4]. The most effective are considered to be solar heating, wave power and hydroelectricity. Unfortunately the exploitation of renewables is limited by natural conditions at the exact location. Renewable energy sources do not directly produce CO_2; the emission of greenhouse gases is released in life-cycle and is indirect. Hence the use of land and indirect emissions are the two negative aspects of renewables which should not be forgotten. Although these non-fossil energy sources are large and inexhaustible they have only limited potential.

The second alternative is nuclear energy (fission and fusion). Nuclear power in the form of fission produces large amounts of inexpensive fuel. Unfortunately it is not favorable as well due to the highly radioactive waste created and not stored properly. In addition, known uranium (U-235) sources will be run out in 50-80 years [7]. It could be stretched by extracting uranium from seawater or by transformation of non-fissile elements to fissile elements (breeder reactions using U-238 and Th) however the safety and environmental problems overbalance.

Nuclear fusion is the youngest and less developed energy source nevertheless it promises to produce safe, environment friendly and inexhaustible energy. This should be the best solution of the staggering task to develop new energy source for mankind.

1.2. Nuclear fusion: energy source for the future

The idea of controlled thermonuclear fusion appeared in the middle of 20th century. Basic principles were borrowed from the most famous thermonuclear reactor – the Sun [8, 9]. In the process that powers the Sun the four protons are combined to produce helium, releasing globally energy in three steps:

$$\begin{aligned} p + p &\rightarrow D + e^+ + \nu_e \\ D + p &\rightarrow {}^3_2He + \gamma \\ {}^3_2He + {}^3_2He &\rightarrow {}^4_2He + 2p \end{aligned} \qquad (1)$$

The idea to realize controlled nuclear fusion on Earth was evoked by analogy with solar fusion production. However it is impossible to reproduce solar conditions on Earth. The probability of the fusion reaction is too small due to extremely low value of the proton-proton cross section reaction [10] and is compensated by space scales of Sun and other stars. By looking

at the cross sections of fusion reaction (see figure 1.2.), on Earth the least difficult fusion reaction is between the hydrogen isotopes deuterium D (the stable isotope of hydrogen with a nucleus consisting of one proton and one neutron) and tritium T (the radioactive isotope of hydrogen with a nucleus of one proton and two neutrons):

$$^{2}D + {}^{3}T \rightarrow {}^{4}He(3.5MeV) + n(14.1MeV) \tag{2}$$

The products of the reaction are neutral helium which carries one third of the result energy and high energy neutron. The energy of neutron can be converted into heat. Other possible candidates for nuclear fusion are:

$$\begin{aligned} {}^{2}D + {}^{2}D &\rightarrow {}^{3}He(0.82MeV) + n(2.45MeV) \\ {}^{2}D + {}^{2}D &\rightarrow {}^{3}T(1.01MeV) + {}^{1}H(3.02MeV) \\ {}^{2}D + {}^{3}He &\rightarrow {}^{4}He(3.6MeV) + {}^{1}H(14.7MeV) \end{aligned} \tag{3}$$

The cross sections of these reactions are shown in figure 1.2. The D-T reaction (2) has the highest cross section at lowest temperature and is easier to be realized. Usually the D-T reaction is accompanied by side reactions, the most important of which are D-D and T-T reactions however these reactions could be neglected due to small fusion cross section.

The energy production of reaction (2) using deuterium containing in 1l of water (33 mg) is equal to that of 260l of gasoline. Deuterium can be cheaply extracted from ordinary water. Tritium is a radioactive isotope of hydrogen and has a rather short half-life about 12.3 years [7] and does not exist in nature. It can be produced as a product of nuclear reaction between neutrons produced in D-T reaction (2) and lithium [7] which is like deuterium a widely available element [11]. Thus, sources for nuclear fusion present on Earth seem to be inexhaustible.

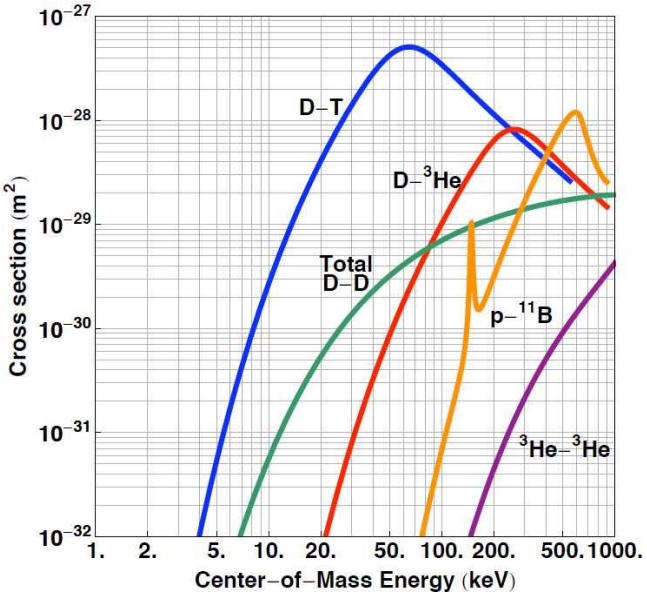

Figure 1.2. Cross sections versus center-of-mass energy for key fusion reactions [7, 12].

To launch the nuclear reaction in Earth conditions we need to heat atoms to high enough temperatures. During this process electrons separate from nuclei and the gas turns into plasma, the fourth state of matter. The term "plasma" was introduced 80 years ago by I. Langmuir to describe the charge-neutral part of a gas discharge [13]. It is a high energy electrically charged mixture of ions and electrons. It is quasi neutral if the scale of plasma system is much larger than Debye radius [14] and influenced by electric and magnetic fields.

Plasma is by far the most common form of matter in the Universe. It makes up over 99% of the visible universe. Stars, stellar and extragalactic jets, and the interstellar medium are examples of astrophysical plasmas. In our solar system, the Sun, the interplanetary medium, magnetospheres and ionospheres of the Earth and other planets, as well as ionospheres of comets and certain planetary moons all consist of plasmas. While plasma is the most abundant phase of matter in the Universe, on Earth it only occurs in a few limited places. It appears naturally only in lightning and the aurora [14]. Plasma can also be observed in welding, electric sparks and inside fluorescent lamps. In nuclear fusion plasma is used as a fuel for thermonuclear energy production.

To get energy from fusion, plasma is heated to very high temperatures. It is necessary to reach firstly a point where plasma temperature can be maintained against the energy losses solely by the α-particle heating. A "steady state" is achieved with equal external adsorbed power P_{ext} and fusion power produced P_{fus}, this is called "breakeven". In this case the power enhancement factor $Q = P_{fus}/P_{ext} = 1$. If it is possible to turn off the external heating, $P_{ext} = 0$ (or $Q = \infty$), the ignition is achieved and the reaction becomes self-sustaining [16].

The requirement for the plasma burn to be self-sustaining is called Lawson criterion [17]. The product $n_e\tau_E^*$, where n_e is the peak plasma electron density and τ_E^* is the global energy confinement time, is a measure of quality of the plasma confinement. The so-called "fusion product" (or "triple product") $n_e\tau_E^*T$ is also widely used for characterizing the performance of fusion devices. It combines requirements on the two quantities, $n_e\tau_E^*$ and temperature, which both have to be large for ignition, into a single quantity. It is the function of the temperature only. For ideal conditions at the minimum the criterion takes a form [7]:

$$n_e\tau_E^*T \simeq 3\cdot 10^{21} m^{-3} keVs \tag{4}$$

Several ways to achieve the above conditions exist, mainly inertial fusion that uses inertia of the pellet [18-20] and magnetic fusion that exploits magnetic fields to confine plasma [7, 21], and a wide variety of other fusion concepts developed over the years as well. The magnetic confinement is realized in several types of fusion devices, the two main of them are stellarator, firstly proposed by L. Spitzer in 1951 [22], and tokamak briefly reviewed in this thesis.

1.3. The tokamak

Tokamak (from Russian "токамак", "ТОроидальная Камера с Магнитными Катушками", – "toroidal camera with magnetic coils") is the predominant device in thermonuclear fusion. It is the earliest fusion device which was firstly proposed by I. Tamm and his former postgraduate student A. Sakharov in 1950 [23-26].

Principal scheme of a tokamak is shown in figure 1.4. It is a toroidal device surrounded by magnetic coils. The primary transformer circuit is situated in the center of toroidal camera; plasma itself forms the secondary winding of the transformer. The poloidal magnetic field, created by a toroidal current I_p flowing through plasma, adds a vertical component to the magnetic field, giving the magnetic field throughout the vessel a twist. This configuration imposes to the particles that have drifted towards the outside of the ring to go back into the centre, preventing the plasma from escaping. Plasma is heated by the toroidal current so-called Ohmic heating however it is not enough to reach Lawson criterion and additional heating is required [27-29].

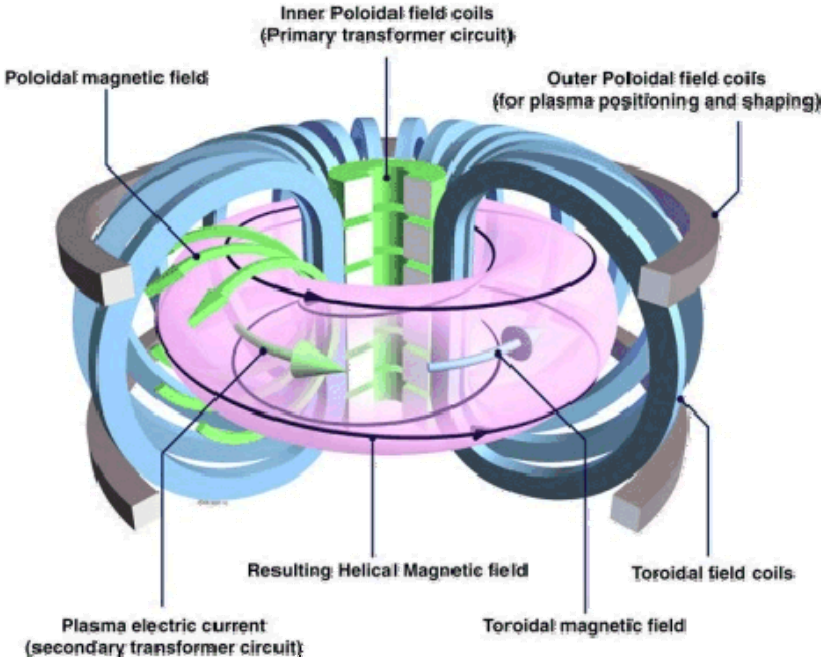

Figure 1.4. Schematic diagram of a tokamak [30].

In 1958 the first machine T-1 started in USSR. In 1968 T-3 tokamak has reached the temperature of plasma of 10 million degrees and tokamaks became the most spread thermonuclear machines in the world [26].

At present time there are more than 200 of tokamaks in the world [31]. Mostly it is experimental devices focused on a quite narrow nuclear task. The most famous in Russia are T-

10 (Kurchatov Institute, Moscow) [32], FT-2, Tuman, Globus-M (Ioffe Institute, Saint-Petersburg) [33]. In USA the NSTX in Princeton and DIII-D in San-Diego are the most explored. In Europe the largest tokamaks are JET and MAST in Culham, UK [30], and Tore Supra in Cadarache, France [34] which utilizes superconducting coils.

A drawback of the tokamak concept is that it has to operate in pulsed mode. A tokamak needs very strong toroidal fields and the strong currents flowing through the magnetic coils generate a lot of heat to increase the plasma current induced by an increasing current in the poloidal coils. A fusion power plant based on the tokamak design will only operate efficiently if it employs superconducting magnet coils. One of the first tokamaks using superconducting coils are EAST, an experimental superconducting tokamak, situated in eastern China [35] and KSTAR [36] launched in 2008 in South Korea. JT-60 has been operating in Japan until 2010 when it was dissassembled to be upgraded to JT-60SA also equipped with superconducting magnets [37].

Superconducting systems store energy in the magnetic field created by the flow of direct current in a superconducting coil which has been cryogenically cooled to a temperature below its superconducting critical temperature. Tokamaks with superconductor coils are focused on reaching the steady state regime of operation which requires real-time control of transport. These requirements are followed by enhanced need in sensitive diagnostics able to follow the turbulence in time and space. The present thesis is exactly devoted to the developing of such a diagnostics which can be applied to determine plasma turbulence characteristics and may become an element of the real-time control system.

1.3.1. Tokamaks in this work

In this subsection we briefly describe the tokamaks mentioned in this thesis: Tore Supra, FT-2, JET and future nuclear fusion reactor ITER. The results of numerical modeling performed for all these devices are shown in Chapter IV. In Chapter V we discuss the experiments performed at FT-2, Tore Supra and JET tokamaks.

1.3.1.1. Tore Supra

Tore Supra (front view is shown in figure 1.5.) is a large machine (R=2.25m, a=0.72m) with superconducting toroidal magnetic coils (B_t=4.5T) and actively cooled first wall operating since 1988 situated at the nuclear research center of Cadarache, Bouches-du-Rhône in Provence, one of the sites of the Commissariat à l'Énergie Atomique (CEA).

Tore Supra is specialized to the study of physics and technology dedicated to long-duration plasma discharge. It now holds the record of the longest plasma duration time for a tokamak 6

minutes 30 seconds and over 1000 MJ of energy injected and extracted in 2003. It allows to test critical parts of equipment such as plasma facing wall components or superconducting magnets that will be used in its successor, ITER, demonstrating the capability of Tore Supra to run long pulses on a regular basis. A new ITER relevant lower hybrid current drive (LHCD) launcher has allowed coupling to the plasma a power level of 2.7MW for 78s, corresponding to a power density close to the design value foreseen for an ITER LHCD system [38].

As soon as the purpose of Tore Supra is to obtain long stationary discharges, the two major questions are addressed: non-inductive current generation and continuous heat and particles removal. The physics program therefore has two principal research orientations, complemented by studies on magnetohydrodynamic (MHD) stability, turbulence, and transport. The first physics program concerns the interaction of electromagnetic (Lower Hybrid and Ion Cyclotron) waves with the hot central plasma. All or part of the plasma current can be generated in this manner, thus controlling the current density profile. The second physics program concerns the edge plasma and its interaction with the first wall. The originality of Tore Supra is the ergodic divertor, which perturbs the magnetic field at the plasma edge by creating a chaotic magnetic field region, resulting in outfluxes of hot plasma collected on neutralizers. Highly radiative layers have been obtained with this device, while preserving a good particle extraction capacity.

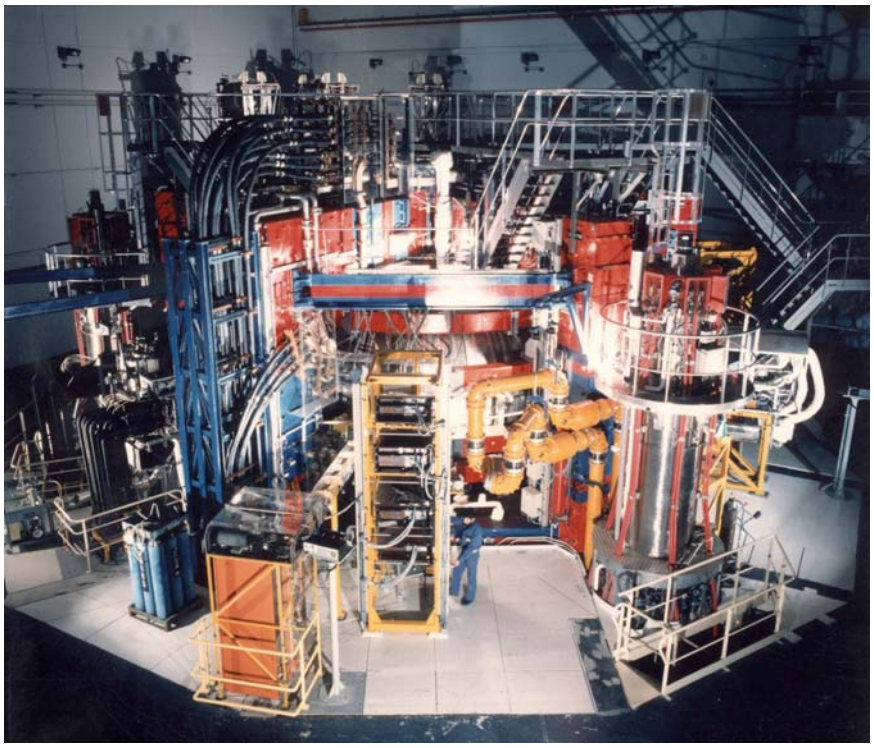

Figure 1.5. Front view of Tore Supra [34].

A detailed description of the machine can be found on the official CEA website [34]. Tore Supra has been stopped for upgrade since 2011.

1.3.1.2. FT-2

The relativelty small (R=55cm, a=8cm) experimental machine FT-2 tokamak (from Russian "Физический Токамак – 2", "Physical Tokamak – 2") is situated in Ioffe Institute, Saint-Petersburg, Russia (front view is shown in figure 1.6.). The tokamak possesses exceptional features: due to the small plasma current (I_P=22kA) the poloidal magnetic field is small compared to the toroidal field (B_t=2.2T). This leads to poloidal Larmor radii that can be several centimetres, of the order of the minor radius. FT-2 also has a large toroidal ripple with the ripple-loss region extending deep into the bulk plasma. With this wide ripple loss region, a large number of trapped particles can suffer a prompt loss even at half minor radius. [39]

After its construction in 1980 many interesting and important results were obtained, in particular, in H-mode physics, lower hybrid (LH) heating [40, 41] and current drive [42] and parametric instability. The auxiliary heating is provided by LH waves [42]. This allows reaching central temperatures of up to 700 eV for electrons and 400 eV for ions. The density of the plasma pulses is sufficiently high to disable any current drive. It turned out that strong heating significantly affects transport processes in plasma. A spontaneous transition into an improved confinement mode has been found during lower hybrid heating (LHH) [44]. The analysis of the effect of the radial electric field on the formation of transport barriers both inside and at the edge of the plasma column has been studied in [41]. It was shown that the profile of the radial electric field can be significantly affected by the combined action of LH heating and an additional rapid increase in the plasma current.

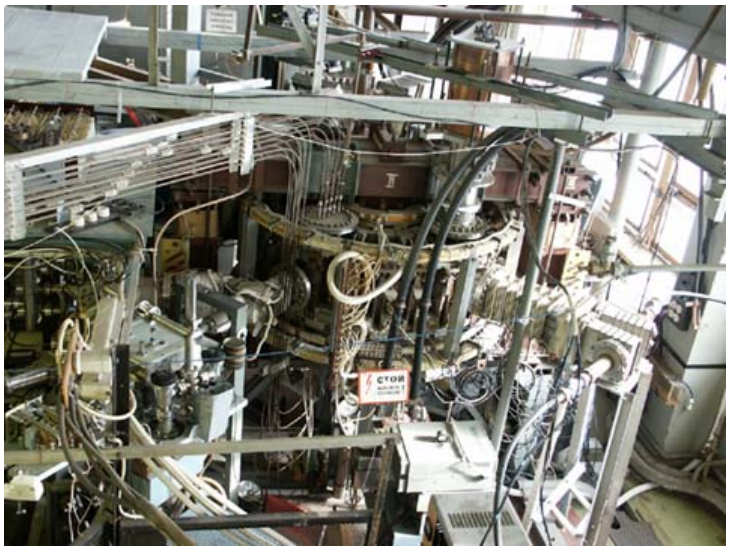

Figure 1.6. FT-2 tokamak, front view [33].

For further information the reader is addressed to the Ioffe Institute official website [33].

1.3.1.3. JET

The Joint European Torus (JET), located at Culham Centre for Fusion Energy (CCFE), UK, is the world's largest (R=3m, a=0.9m) and most powerful (P=16MW) tokamak and the focal point of the European fusion research programme [30, 44]. Designed to study fusion in conditions approaching those needed for a power plant, it is the only device currently operating that can use the deuterium-tritium fuel mix that will be used for commercial fusion power.

Since it began operating in 1983, JET has made major advances in the science and engineering of fusion, increasing confidence in the suitability of the tokamak for future power production. The world's first controlled release of deuterium-tritium fusion power has been realized at JET in 1991 and the world record for fusion power of 16 MW which equates to a measured gain $Q \approx 0.7$ has been reached in 1997.

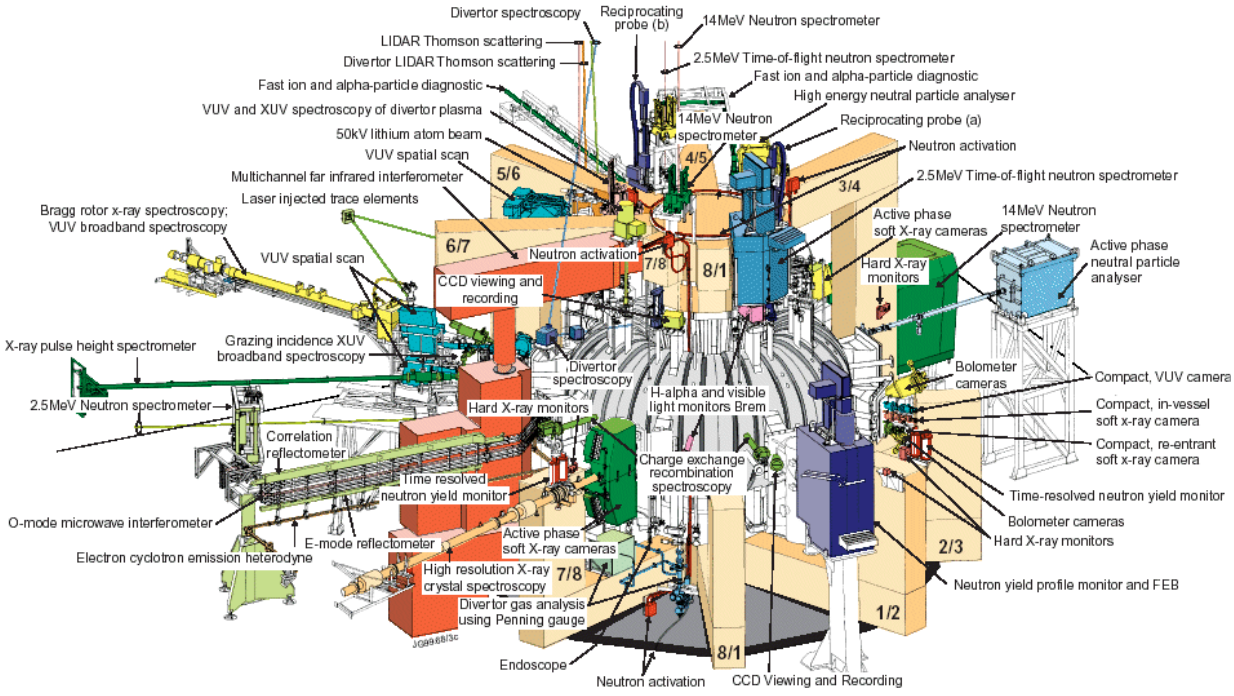

Figure 1.7. Overview of JET diagnostics [44].

In the core of the machine is the vacuum vessel where the fusion plasma is confined by means of strong magnetic fields (B_t=4T) and plasma currents (I_p=5MA). A divertor at the bottom of the vacuum vessel allows escaping heat and gas to be exhausted in a controlled way. Heating at JET is realized by a flexible and powerful plasma auxiliary heating system, consisting of Neutral Beam Injection (NBI, 34MW), Ion Cyclotron Resonance Heating (ICRH, 10MW) and Lower Hybrid Current Drive (LHCD, 7MW). A high frequency pellet injector for plasma refuelling and for ELM pacing studies, a massive gas injection valve for plasma disruption

studies are among JET facilities as well. Remote handling facilities allows advanced engineering work to be performed inside the vacuum vessel without the need for manned access.

An impressive range of diagnostics has been developed over the years for monitoring and analysis of JET operations. JET is surrounded by more than 100 different diagnostic systems (see figure 1.7) and 60 of them are in use during an average experiment capturing up to 18GB of raw data per plasma pulse. The data could be analysed using remote access facilities of CCFE due to the JET facilities are collectively used by all European fusion laboratories under the European Fusion Development Agreement (EFDA).

JET possesses unique capabilities to operate with beryllium plasma-facing components mirroring the material choices of future fusion reactor ITER. In recent years, JET has carried out much important work to assist the design and construction of ITER. After more than 25 years of successful operation, JET is still at the forefront of fusion research and is closely involved in testing plasma physics, systems and materials for ITER. Today, its primary task is to prepare for the construction and operation of ITER, acting as a test bed for ITER technologies and plasma operating scenarios.

For more information please see the EFDA website [44].

1.3.1.4. ITER

Despite the progress continuously achieved on JET and other fusion experiments, it is clear that a larger and more powerful device would be necessary to demonstrate the feasibility of nuclear fusion energy on a reactor scale. This is the purpose of the research and development project ITER (International Thermonuclear Experimental Reactor), an international nuclear fusion research and engineering project [46]. It is the first attempt of the humanity to build the world's largest and most advanced experimental nuclear fusion reactor.

It is beibg built at CEA Cadarache facility in the south of France. The project is the first step on the way from experimental reactors to first DEMO-reactor and finally to the electricity producing power plant. The project is funded and run by seven member entities — the European Union (EU), India, Japan, China, Russia, South Korea and the United States. The history of ITER began in 1985 when the Soviet Union, European Union, Japan and the USA have built the collaboration to develop the hugest tokamak in the world. In 2006 the ITER agreement was officially signed and in 2007 entered into force, the ITER Organization was established.

The schematic view of the tokamak is shown in figure 1.8. The heart of ITER is a superconducting tokamak facility with striking design similarities to JET, but twice the linear dimensions. It will have a plasma volume of around 840m^3. It is designed to produce

approximately 500MW of fusion power sustained for more than 400s. ITER will be the first fusion experiment with an output power higher than the input power.

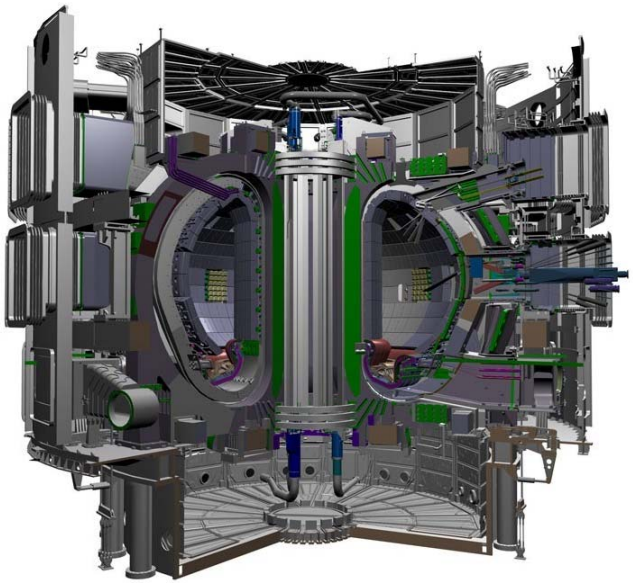

Figure 1.8. ITER schematic view [46].

The ITER program is anticipated to last for 30 years — 10 years for construction, and 20 years of operation. Since 2007 it is technically ready to start construction and the first plasma operation is expected in 2019 [46].

1.3.1.5. Main parameters of machines mentioned in this work

Table 1.1. Main parameters of ITER, JET, Tore Supra and FT-2.

	ITER	JET	Tore Supra	FT-2
Major radius of plasma, m	6.21	3.0	2.25	0.55
Minor radius of plasma, m	2.0	1.25	0.72	0.08
Volume of plasma, m^3	837	155	25	
Plasma current, MA	15	5-7	1.7	0.04
Magnetic field, T	5.3	3.4	4.5	2.2
Duration of pulses, s	~ 300s	10-80	~ minutes	0.06
Type of plasma	D-T	D-D/D-T	D-D	H-H/D-D
Plasma density, m^{-3}	$< 10^{20}$	$< 8 \cdot 10^{19}$	$< 8 \cdot 10^{19}$	$< 6 \cdot 10^{19}$
Plasma density gradient length, m	?	~ 0.1..0.5 [7]	~ 0.4 [47]	~ 0.01 [33]
Thermonuclear power	500MW	50kW/10MW	~ kW	
Q	>10	~ 1	~ 0	~ 0

1.4. Turbulence in fusion plasma

Magnetically confined fusion plasma is a more complex system than the neutral fluid. In plasmas there are at least two fluids, electrons and ions, which cause great number of instabilities. Microinstabilities cause fluctuations of electric and magnetic fields which in its turn cause fluctuations in velocities and particle positions therefore microinstabilities have an influence on transport. Turbulence is induced by incoherent motion appearing from instabilities. It is rather frequent phenomenon in plasma experiments. Observations show that plasma is a fluctuating medium in all its parameters such as density, magnetic field, potential and temperature. Various instabilities that cause turbulence present in various regions of plasma with different characteristics: SOL, edge and core.

Drift wave microturbulence is considered nowadays to be the main source of anomalous transport in tokamak which usually results in loss of heat much faster than it is predicted by neoclassical approach. In figure 1.9. a comparison between neoclassical and turbulence thermodiffusional coefficients is shown.

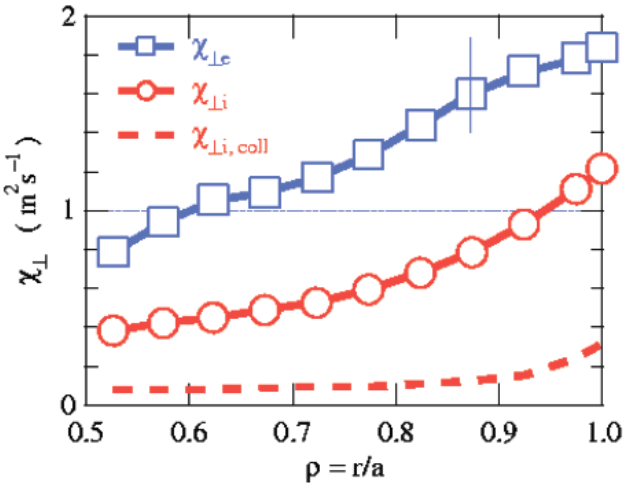

Figure 1.9. Comparison between neoclassical (collisional) thermodiffusional coefficient (dashed line) and anomalous transport *e* (blue squares) and *i* (red circles) coefficient.

Anomalous (turbulence) transport is not fully understood nowadays however it affects the performance of contemporary fusion devices and remains one of the most complex problems in plasma physics. In plasmas, there are two types of fluctuations which can induce anomalous transport: electrostatic and electromagnetic fluctuations.

The central role of microturbulence in anomalous transport has stimulated intensive analytical and experimental investigations. The two types of turbulence cited before have been observed in experiments however there is no exact separation which of the types is responsible for anomalous transport. In recent years studies on plasma turbulence have been focused upon small scale fluctuations [47, 47], long scale fluctuations [49-50] and mesoscale fluctuations such

as zonal flows and streamers [52-54]. The mechanism of turbulence suppression is not well studied yet as well.

In this work, turbulence is considered only through plasma electron density, and only effects and the detection of density fluctuations will be studied.

1.4.1. How fluctuations cause anomalous transport

This subsection is based on works of N. Bretz [56] and D. W.Ross [57, 58]. We shortly recall some theoretical background of anomalous transport formation. A generalized form of plasma transport coefficients and anomalous fluxes of quasilinear type can be written:

$$\Gamma_i = -D_n \frac{\partial n_j}{\partial r} - D_T \frac{\partial T_j}{\partial r} + V n_j + \Gamma_j^{\delta} \tag{5}$$

$$Q_j = -\chi_{jT} n_j \frac{\partial T_j}{\partial r} - \chi_{jn} T_j \frac{\partial n_j}{\partial r} + V n_j T_j + \frac{5}{2} k_b T_j \Gamma_j + Q_j^{\delta} \tag{6}$$

where total fluxes consist of a sum of terms arising from Coulomb collisions (neoclassical transport) and terms arising from fluctuations (anomalous transport) and apply only to transport between closed flux surfaces. In this expression Γ_j and Q_j are ambipolar particle and energy fluxes, respectively, *D* and χ are particle and energy diffusion coefficients, respectively, and *V* is a convection velocity. The subscript *i* refers to particle species (electron or ions) and the superscript δ to fluctuation quantities which may be electrostatic, δE, or magnetic, δB.

In terms of measurable quantities the particle flux is $\Gamma_j^{\delta} = \Gamma_j^{\delta E} + \Gamma_j^{\delta B}$ where the $\vec{E} \times \vec{B}$ driven particle flux has the form $\Gamma_j^{\delta E} = \left\langle \delta n_j \delta \upsilon_r \right\rangle$ with $\delta \upsilon_r = c\, \delta E_\theta / B_\phi$. Similarly, for energy flux, $Q_j^{\delta} = Q_j^{\delta E} + Q_j^{\delta B}$ one has $Q_j^{\delta E} = \frac{3}{2} k_b n_j \left\langle \delta E_\theta \delta T_j \right\rangle / B_\phi + \frac{3}{2} k_b T_j \left\langle \delta E_\theta \delta n_j \right\rangle / B_\phi$. Fluctuating quantities are represented by density, δn, temperature δT, electric field, δE, and magnetic field, δB. Subscripts *r*, θ, and ϕ represent radial, poloidal, and toroidal coordinates $\langle ... \rangle$ denotes an ensemble average, and k_b is Boltzmann's constant. One expects the electromagnetic particle diffusion term to be negligible due to electromagnetic thermodiffusional coefficient which is proportional to parallel velocity is much smaller than electrostatic thermodiffusional coefficient proportional to turbulence correlation time (except at high $\beta = nT / B 2\mu_0$). Many expressions for energy flow due to electrostatic and electromagnetic fluctuations are found in literature.

When both δn_e and δE_θ can be measured simultaneously, the average convection flux $Q_{conv}^{\delta E} = \frac{5}{2} k_b T_e \left\langle \delta E_\theta \delta n_e \right\rangle / B_\phi$ can be calculated directly without further assumptions. However, in

cases of wave scattering, reflectometry, ECE, and BES only δn_e or δT_e can be measured, and additional assumptions about the type of transport process have to be made in order to estimate fluctuation driven fluxes.

Expressions for these fluctuation terms have been derived for a number of specific turbulence processes. One that has been considered in detail is that due to electrostatic drift waves which are driven by gradients in plasma pressure and are typically unstable over significant regions of the plasma cross section. For all electrostatic modes one has $\left(\delta n_e/n_e\right)\sin\psi = e\delta\phi/k_bT_e$ and $k_\theta\delta\phi = -\delta E_\theta$ where ψ is the phase angle between δn_e and $\delta\phi$, plasma potential. Particle flux can be written $\Gamma_j^{\delta E} = n_e\upsilon_{Te}\rho_{ce}\left\langle\left(\delta n_e^2/n_e^2\right)k_\theta\sin\psi\right\rangle$ where $\upsilon_{Te}\rho_{ce} = cT_e/eB_\phi$ with the electron thermal speed $\upsilon_{Te} = \sqrt{k_bT_e/m_e}$, and $\rho_{ce} = \upsilon_{Te}/\omega_{ce}$, the electron cyclotron radius. Theoretical expressions exist for ψ and depend on specific form of turbulence. Limiting expressions can be obtained from additional assumption of strong turbulence, called the mixing length limit: $\delta n_e/n_e \approx 1/k_rL_n << 1$, $\sin\psi \approx 1$, and isotropy: $k_r \approx k_\theta$ where $L_n = -d\left(\ln n_e\right)/dr$, to find:

$$D_n^{\delta E}\left(\text{strong turbulence}\right) \approx \upsilon_{Te}\rho_{ce}(\delta n_e/n_e) \tag{7}$$

Typical conditions of the tokamak core imply that density fluctuation levels of $\delta n_e/n_e \le 1\%$ can lead to a loss that exceeds neoclassical processes. As a result, observations of fluctuations in this range along with drift wave models have been used to estimate core transport [58].

A similar estimate of the particle diffusion coefficient can be made from general random walk arguments using average step size and correlation time across the magnetic field [59]. Thus,

$$D_n^{\delta E}(\text{random walk}) \approx L_{nc}/\tau_{nc} \tag{8}$$

where L_{nc} and τ_{nc} are correlation length and time for density fluctuations across the field.

There are other electrostatic modes that have been investigated as a source of anomalous transport: resistive/neoclassical MHD-like modes driven by field curvature and ripple, viscosity, and plasma current; electromagnetic skin depth modes [61]; and thermal instabilities at the plasma edge [62]. Compared to drift waves MHD-like modes are characterized by longer, and skin depth modes are characterized by shorter wavelengths. However, the accumulation of many past experiments has focused attention on modes that have frequencies and wave numbers characteristic of drift waves in the core of large tokamaks, that is, $f_e \le \omega_e/2\pi \le 20kHz$ and $k_\perp \le 1/\rho_s \approx 5cm^{-1}$.

There are a number of mechanisms that can give rise to anomalous transport. Different mechanisms may dominate at different times and in different regions in plasma. Some modes cause transport and some do not. Experimentally, one sees MHD and turbulent processes

occurring simultaneously. In addition tokamak plasmas can have toroidal and poloidal flows. Instruments must be able to distinguish different modes in moving plasma. Finally, the fluctuation amplitudes themselves are small. In the plasma core typically $\delta n_e/n_e \leq 1\%$. In the edge one has $\delta n_e/n_e \leq 30\%$ (for an example see figure 1.10). Thus, measurement techniques need to be accurate and be able to separate broadband turbulence from significantly higher levels of narrowband, MHD-like, activity.

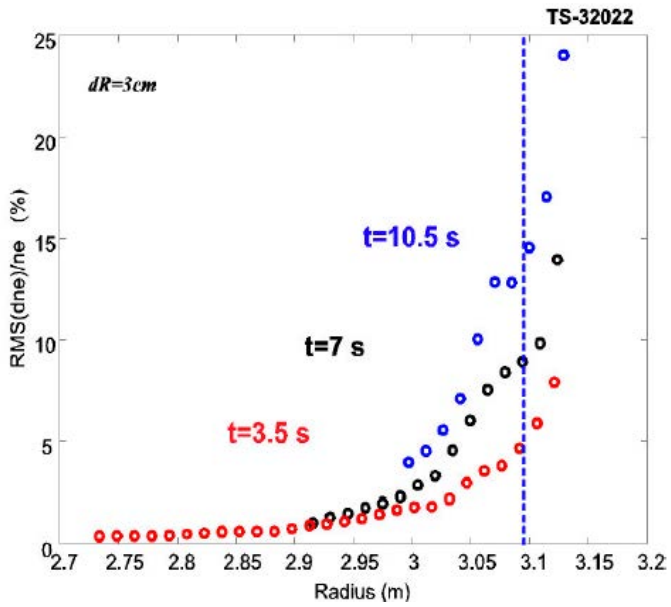

Figure. 1.10. Radial profile of density fluctuations at different density at Tore Supra [63].

Summarizing, to access to physics of turbulence generation one needs to measure fluctuating quantities: density, δn, temperature δT, electric field, δE, potential $\delta\phi$ and magnetic field, δB. In this thesis measurements of δn_e will be discussed.

1.4.2. Bohm or Gyro-Bohm (drift wave) scaling for turbulence

In absence of a fundamental, first-principles turbulence theory, heuristic, mixing length rules are often utilized to estimate size scaling of turbulent transport [64]. This approach invokes a random walk type of picture for diffusive processes using the scale length of turbulent eddies as the step size and the linear growth time of the instability as the step time. It predicts that if the eddy size increases with device size, the transport scaling is Bohm-like, i.e., local ion heat diffusivity is given as:

$$\chi_B = \frac{cT}{eB} \tag{9}$$

On the other hand, if the eddy size is microscopic (on the order of the ion gyroradius), the transport scaling is gyro-Bohm, i.e., local ion heat diffusivity is given as:

$$\chi_{GB} = \rho^* \chi_B \tag{10}$$

where $\rho^* = \rho_i / a$ is ion gyroradius ρ_i normalized by the tokamak minor radius a. There is a long history of confinement scaling studies that have correlated the thermal and/or particle confinement with either Bohm or drift wave scaling laws. The issue is still actively debated as to which transport scaling is to occur under given confinement conditions [65].

1.4.3. Theoretical description of the turbulence wave number spectrum

A better understanding of turbulence transport requires precise comparison between experimental observation and theory. Macroscopic effects give general information on turbulent motion. It is clear that only macroscopic parameters or characteristics without detailed investigation of wave number and frequency spectra and oscillation amplitude do not allow to determine the exact type of turbulent motion which is in charge of given microscopic phenomenon. The turbulence energy spectrum function n_κ^2 describing fluctuation energy repartition over different spatial scales contains information on characters of underlying instabilities and mechanisms involved in energy transfer between different scales. Energy transfer towards smaller scales is called the direct cascade, towards larger scales it is called the inverse cascade. The wave number spectrum is the one of the few quantities that can be measured in a tokamak and allows a highly detailed comparison between experiment and theory [66].

Several models describing turbulence spectral characteristics exist: the dressed test particle model of fluctuations in plasma near equilibrium, 2D fluid turbulence and 3D model [67]. In this work we consider the 2D model as soon as the simplest fluid model in the first approximation gives a good description of turbulence behavior in plasmas.

Well known 3D Kolmogorov's theory of high Reynolds number turbulence (K41 theory) gives the spectrum scaling of the direct cascade $\kappa^{-5/3}$ [68, 69]. However, the behavior of the spectrum is dimensionally dependent. In magnetically confined toroidal plasmas the magnetic field B has two components: a toroidal component B_t produced by toroidal field coils and a poloidal component B_θ produced by a toroidal plasma current. At first approximation plasma turbulence moving perpendicular to the magnetic field can be considered as two-dimensional in poloidal cross section of the tokamak supposing central symmetry. Experimentally, a 2D fluid is realized by a thin but wide layer where movements are mainly horizontal.

In this work Kraichnan-Leith-Batchelor (KLB) model of statistically stationary forced homogeneous isotropic 2D turbulence is considered [69]. This theory predicts existence of two

inertial ranges: an energy inertial range with an energy spectrum scaling of $\kappa^{-5/3}$ and an enstrophy inertial range with an energy spectrum scaling κ^{-3}. The existence of two conserved quantities complicates the construction of theory. Energy and enstrophy are injected into the flow by some external forcing at some intermediate wave number range $\kappa_{\min} < \kappa_f < \kappa_{\max}$. The most of energy transfers towards low κ and forms the inverse cascade, the most of enstrophy transfers downscale towards high κ and is called the enstrophy cascade of direct cascade. Energy dissipates at large scale due to friction between the box size vortices and the boundary, the enstrophy dissipates at small scales due to molecular viscosity [71]. The inverse enstrophy and forward energy cascades are neglected however in reality there are small fractions of upscale enstrophy flux and downscale energy flux.

KLB theory gives the energy scales as:

$$\delta n_\kappa^2 \propto \begin{cases} \kappa^{-5/3}, \kappa_{\min} < \kappa < \kappa_f \\ \kappa^{-3}, \kappa_f < \kappa < \kappa_{\max} \end{cases} \tag{11}$$

Later R. Kraichnan has made logarithmic corrections taking into account non-locality of interactions [72]. In figure 1.11 the schematic wave number spectrum is shown.

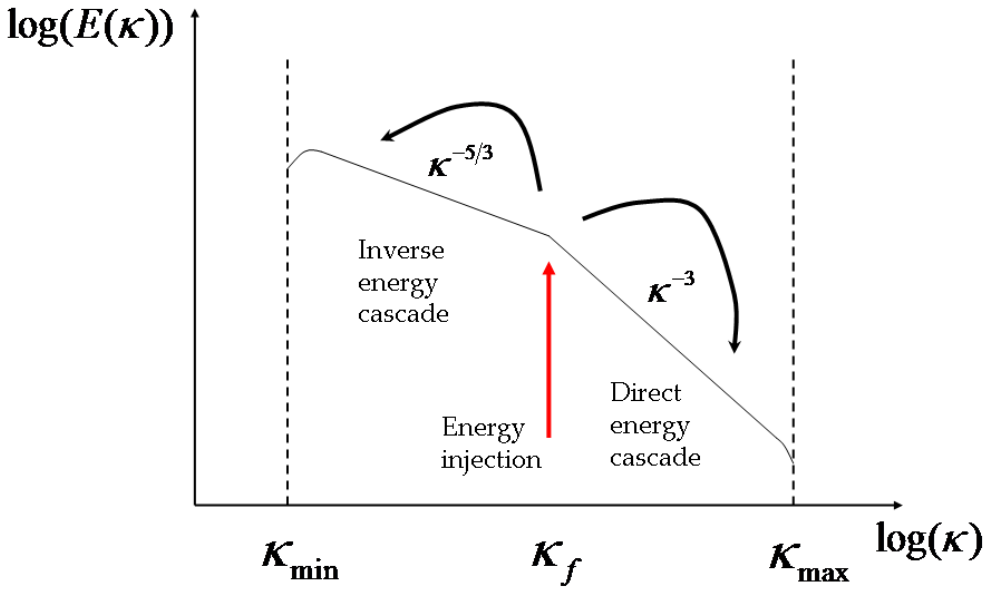

Figure 1.11. Schematic of energy spectrum for dual cascade.

The similarity between fluid and magnetized plasma is limited. Injection appears at various different scales and the development of large-scale structures interacting with the background fluctuations impact the saturated state of turbulence [66]. For example, observations of wave number spectrum show that the spectrum is composed of two power laws at high-k: κ^{-3} and κ^{-7} [47].

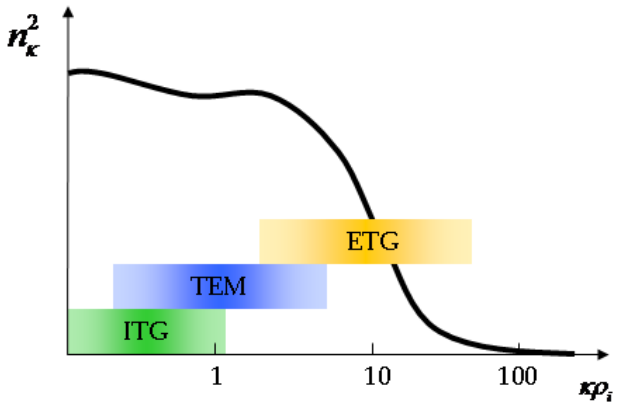

Figure 1.12. The range of poloidal wave numbers covered by ITG, drift-waves, TEM and ETG modes of turbulence. Large scales are dominant.

A large variety of modes can become unstable; they differ in particular by their typical scale. The most common are ion temperature gradient (ITG) mode (typical scale longer than ion Larmor radius $\rho_i \approx 1mm - 1cm$), the trapped electron mode (TEM) also of the same order, the smaller scale electron temperature gradient (ETG) mode (typical scale of the order of electron Larmor radius $\rho_e \approx 10\mu m - 100\mu m$) [47]. The turbulence at the largest scales is believed to be responsible for transport. In figure 1.12 the scale ranges of these instabilities are schematically shown.

1.4.4. Examples of turbulence wave number spectra

Though the theory gives main dependencies in the turbulence wave number spectrum, it could be different from that one shown in the previous subsection. Thus, as it was mentioned, in plasma a lot of processes take place. In numerical simulations there is nothing to do without assumptions. Therefore various shapes of spectra are used in numerical modeling of turbulence.

In one of the first works addressing to the 1D simulations [73] the perturbation of the form of a wave packet located at x_0 with a magnitude δn_0, a spatial period Λ extending over a region characterized by a width Δ:

$$\delta n_e(x) = \delta n_0 e^{-(x-x_0)^2/\Delta^2} \sin\left[2\pi(x-x_0)/\Lambda\right] \tag{12}$$

And the spectrum takes a form:

$$\delta n_\kappa^2 \approx (\pi \delta n_0^2/3)\, e^{-\kappa^2 l_c^2/4} \tag{13}$$

where l_c is the correlation length. This spectrum falls off rapidly with increasing κ and is roughly consistent with theoretical drift wave models and with microwave scattering measurements of density fluctuation spectra in tokamak plasmas [73-76]. The same shape of turbulence spectrum is used in works [77] and [78]. In the second work, another type of localized perturbation has been studied:

$$\delta n(x) = \begin{cases} \delta n_0 \sin[k_f (x - x_f)], \left| x - x_f \right| \le w_f \\ 0, \left| x - x_f \right| > w_f \end{cases} \tag{14}$$

where w_f is the half-width of the perturbation centered around w_f and k_f is the fluctuating wave number.

In [77] in case of spatio-temporal turbulence the spectrum is introduced in the following way:

$$\delta n_e(x) = \delta n_0 g(x) \sum_{j,m} \sin(k_j x + \phi_{xj}) \sin(\omega_m t + \phi_{tm}) \exp(-k_j^2 l_c^2 / 8) \exp(-\omega_m^2 t_c^2 / 8) \tag{15}$$

$g(x)$ accounts for a smooth inhomogeneous distribution of the fluctuation amplitude. The temporal correlation function for a set of samples is also Gaussian, $\exp(-t^2 / t_c^2)$.

Some other kinds of turbulence spectra will be presented and commented in Chapter IV.

1.4.5. Turbulence suppression

In the improved confinement regime (H-mode) [79] cross-field losses of particles and energy are reduced due to transport barriers which are formed by sheared poloidal plasma flows and located close to the plasma edge. The H-mode formation is still not clearly understood as well as turbulence suppression or properties modifications of fluctuations. Some of mechanisms of such an effect are briefly described in this subsection.

1.4.5.1. Radial electric field shear

In 1988 S.-I. Itoh and K. Itoh have introduced the radial electric field E_r into the explanation of the H-mode confinement regime [80] and therefore have shown its importance. A spontaneous bifurcation of E_r nowadays is used as a theoretical model to explain the improved confinement.

The electric field created a fluid like motion is known as $\vec{E} \times \vec{B}$ drift. The $\vec{E} \times \vec{B}$ drift velocity is given by the expression:

$$\vec{\upsilon}_{\vec{E} \times \vec{B}} = \frac{\vec{E} \times \vec{B}}{B^2} \tag{16}$$

The electric field can be determined from the radial force balance:

$$E_r = \upsilon_{\theta,j} B_\varphi - \upsilon_{\varphi,j} B_\theta - \frac{1}{e_j} \frac{dp_j}{dr} \tag{17}$$

where *j* is any plasma species and the last term is often called the diamagnetic contribution to the E_r.

In 1990 Biglari, Diamond and Terry have developed a model showing analytically that a possible turbulence quench mechanism is a sufficiently strong shear in the radial electric field E_r [81]. The BDT model explains H-mode reduced turbulent transport due to accumulated experimental evidence. It shows that the electric field stabilizes nonlinearly turbulent modes in plasma. The model also explains the formation of edge and core transport barriers. The important result of this work is that turbulence suppression does not depend on the sign of E_r or its radial shear ∇E_r. The BDT-criterion for shear decorrelation (when shearing rate exceeds decorrelation time) takes a form:

$$\left|\frac{\nabla E_r}{B_\phi}\right| > \frac{\Delta\omega_t}{k_\theta L_r} \tag{18}$$

where $\Delta\omega_t$ is the turbulent decorrelation frequency, L_r is the radial correlation length, k_θ is the poloidal wave number of turbulence. If the E_r shear is strong, it can drive perpendicular plasma shear flows that break turbulent structures into smaller ones, thus reducing radial correlation lengths and suppressing turbulence.

1.4.5.2. Zonal Flows

Zonal flows (ZFs) are low frequency electrostatic fluctuations with finite radial wave number [54, 55]. Since they are poloidally symmetric, they do not drive radial or cross-field transport. ZFs gain their energy from all types of microinstabilities through $v\nabla v$ - nonlinearity and regulate the amplitude of the latter by shearing them. Since ZFs are electrostatic fluctuations, the caused velocity shear is time varying, however the time scale stays accessible to diagnostics studied in this thesis. The increase in the zonal flow fraction in turbulence contributes to a lessening of anomalous transport. The interaction between zonal flows and drift waves plays an essential role in determining plasma turbulence and transport [54].

1.5. Turbulence diagnostics

The importance of plasma turbulence in plasma magnetic confinement has been clearly shown in the previous subsection. It is a strong motivation for researchers to develop diagnostics to measure fluctuations in tokamaks. Beam Emission Spectroscopy (BES), Heavy Ion Beam Probes (HIBP), Langmuir probes, electromagnetic wave scattering and reflectometry systems are measuring plasma density fluctuations. In this section we shortly discuss advantages and disadvantages of these methods.

Langmuir probes are the oldest and most well described diagnostic [82, 83 and 84]. Probes measure simultaneously electron density n_e, temperature T_e, plasma potential ϕ and their fluctuations. Probes are used routinely to estimate fluctuation driven energy and particle flux in the tokamak edge and the shear layer in diverted plasmas. Application of probes is restricted to the low temperature plasma boundary where the level of fluctuations is significantly high, the impact of impurities is rather noticeable as well; this leaves a lot of questions to researchers. Good spatial resolution and slow time scale due to capacity do not take into account the turbulent flux on the interpretation model as it should be [85].

HIBP are used to measure simultaneously fluctuations of plasma potential and electron density [86-88]. This is a collimated beam of neutrals or singly charged ions which ionizes in plasma producing secondary ions that have orbits larger than the minor radius. HIBP is not as sensitive to high κ fluctuations due to its finite sample volume. There is also uncertainty in radial location measurements. Furthermore, the HIBP systems are complex and rather expensive and do not really permit to have absolute measurement due to lack of knowledge during the particle trajectory.

BES is a technique measuring density fluctuations by observing the light emitted from beam atoms or ions that have been excited by collisions with constituents of the bulk plasma [89]. The detectable fluctuation level is limited by photon statistics, atomic excitation process and beam stability, and due to this fact the absolute value of density fluctuations is not accessible. Wave number spectra in radial and poloidal directions can be acquired from cross correlation measurements in these directions. Unfortunately the diagnostic is rather sensitive to the MHD activity.

Coherent scattering of electromagnetic waves is used to measure properties of electron density autocorrelation function [84]. The diagnostic is based on refractive index principles. The calibration of scattering systems is not straightforward and introduces uncertainty in estimates of electron density fluctuations. The main drawback of the diagnostic is that the frequency tends to be so low that the beam suffers from considerable refraction by the plasma. Also, diffraction limits the minimum beam size obtainable. Moreover, fluctuation wave numbers greater than $2k_i$ are not obtainable so relevant parts of the κ spectrum may not be accessible with low k_i microwaves. Measurements are limited primarily by low spatial resolution at low values of κ and by practical requirements on machine access to sample a variety of plasma locations and κ.

Reflectometry refers to the reflection of an electromagnetic wave from a plasma cut-off where the plasma refractive index vanishes [90, 91]. Fluctuation measurements in the plasma interior using reflectometry are relatively straightforward to perform but rather hard to interpret. The phase delay is most sensitive to density fluctuations located near the reflection layer. However, it is also sensitive to fluctuations along the entire radiation path, and so the

localization of the measurement is not the same as if one were probing an oscillating mirror at the cut-off position. Moreover, standart one channel reflectometry methods provide no wave number resolution.

1.6. Radial correlation reflectometry

On purpose to determine wave number spectrum or at least the turbulence correlation length radial correlation reflectometry (RCR) was proposed. Firstly this method was used for ionosphere [92]. Although the first experiments using microwave reflectometry were carried out many years ago [93, 94] it is only in recent years that the technique has been developed to the point where quantitative information can be routinely obtained on tokamak plasmas. R. Cano and A. Cavallo in 1980 [90] proposed to apply it for tokamaks and first experiments were held on the TFR tokamak using the ordinary mode of propagation in 1985 by F. Simonet [91] and later was widely spread all over the world fusion devices. Nowadays RCR is a widely used method for measuring electron density of plasma and turbulence properties in tokamak [56, 84, 95-97].

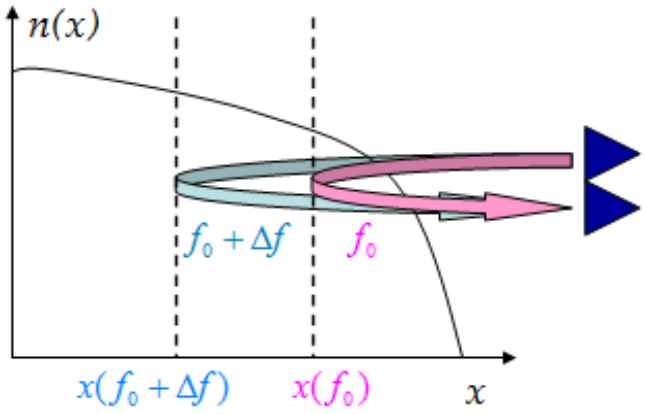

Figure 1.13. Launching the two microwaves to the plasma simultaneously.

In this method microwaves with frequencies f_0 and $f_0 + \Delta f$ are launched simultaneously into plasma along the density gradient and reflected at the cut-off layer (see figure 1.13.). The first frequency f_0 is called "reference frequency" and is fixed; the second "sweeping frequency" $f_0 + \Delta f$ is swept. The coherence decay of the two reflected signals $A_s(f_0)$ and $A_s(f_0 + \Delta f)$ with growing difference of probing frequencies Δf – cross correlation function (CCF) – is studied by such a diagnostic:

$$CCF(\Delta x)=\frac{\left\langle \left(A_s(f_0)-\left\langle A_s(f_0)\right\rangle\right)\left(A_s(f_0+\Delta f)-\left\langle A_s(f_0+\Delta f)\right\rangle\right)^*\right\rangle}{\sqrt{\left\langle \left(A_s(f_0)-\left\langle A_s(f_0)\right\rangle\right)^2\right\rangle\left\langle \left(A_s(f_0+\Delta f)-\left\langle A_s(f_0+\Delta f)\right\rangle\right)^2\right\rangle}} \tag{19}$$

where $\Delta x = x(f_0+\Delta f)-x(f_0)$.

This diagnostic is an attractive alternative to others mentioned before and possesses a wide range of possibilities to measure plasma density profile and its fluctuations [98]. It is often used for fluctuation monitoring in discharges, in particular, anomalous transport suppression studies in better confinement regimes.The diagnostic is not focused only on edge or core measurements and is relatively cost-effective. Technical simplicity, as well as experimental geometry allowing single-port access to plasma, is among its attractive merits. Another advantage of the method is high locality – the sensitivity of the refractive index to changes in electron density is the greatest near the cut-off, so the reflected phase and amplitude variations carry the information on local density fluctuations.

Taking into account that RCR utilizes perpendicular incidence of microwave onto the plasma it is essentially that 1D experimental geometry is less sensitive to 2D effects, compared to Doppler reflectometry [99-101] or poloidal correlation reflectometry [102-104]. The RCR has the benefit of the plasma curvature to reduce the 2D dependencies as it was shown for classical reflectometry [105].

As soon as RCR measures directly the scattering signal and not density fluctuations themselves the diagnostic requires accurate and reasonable procedure of data interpretation. Formerly it was naively supposed that the distance between cut-off positions at which the correlation of two reflectometry signals is suppressed should be equal to the turbulence correlation length, however this assumption is incorrect. It has already been shown in 1D numerical computations performed using the Born approximation performed by I. Hutchinson in [95] that the scattering signal CCF decays spatially much more gradually than the TCCF. This gradual decay of RCR CCF was attributed in [95] to the contribution of small angle scattering off very long scale fluctuations.

Later this observation was confirmed also in full-wave 1D [77] numerical modeling for small level of turbulent density fluctuations (see figure 1.14.). Moreover, a surprisingly high RCR correlation length was observed in experiments [106]. However, no simple theoretical description of this behavior was provided in 1D geometry, nor ways to overcome this difficulty in determining the turbulence correlation length or spectrum.

A complicated analytical treatment of the RCR performed in 2D geometry in linear (Born) approximation for linear plasma density profile and O-mode probing [107] also resulted in the prediction of slow (logarithmic) decay of coherence, which was confirmed by 2D numerical computations [108, 109]. As has been shown in [77, 108] a faster decay of coherence occurs only

at high enough fluctuation amplitude leading in agreement with analytical prediction [110, 111] to strong reflected wave phase modulation.

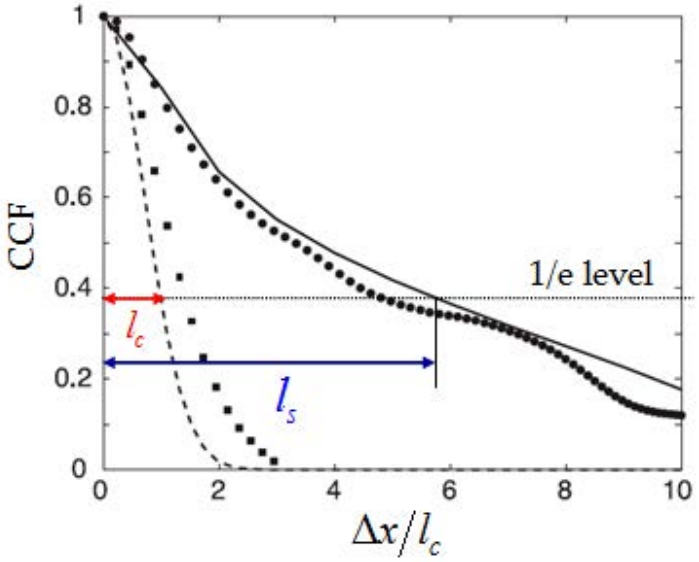

Figure 1.14. Large difference between RCR CCF correlation length l_s and TCCF correlation length l_c in 1D Born approximation full-wave computations [77].

Unfortunately even knowing the problem people are still using the erroneous approach during the last two decades [112]. It is evident that correct RCR data interpretation is needed.

1.7. Scope of this work

In this dissertation deep study of the RCR diagnostic is performed. Addressing firstly to analytical approach we aim to describe the dependency of the scattering signal from plasma on turbulence wave number and further explain the discrepancy between the correlation function of measurement and the fluctuation correlation function in 1D geometry. Moreover, numerical modeling performed in Born approximation is compared to analytical asymptotic expressions of RCR signal and CCF behavior. The relation between turbulence wave number spectrum and signal RCR CCF is proposed and tested in experiment numerical modeling and further in real experiments.

This work is organized as follows: in Chapter II we recall reflectometry basics and describe the theory of RCR. In Chapter III the examples of numerical simulations held for different machines are presented; we also give the insight on experimental setting. Chapter IV presents experimental results obtained on small FT-2 and huge Tore Supra machines. Chapter V summarizes results of the thesis.

Chapter II

Theoretical background of radial correlation reflectometry

In this Chapter we firstly describe propagation of electromagnetic waves in inhomogeneous plasma, reflectometry basics and the way to introduce plasma density fluctuations. Further, the one dimensional theory of radial correlation reflectometry is presented. The analytical expression for the RCR CCF is given. The simple relation between the RCR CCF and the turbulence wave number spectrum is derived. We also present formlue aloowing direct transformations between RCR CCF and TCCF.

2.1. Propagation of electromagnetic waves in plasmas

This section is based on V. L. Ginzburg development in CGS units [92].

Propagation of an electromagnetic wave in a medium is described by Maxwell equations:

$$\nabla \cdot \vec{D} = 4\pi\rho \tag{20}$$

$$\nabla \cdot \vec{B} = 0 \tag{21}$$

$$\nabla \times \vec{E} = -\frac{1}{c}\frac{\partial \vec{B}}{\partial t} \tag{22}$$

$$\nabla \times \vec{H} = \frac{4\pi}{c}\vec{j} + \frac{1}{c}\frac{\partial \vec{D}}{\partial t} \tag{23}$$

Where $\vec{E}$ and $\vec{H}$ are electric and magnetic fields of the wave correspondingly; ρ and $\vec{j}$ are charge and current correspondingly created by external sources related to the polarization $\vec{P}$ in the usual way:

$$\rho = -\nabla \cdot \vec{P} \tag{24}$$

$$\vec{j} = \frac{\partial \vec{P}}{\partial t} \tag{25}$$

These relations enforce charge conservation:

$$\frac{\partial \rho}{\partial t} + \nabla \cdot \vec{j} = 0 \tag{26}$$

In plasma as in any dielectric, the relations between fields and their induction take the following form:

$$\vec{D} = \vec{E} + 4\pi\vec{P} \tag{27}$$

$$\vec{B} = \vec{H} + 4\pi\vec{M} \tag{28}$$

where $\vec{M}$ is magnetization. The linear relation between $\vec{j}$ and $\vec{E}$ is given by Ohm law:

$$\vec{j} = \bar{\sigma}\vec{E} \tag{29}$$

where $\bar{\sigma}$ is the conductivity tensor.

2.1.1. Approximations and restrictions used

To obtain a general description of electromagnetic wave propagation in plasma it is needed to use simplifying hypotheses and approximations.

2.1.1.1. Stationary plasma

Temporal variations of the plasma occur on a time scale considerably bigger than the period of the waves signifying that the plasma is stationary on the wave time reference.

2.1.1.2. Cold plasma approximation

At present, most fusion experiments operate at plasma temperature below 5 keV. Waves traveling at phase velocities close to the speed of light are concerned. In this case the thermal velocity of electrons is much less than the phase velocity $\upsilon_{Te}/\upsilon_{ph} << 1$. Cold plasma approximation is used to describe the propagation of most electromagnetic waves in tokamak plasma. The meaning of the approximation is that thermal motion of particles is neglected comparing to the motion caused by propagating electromagnetic wave [113, 114].

It is also assumed that there is no collisional damping (or Landau damping) on the time scale of plasma electrons as required for cold plasma approximation. Electrons are initially considered at rest, except for movement induced by wave fields.

2.1.1.3. High frequencies

Ion and neutral particle motion is neglected as well due the relation $m_e/m_i << 1$ as soon as high frequency electromagnetic waves $\omega >> \omega_{ci}$ are studied. Only electrons contribute to the plasma dielectric tensor over the time of flight.

2.1.1.4. Anisotropy

We suppose the anisotropy is introduced only by external magnetic field $\vec{B}_0$. In this work inhomogeneous anisotropic plasma is considered where refractive index depends on the propagation direction.

2.1.1.5. Propagationg waves

The electromagnetic wave propagating into plasma is supposed to be monochromatic. It could be described in usual way:

$$\vec{E} \propto \vec{E}_0 \exp(-i\omega t) \tag{30}$$

where $\omega = 2\pi f$ is the microwave angular frequency of the wave. The phase velocity, $\upsilon_{ph} = \omega/k$ gives the rate of propagation of a point of constant phase on the wave. If the wave frequency or amplitude is modulated the wave possesses the group velocity $\upsilon_{gr} = \partial\omega/\partial k$. The dispersion relation $\omega(k)$ contains information on phase and group velocities, propagation region, reflection points, resonance points, damping, wave growth. Another property of the

electromagnetic wave is polarization which is defined by the orientation and phase of the electric field of the wave $\vec{E}$. There are three types of polarization: linear, circular and elliptical.

2.1.1.6. Linear approximation

As soon as restrictions of small-amplitude waves are imposed it is possible to apply linear theory of perturbations. All the perturbations δf of the quantity *f* in this work are assumed to be small as well $\delta f / \langle f \rangle << 1$. This permits to use linear relations to describe wave propagation in plasma knowing that the input power of reflectometer is not able to modify the background plasma parameters.

2.1.2. Propagation in homogeneous plasma

Taking into account approximations introduced in 2.1.1., we consider plane wave propagation in the uniform and homogeneous plasma in external magnetic field $\vec{B}_0$. According to linear approximation we perform Fourier analysis of Maxwell equations. By taking the curl of the eq. (22) and combining it with the eq. (23) and transforming operators $\nabla \to ik$ and $\partial/\partial t \to -i\omega$ we obtain the wave equation (Helmholtz equation):

$$\vec{k} \times (\vec{k} \times \vec{E}) + \frac{\omega^2}{c^2} \overline{\varepsilon} \vec{E} = 0 \tag{31}$$

where $\overline{\varepsilon}$ is the dielectric tensor related to the conductivity as follows:

$$\overline{\varepsilon} = \overline{1} - \frac{4\pi\overline{\sigma}}{i\omega} \tag{32}$$

Eq. (31) can be rewritten in a form:

$$\left(\vec{N}\vec{N} - N^2\overline{1} + \overline{\varepsilon}\right)\vec{E} = 0 \tag{33}$$

where $\vec{N} = \vec{k}\frac{c}{\omega}$ is the refractive index and $k_0 = \frac{\omega}{c}$ the vacuum wave number. Eq. (33) is represented by the following matrix:

$$\begin{pmatrix} \varepsilon_{xx} - N^2\cos^2\theta & -i\varepsilon_{xy} & N^2\cos\theta\sin\theta \\ i\varepsilon_{xy} & \varepsilon_{xx} - N^2 & 0 \\ N^2\cos\theta\sin\theta & 0 & \varepsilon_{zz} - N^2\sin^2\theta \end{pmatrix} \begin{pmatrix} E_x \\ E_y \\ E_z \end{pmatrix} = 0 \tag{34}$$

where θ is the angle between external magnetic field $\vec{B}$ and wave vector $\vec{k}$. This system consists of three scalar equations and possesses a non-zero solution only if the determinant of the matrix is equal to zero. Thus, the dispersion relation is obtained:

$$\det\left|\vec{N}\vec{N} - N^2\overline{1} + \overline{\varepsilon}\right| = 0 \tag{35}$$

The elements of the system (34) are the following:

$$\begin{aligned}
\varepsilon_{xx} &= \varepsilon_{yy} = 1 - \frac{\omega_{pe}^2}{\omega^2 - \omega_{ce}^2} \\
\varepsilon_{xy} &= -\varepsilon_{yx} = -\frac{\omega_{ce}}{\omega}\frac{\omega_{pe}^2}{\omega^2 - \omega_{ce}^2} \\
\varepsilon_{zz} &= 1 - \frac{\omega_{pe}^2}{\omega^2} \\
\varepsilon_{xz} &= \varepsilon_{zx} = \varepsilon_{zy} = \varepsilon_{yz} = 0
\end{aligned} \tag{36}$$

where

$$\omega_{pe} = \sqrt{\frac{4\pi n_e e^2}{m_e}} \tag{37}$$

is the plasma angular frequency and $f_{pe} = \frac{\omega_{pe}}{2\pi}$ is the plasma frequency. And

$$\omega_{ce} = \frac{eB}{m_e c} \tag{38}$$

is the electron cyclotron angular frequency.

2.1.2.1. Perpendicular propagation

In reflectometry experiments in toroidal plasmas electromagnetic waves are usually launched and received with the wave vector $\vec{k}$ perpendicular to the external magnetic field $\vec{B}_0$. In this case two types of waves are possible: "ordinary mode" and "extraordinary mode".

2.1.2.1.1. Ordinary mode (O-mode)

It is a wave with a linear polarization, the electric field of the wave is parallel to the external magnetic field $\vec{E} \parallel \vec{B}_0$ (see figure 2.1.). This mode is not sensible to the magnetic field $\vec{B}_0$. The wave propagates as it was in unmagnetized plasma. In this case the refractive index takes the simplest form:

$$N^2 = 1 - \frac{\omega_{pe}^2}{\omega^2} \tag{39}$$

The refractive index of the wave determines whether the wave will propagate ($N^2 > 0$) or be reflected ($N^2 < 0$). For the ordinary mode the refractive index never reaches the infinity. Thus, the wave propagates in plasma if its frequency is greater than the plasma frequency $\omega > \omega_{pe}$.

The cut-off position is determined by the condition $\omega = \omega_{pe}$. For a given frequency ω it is possible to determine the critical density above which the wave does not propagate anymore:

$$n_c = \frac{m_e \omega^2}{4\pi e^2} \tag{40}$$

2.1.2.1.2. Extraordinary mode (X-mode)

The electric field of this wave is perpendicular to the external magnetic field $\vec{E} \perp \vec{B}_0$ (see figure 2.1.). The propagation of the wave depends not only on the plasma density but on the magnetic field as well. The refractive index takes a form:

$$N^2 = 1 - \frac{\frac{\omega_{pe}^2}{\omega^2}\left(1 - \frac{\omega_{pe}^2}{\omega^2}\right)}{1 - \frac{\omega_{pe}^2}{\omega^2} - \frac{\omega_{ce}^2}{\omega^2}} \tag{41}$$

For the extraordinary wave two cut-off positions take place. The condition for the left (lower) cut-off position is:

$$\omega = \omega_L = \frac{1}{2}\left(-\omega_{ce} + \sqrt{\omega_{ce}^2 + 4\omega_{pe}^2}\right) \tag{42}$$

The condition for the right (high) cut-off is:

$$\omega = \omega_R = \frac{1}{2}\left(\omega_{ce} + \sqrt{\omega_{ce}^2 + 4\omega_{pe}^2}\right) \tag{43}$$

If the refraction index reaches infinity ($N^2 \to \infty$) the extraordinary wave will be absorbed at the upper hybrid resonance:

$$\omega = \omega_{UH} = \sqrt{\omega_{ce}^2 + \omega_{pe}^2} \tag{44}$$

The extraordinary wave propagates if $N^2 > 0$, i.e. $\omega_L < \omega < \omega_{UH}$ and $\omega_R < \omega$.

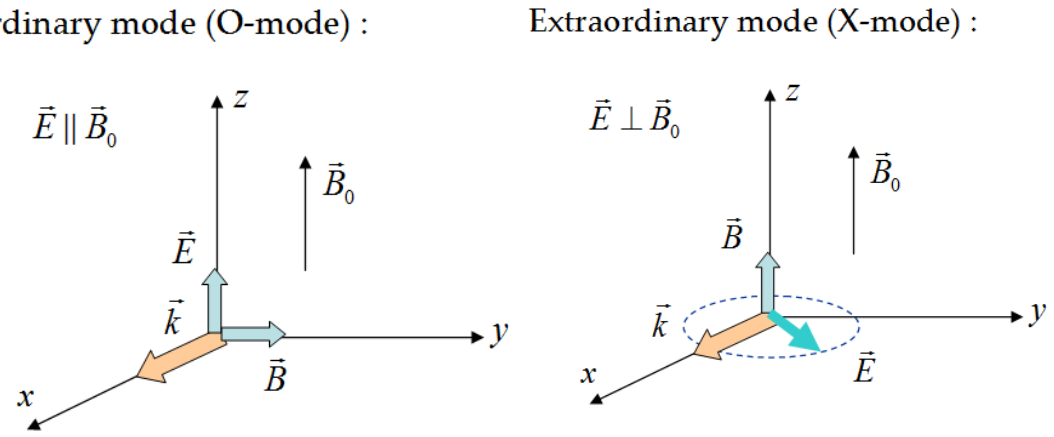

Figure 2.1. Geometry of ordinary and extraordinary waves.

2.1.3. Propagation in inhomogeneous plasma

In practice, plasma in a tokamak is not homogeneous. Plasma density profile has a maximum peak in the centre of the machine and is equal to zero at the edge. Moreover, the fluctuations of the plasma usually take place (will be discussed in the next section). To simplify the model we suppose that plasma is stationary and the refractive index depends only on radial position. We also suppose that plasma is inhomogeneous only in one (radial) direction.

The Helmholtz wave equation (31) is modified in the case of propagation in inhomogeneous plasma:

$$\frac{d^2E(x,\omega)}{dx^2} + k^2(x)E(x,\omega) = 0 \tag{45}$$

where the wave vector and the refractive index depend on radial position:

$$k^2(x) = \frac{\omega^2}{c^2}N^2(x) = k_0^2 N^2(x) \tag{46}$$

2.1.3.1. Wentzel – Kramers – Brillouin approximation

Naturally, no practical plasma or any other medium satisfies the condition of being uniform throughout all space. It is important to consider, then, what happens when there are spatial gradients in electromagnetic properties. If properties of plasma vary sufficiently slowly, then locally the wave can be thought of as propagating in an approximately uniform medium and, hence, behaving as if all the previous treatment applied. Thus, for any frequency and propagation direction, there is locally a well-defined k and a refractive index N corresponding to local values of plasma parameters. Under the assumption that spatial variations are small the Wentzel – Kramers – Brillouin (and sometimes Jeffreys, hence WKB or WKBJ) approximation is applied to solve the Helmholtz equation (45). The idea of WKB approximation operating the geometric optic or eikonal approximation is to generalize the analytical solution of the case if the length of the inhomogeneity in plasma is much higher than local wavelength. It means that the refractive index is varied slowly and the equation could be solved locally.

The solution of the electric field is searched in the form:

$$E(x,t) = E_0(x)\exp(i\phi(x))\exp(-i\omega t) \tag{47}$$

It should satisfy the following equation:

$$\frac{d^2E_0}{dx^2} - iE_0\frac{d^2\phi}{dx^2} - 2i\frac{dE_0}{dx}\frac{d\phi}{dx} + [k^2 - \left(\frac{d\phi}{dx}\right)^2]E_0 = 0 \tag{48}$$

Assuming that the electric field amplitude $E_0(x)$ varies slowly comparing to its phase, eikonal $\phi(x)$, the second order term $\frac{d^2E_0}{dx^2}$ is negligible. In this case we obtain the equation in

which each term is equal to zero. Namely, $k^2 - \left(\frac{d\phi}{dx}\right)^2 = 0$ results in expression for the electric field phase:

$$\phi(x) = \pm\int k(x)dx \tag{49}$$

The solution of the remaining equation $E_0\frac{d^2\phi}{dx^2} + 2\frac{dE_0}{dx}\frac{d\phi}{dx} = 0$ gives the expression for the electric field amplitude $E_0(x) = \frac{E_0}{\sqrt{\frac{d\phi}{dx}}} = \frac{E_0}{\sqrt{k(x)}}$, in terms of wave vector:

$$E(x,t) = \frac{E_0}{\sqrt{k(x)}}\exp[\pm i\int k(x)dx]\exp[-i\omega t] \tag{50}$$

In terms of the refractive index:

$$E(x,t) = \frac{E_0}{\sqrt{N(x)}}\exp[\pm ik_0\int N(x)dx]\exp[-i\omega t] \tag{51}$$

This approximation is valid if the second order term is negligible comparing to other terms:

$$\left|\frac{d^2E_0}{dx^2}\right| << \left|E_0\frac{d^2\phi}{dx^2}\right| \text{ and } \left|\frac{d^2E_0}{dx^2}\right| << \left|\frac{dE_0}{dx}\frac{d\phi}{dx}\right| \tag{52}$$

it means:

$$\left|\frac{d^2k}{dx^2}\right| << \left|k\frac{dk}{dx}\right| \text{ and } \left|\frac{dk}{dx}\right| << \left|k^2\right| \tag{53}$$

In terms of wavelength:

$$\frac{d^2\lambda^2}{dx^2} << \frac{d\lambda}{dx} << 1 \tag{54}$$

These conditions are conditions of the geometric optics and are valid if the wavelength varies slowly at the distance equal to the wavelength. The plasma properties should vary slowly at the scale of the wavelength.

The WKB approximation is valid far from the cut-off. In the vicinity of the cut-off layer when the refractive index goes to zero the WKB approximation is no more valid and to find the solution it is necessary to treat the equation numerically.

2.2. Plasma density fluctuations

We introduce density fluctuations to plasma as:

$$n(r) = \bar{n}(r) + \delta n(r) \tag{55}$$

In inhomogeneous plasmas density fluctuations are described by the function $\delta n(r)$. Plasma density fluctuations are described by magnitude $\delta n_0(r)$, wave number κ, frequency $\varpi/2\pi$. One of the main spatial characteristics is correlation length l_c.

The frequencies of microturbulence involved are of the order of the diamagnetic frequency, i.e. very low compared to ω_{ci}. Thus the impact on the frequency shift on the dispersion relation of the scattered wave can be neglected.

We suppose plasma density fluctuations to be small $\delta n(x)/n_c << 1$ and slowly changing in time. In this case the fluctuation part can be treated as a perturbation (Born approximation). The Fourier transform gives the relation between fluctuations in real space and their image in wave number space δn_κ:

$$\delta n_\kappa = \int \delta n(x) e^{-i\kappa x} dx \tag{56}$$

$$\delta n(x) = \frac{1}{2\pi} \int \delta n_\kappa e^{-i\kappa x} d\kappa \tag{57}$$

We also suppose that turbulence is statistically homogeneous. Using Wiener–Khinchin theorem we obtain the expression for the correlation function of random Fourier-harmonics averaged over time or over ensemble (random phase samples):

$$< \delta n_\kappa, \delta n_{\kappa'}{}^* >= 2\pi n_\kappa^2 \delta(\kappa - \kappa') \tag{58}$$

where $\delta n_{k'}{}^*$ - conjugate Fourier-harmonic; δn_k^2 wave number spectrum; $\delta(k - k')$ - Dirac's delta-function. Taking into account the relations (56) and (58) we obtain the expression for the turbulence spatial cross correlation function (or TCCF):

$$TCCF(\Delta x) =< \delta n(x) \delta n(x') >= \int \frac{dk}{2\pi} n_k^2 e^{-ik(x-x')} \tag{59}$$

2.3. Mechanism of back and forward Bragg scattering

In 1D geometry the scattering processes are forward scattering and backscattering [78, 115]. The injected wave into the plasma described by wave vector $\vec{k}_i$ and angular frequency ω_i interacts with the fluctuations characterized by wave vector $\vec{\kappa}$ and frequency $\varpi/2\pi$. Part of energy is subtracted from the wave and redistributed into space. The mechanism of scattering is similar to Bragg scattering in crystals. The scattered wave possesses a new wave vector $\vec{k}_s$ which determines its propagation direction:

$$\vec{k}_s = \vec{k}_i \pm \vec{\kappa} \tag{60}$$

The scattering angle θ (between $\vec{k}_s$ and $\vec{k}_i$) obeys the Bragg rule:

$$\left|\vec{\kappa}\right| = 2\left|\vec{k}_i\right|\sin\frac{\theta}{2} \tag{61}$$

If this relation is satisfied the turbulence wave number $\vec{\kappa}$ becomes resonant and the coupling between wave and fluctuations is maximal.

In case of stationary incident wave two turbulent wave vectors are involved into Bragg scattering process, $\vec{\kappa}$ and $-\vec{\kappa}$. In 1D the relation (61) takes a form:

$$\left|\vec{\kappa}\right| = 2\left|\vec{k}_i(x_B)\right| \tag{62}$$

where $\vec{k}_i(x_B)$ is the value of the wave vector at the resonance position x_B. In 1D the incident and scattered wave have equal frequencies and opposite wave-vectors for back Bragg scattering and similar wave-vectors for forward scattering at the scattering point. In case of ordinary mode this relation takes place only for turbulence wave numbers less than two vacuum wave numbers of the incident wave $\left|\vec{\kappa}\right| < 2\frac{\omega_i}{c}$. Bragg backscattering of the probing wave leads to phase fluctuations of the reflectometer signal. The forward scattering component of the signal contributes very little to the received signal phase perturbation, especially if antennas are far from plasma, however non-linear contributions from forward scattering at the edge of plasma influence on the reflectometry signal in 2D approach [116].

2.4. Reflectometry principles

Reflectometry measurements are based on the reflection of the microwave (with frequency from 1 to 300 GHz) launched to plasma from the cut-off layer. If the reflected wave is detected, it is possible to use it to diagnose the plasma density. The phase of the reflected wave contains information on the position of the cut-off layer and density fluctuations.

2.4.1. Standard reflectometry for plasma density profile masurements

In figure 2.2. the principal scheme of one channel reflectometry experiment is shown. A wave launched into plasma is reflected from the cut-off layer, and detected again near its launch point. It might be thought, by analogy with radar, that the phase or group delay provides a single number that is directly proportional to the distance of the cut-off layer from the launching point, independent of the density profile elsewhere in plasma. It is important to emphasize that this is not the case. The analogy with radar breaks down because plasma between the launching point and the reflection point acts, as it does in interferometry, to alter the phase delay. In other words, we must take into account the plasma refractive index of all along the wave path, unlike radar, in which the refractive index is unity everywhere [84].

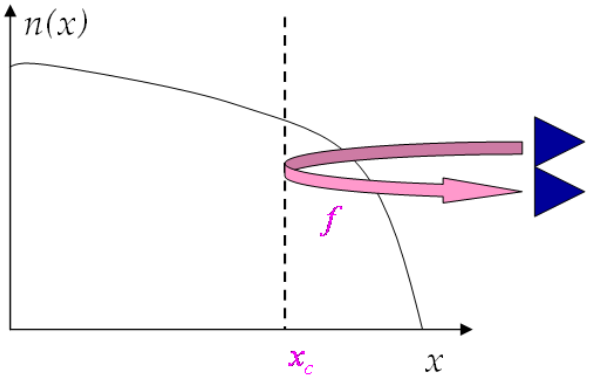

Figure 2.2. Reflectometry scheme in plasma. The wave is reflected from the cut-off layer.

As it is shown in figure 2.2. the probing wave propagates in the direction of plasma density gradient (in radial direction) from the periphery to the center of plasma. In the region from the plasma boundary to the cut-off point the geometric optics approximation is valid and launched and scattered waves are independent. Far enough from the cut-off position x_c the geometric optic approximation is valid and the electric field of the wave is described by the quasi-classical solutions of the wave equation (45). Namely, behind the cut-off the electric field of the wave takes a form (in WKB approximation):

$$E = \frac{A}{\sqrt{|k(x)|}} \exp\left(-\int_{x_c}^{x} |k(x)|\,dx \right) \tag{63}$$

and before the cut-off it is the sum of incident and reflected waves:

$$E = \frac{B}{\sqrt{k(x)}} \exp\left(i\int_{0}^{x} |k(x)|\,dx \right) + \frac{C}{\sqrt{k(x)}} \exp\left(-i\int_{0}^{x} |k(x)|\,dx \right) \tag{64}$$

The task is to find the phase of the reflected wave or the relation between amplitudes A, B and C.

The WKB form of the phase difference between points 1 and 2 is :

$$\phi_1 - \phi_2 = \frac{\omega}{c}\int_{1}^{2} N(x)dx \tag{65}$$

In the vicinity of the cut-off layer the wavelength is estimated as

$$\lambda \propto \frac{1}{\sqrt{1-\dfrac{n(x)}{n_c}}} \to \infty \tag{66}$$

and subsequently the geometric optics approximation is not valid there. It is necessary to connect the solutions at the point $x = x_c$ where $n(x_c) = n_c$. Nominally WKB solutions are not valid in the vicinity of the cut-off and as it is well known one should extend solutions analytically in upper and lower half planes of the complex variable far enough from the cut-off

point [117, 118]. The squared wave number is linearized around an interval centered on the reflection point and the solution of equation (45) is expressed in terms of Airy function [119].

Phase shift between launched and reflected waves occurs to be equal to $-\pi/2$ and correspondingly the full phase shift at the plasma boundary is [92]:

$$\varphi = 2\frac{\omega}{c}\int_0^{x_c} N(x)dx - \frac{\pi}{2} \tag{67}$$

This equation states that the phase is just what would be obtained from simple-minded application of the WKBJ approach, regarding the cut-off layer as a mirror, except that an additional $\pi/2$ phase change at reflection must be included.

To determine the cut-off position using the phase shift generally speaking it is necessary to know the plasma density profile. However for close to linear plasma density profiles the integral in the phase expression could be estimated as:

$$\frac{\omega}{c}\int_0^{x_c}\sqrt{1-\frac{n(x)}{n_c}}dx \approx 0.5\frac{\omega}{c}x_c \tag{68}$$

in case of O-mode reflectometry using $\frac{\omega_{pe}^2}{\omega^2} = \frac{n(x)}{n_c}$.

Plasma density profile along the reflectometer's wave path can be deducted from phase measurements at different frequencies. For ordinary mode the Abel integral transform is used to obtain an explicit analytic solution. For all relevant frequencies the function $\varphi(\omega)$ could be constructed by interpolation for example. Substituting the O-mode expression for *N(x)* into expression (67) after differentiating with respect to ω we express the result in terms of vacuum wave length $\lambda = 2\pi c/\omega$:

$$\frac{d\varphi}{d\omega} = 2\int_\lambda^\infty \frac{dx_c}{cd\lambda^*}\frac{\lambda^* d\lambda^*}{\sqrt{\lambda^{*2}-\lambda^2}} \tag{69}$$

where $\lambda^* = 2\pi c/\omega^*$. The most convenient expression for the cut-off position for a given frequency ω can be determined:

$$x_c(\omega) = a - \frac{c}{\pi}\int_0^\omega \frac{d\varphi}{d\omega^*}\frac{d\omega^*}{\sqrt{\omega^2-\omega^{*2}}} \tag{70}$$

The position of the cut-off is deduced from phase delay for all frequencies less than ω.

We would like to notice also that the quantity we require for the inversion is actually the derivative of the phase delay with respect to frequency. This quantity is precisely the group delay, that is, the round-trip time it would take a pulse or a modulation envelope to propagate out to the reflection layer and back:

$$\Delta t = \frac{1}{2\pi}\frac{d\varphi}{d\omega} \tag{71}$$

In case of X-mode reflectometry there is no analytical formula for the cut-off positions and the equation (67) should be treated numerically using Bottlier-Curtet method [120].

Sweeping reflectometry providing information on plasma density profile in the gradient region along the path of the reflectometry wave is based on this principle, for example [121].

2.4.2. Fluctuation reflectometry

Fixed frequency fluctuation reflectometry provides information on tokamak low frequency turbulence. Technically this method is simple and requires only single access to plasma. However due to one dimensional scattering geometry interpretation of fluctuation reflectometry results, in general, is a very complicated task. The phase delay is most sensitive to density fluctuations located near the reflection layer. However, it is also sensitive to fluctuations along the entire radiation path, and so the localization of the measurement is not the same as if one were probing an oscillating mirror at the cut-off position (despite the fact that many published analyses have adopted this analogy).

Roughly the principle of fluctuation measurements could be described as following. In presence of plasma density fluctuations (55) the relation between the fluctuation characteristics and received signal characteristics can be found. The received signal phase contains two components as well:

$$\varphi(t) = \overline{\varphi}(t) + \delta\varphi(t) \tag{72}$$

The expression (67) describes the first slow changing phase term. Supposing that fluctuation amplitude is small $|\delta n/n_c| << l_c/r_c$ fluctuating part of the phase is obtained in the frame of WKB approximation by calculating the slow phase variation [73]:

$$\delta\phi(t,\omega) = -\frac{\omega^2}{c^2}\int_0^{x_c} \frac{\delta n(x,t)}{n_c}\frac{dx}{k_0(x,\omega)} \tag{73}$$

Usually the interpretation of fluctuation reflectometry results is based on the assumption that the signal originates due to backscattering in the vicinity of the cut-off layer. Thus it is possible to obtain the relation between density fluctuation and scattering signal characteristics and estimate turbulence frequency spectrum and its level. The attempt to confirm this assumption was undertaken by numerical [73] and analytical treatment [115] of the reflectometry problem performed in 1D model. In [115] the fluctuation reflectometry has been addressed analytically, in the framework of the one dimensional WKB analysis. A singular dependence of scattering efficiency on the fluctuation wave number was demonstrated for the linear density profile. However it was assumed there that the singular (inverse proportional to fluctuation wave number $A_s \propto 1/\sqrt{\kappa}$) behavior of the scattering efficiency saturates due to the

violation of the WKB approximation at so called Airy wave number $\kappa \approx \left(\omega^2/c^2 L_n\right)^{1/3}$, where L_n is the density gradient scale length. This conclusion appears to be erroneous that predetermines the subsequent difficulties of one-dimensional theory in interpretation of experiments and numerical modeling.

2.5. Basic assumptions and equations in 1D analysis

Taking into account that RCR uses perpendicular incidence of microwave onto plasma and essentially 1D experimental geometry is less sensitive to 2D effects, compared with Doppler reflectometry or poloidal correlation reflectometry, we analyze it in the frame of 1D model simplifying calculations and allowing investigation of the arbitrary density profile case.

As it was already introduced in subsection 2.1.1., we use cold plasma approximation to describe microwave propagation in plasmas. Plasma is supposed to be an isotropic media; anisotropy is introduced only by external magnetic field. The electromagnetic wave propagating into plasma is supposed to be monochromatic and stationary. Plasma density fluctuations are supposed to be small $\delta n/n < 1\%$ and the linear (Born) approximation and the perturbation theory could be applied. Plasma is supposed to be "frozen", i.e. the turbulence correlation time $\tau_c \approx 10\mu s$ exceeds the probing time $\tau \approx 1ns$.

Supposing probing wave propagation strictly in the direction of plasma density gradient we describe the O-mode probing by Helmholtz equation (45), where $k^2(x) = \omega^2/c^2\left(1-\omega_{pe}^2/\omega^2\right)$ is a probing wave vector, $\omega_{pe} = \sqrt{4\pi e^2\left(n(x)+\delta n\left(x\right)\right)/m_e}$ is the plasma frequency; $n(x)$ is the background density profile; $\delta n\left(x\right)$ represented as (57) stands for turbulent density perturbations, where κ is a turbulence density fluctuation wave number and δn_κ is turbulent fluctuation amplitude; ω is a probing angular frequency. Under assumption that density fluctuations are small the perturbation theory methods are used. Equation (45) can be rewritten in the form:

$$\left\{\frac{d^2}{dx^2}+\frac{\omega^2}{c^2}\left(1-\frac{n(x)}{n_c}\right)\right\}E_z = \frac{\omega^2}{c^2}\frac{\delta n(x)}{n_c}E_z \tag{74}$$

where the critical density at the cut-off position is given by (40).

2.5.1. Reciprocity theorem

In particular, the scattering signal amplitude in linear (Born) approximation can be obtained with the help of straightforward approach based upon the reciprocity theorem in the form

introduced in [122]. This approach refers to a radiation received by antenna from hot inhomogeneous plasma confined in a laboratory device, in a tokamak. This subsection is based on the work performed by A. D. Piliya and A. Yu. Popov [122].

The radiation electric $\vec{E}(\omega;\vec{r})$ and magnetic $\vec{H}(\omega;\vec{r})$ fields with a frequency ω are governed by the Maxwell equations:

$$\begin{aligned} rot\vec{E}\left(\omega;\vec{r}\right)-\frac{i\omega}{c}\vec{H}\left(\omega;\vec{r}\right)=0,\\ rot\vec{H}\left(\omega;\vec{r}\right)+\frac{i\omega}{c}\vec{D}\left(\omega;\vec{r}\right)=\frac{4\pi}{c}\vec{j}_s\left(\omega;\vec{r}\right) \end{aligned} \tag{75}$$

where $\vec{j}_s\left(\omega;\vec{r}\right)$ is the radiation source current and $\vec{D}$ is the electric displacement vector. In the case of the collective scattering the source current results from non-linear coupling between the incident radiation and fluctuating plasma parameters. For spontaneous noise-like emission, the source is the fluctuating current of non-interacting («bare») electrons. We assume linear relation between $\vec{D}$ and $\vec{E}$, $\vec{D}=\hat{\varepsilon}\vec{E}$ with the dielectric operator $\hat{\varepsilon}$ defined according to

$$D_i\left(\omega;\vec{r}\right)=\int \varepsilon_{ik}\left(\omega;\vec{r},\vec{r}'\right)\,E_k\left(\omega;\vec{r}'\right)d\vec{r}' \tag{76}$$

This relation is applicable to any medium, including hot inhomogeneous plasmas as well as dielectrics and metals. Thus, equation (75) with a proper dielectric operator describes the radiation fields in the entire space.

The required solution to equation (75) is determined by the demand that the fields are continues functions of co-ordinates and represent asymptotically at $\vec{r}\to\infty$ outgoing waves.

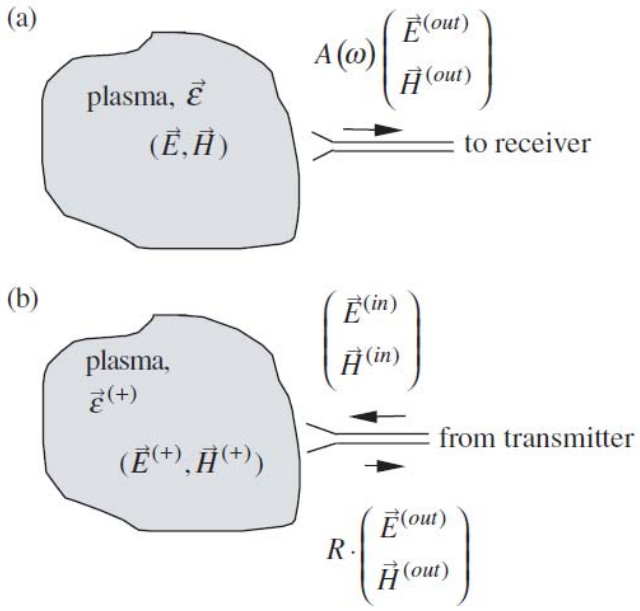

Figure 2.3. (a) Schematic of experimental arrangement for emission registration. (b) Imaginaryarrangement for launching antenna beam ($E^{(+)}$,$H^{(+)}$).

Suppose that the radiation is received by a microwave antenna and transmitted through a plasma-free single mode wave-guide to a registration device (see figure 2.3). Then far from the antenna mouth within the wave-guide,

$$\begin{pmatrix} \vec{E} \\ \vec{H} \end{pmatrix} = A(\omega) \begin{pmatrix} \vec{E}^{(out)} \\ \vec{H}^{(out)} \end{pmatrix} \tag{77}$$

where $A(\omega)$ is the signal amplitude and $\left(\vec{E}^{(out)}, \vec{H}^{(out)}\right)$ are the electric and magnetic fields of the fundamental wave-guide mode propagating outward from plasma volume and normalized to unit energy flux by

$$\frac{c}{8\pi} \int [\vec{E}^{(out)} \times (\vec{H}^{(out)})^*] \cdot d\vec{S} = 1 \tag{78}$$

where $d\vec{S}$ is the surface element in the wave-guide cross-section. The symbol of the real part before the integral is omitted because the integrand is a real function due to the wave-guide mode properties (see, for example, [123]). Equation (78) implies perfect matching with the receiver.

At sufficiently small source current, the scalar amplitude $A(\omega)$ depends linearly on the vector $\vec{j}_s$. The most general form of this relation is

$$A(\omega) = \int \vec{j}_s(\omega;\vec{r}) \vec{g}(\omega;\vec{r}) d\vec{r} \tag{79}$$

where integration is over the plasma volume. The vector weight function $\vec{g}(\omega;\vec{r})$ is, obviously, related to the Green function of equations (75). Finding this function satisfying proper boundary conditions represents the main difficulty in the signal calculation.

Alternatively the amplitude can be calculated in the following way. Imagine that the plasma in the experiment on the emission measurement is replaced by a fictitious medium whose dielectric operator, $\hat{\varepsilon}^T$, is obtained by transposition of the dielectric operator of the real plasma:

$$\varepsilon_{ik}^T(\omega;\vec{r},\vec{r}') = \varepsilon_{ki}(\omega;\vec{r}',\vec{r}) \tag{80}$$

Suppose, further, that an electromagnetic field $\vec{E}^{(+)}(\omega;\vec{r})$, $\vec{H}^{(+)}(\omega;\vec{r})$ is produced in this «transposed» plasma by radiating unite microwave power at the frequency ω through the receiving antenna, (see figure 2.3.(b)). Then

$$\vec{g} = \frac{1}{4} \cdot \vec{E}^{(+)} \tag{81}$$

To prove this claim, note, that according to its definition, ε_{ik}^T satisfies, as a function of ω, the Krammers-Kronig relations and vanishes at $|\vec{r} - \vec{r}'| \to \infty$. These features guarantee that the transposed plasma is physically realisable. Suppose, further, that in the real plasma all oscillations at the frequency ω are damped, i.e. $Q \geq 0$ for any electric field $\vec{E}$. Here

$$Q(\omega) = \frac{\omega}{8\pi} \int \vec{E}^*(\omega;\vec{r}) \hat{\varepsilon}^A(\omega;\vec{r},\vec{r}') \vec{E}(\omega;\vec{r}') d\vec{r} d\vec{r}' \tag{82}$$

is the RF power dissipated in the whole plasma volume with $\hat{\varepsilon}^A(\omega;\vec{r},\vec{r}') = \left\{\hat{\varepsilon}(\omega;\vec{r},\vec{r}') - (\hat{\varepsilon}^T(\omega;\vec{r},\vec{r}'))^*\right\}/2i$ being the "anti-Hermitian" part of $\hat{\varepsilon}(\omega;\vec{r},\vec{r}')$. Writing similar relation for the transposed plasma and changing variables $\vec{r} \rightleftarrows \vec{r}'$ in the integral, we obtain again equation (82) with $\vec{E}$ replaced by $\vec{E}^*$. Thus the transposed plasma possesses the same property of stability as the real plasma.

Taking into account these general features of the transposed plasma we can conclude that the wave equation

$$\begin{aligned} rot\vec{E}(\omega;\vec{r}) - \frac{i\omega}{c}\vec{H}(\omega;\vec{r}) = 0, \\ rot\vec{H}(\omega;\vec{r}) + \frac{i\omega}{c}\hat{\varepsilon}^T\vec{E}(\omega;\vec{r}) = 0 \end{aligned} \tag{83}$$

in this plasma has physically reasonable solutions determined unambiguously by the boundary conditions.

In metallic and dielectric objects surrounding the plasma, including the chamber walls, the dielectric operator kernel $\varepsilon_{ik}(\vec{r},\vec{r}')$ has the form $\varepsilon_{ik}(\vec{r},\vec{r}') = \varepsilon \cdot \delta_{ik} \cdot \delta(\vec{r}-\vec{r}')$, where ε is a scalar. Hence, $\hat{\varepsilon} = \hat{\varepsilon}^T$ here and Eq. (9), similar to equations (75), is valid in the entire space.

The particular solution $\vec{E}^{(+)}, \vec{H}^{(+)}$ to equations (83) which determines, according to equation (79), the signal amplitude has asymptotically, at $\vec{r} \to \infty$, the form

$$\begin{pmatrix} \vec{E}^{(+)} \\ \vec{H}^{(+)} \end{pmatrix} \to \begin{pmatrix} \vec{E}^{(in)} \\ \vec{H}^{(in)} \end{pmatrix} + R\begin{pmatrix} \vec{E}^{(out)} \\ \vec{H}^{(out)} \end{pmatrix} \tag{84}$$

in the antenna wave-guide and represents outgoing waves (or vanishes) elsewhere. Here $(\vec{E}^{(in)}, \vec{H}^{(in)})$ is the incident (traveling toward the plasma) wave-guide mode normalised similar to equation (78) and the coefficient of reflection R is a constant with $|R| \le 1$. Now multiply both equations (75) by $\vec{H}^{(+)}$ and $\vec{E}^{(+)}$, respectively, and equations (83) by $-\vec{H}$ and $-\vec{E}$. Summing four obtained equalities term by term obtain

$$div\left\{\vec{E}\times\vec{H}^{(+)} + \vec{H}\times\vec{E}^{(+)}\right\} = i\frac{\omega}{c}(\vec{E}\vec{D}^{(+)} - \vec{D}\vec{E}^{(+)}) + \frac{4\pi}{c}\vec{j}_s\vec{E}^{(+)} \tag{85}$$

Integrate this equation over a large volume $V \to \infty$ bounded by a surface S_0 assuming formally that the wave-guide feeding the antenna goes through the surface. The volume integral in the left-hand side of the equation transform into the surface integral:

$$\int_V div\left\{\vec{E}\times\vec{H}^{(+)} + \vec{H}\times\vec{E}^{(+)}\right\}d^3r = \int_{S_0}\left\{\vec{E}\times\vec{H}^{(+)} + \vec{H}\times\vec{E}^{(+)}\right\}d\vec{S} \tag{86}$$

Outside the wave-guide, solutions of equations (75) and (83) can be considered in a small area of the surface as plane waves propagating in the same direction. Then two terms in the surface integral cancel out each other. The only contribution comes from the part S_{wg} of the surface S_0 inside the wave-guide where the fields $\vec{E}^{(+)}, \vec{H}^{(+)}$ include waves propagating

opposite to $\vec{E},\vec{H}$. This contribution can be easily evaluated using known properties of the wave-guide modes (see, for example, [123]) and equation (78):

$$\int_{S_{wg}} \left\{ \vec{E} \times \vec{H}^{(+)} + \vec{H} \times \vec{E}^{(+)} \right\} d\vec{S} = (16\pi / c) A(\omega) \tag{87}$$

In the right-hand side, the volume integral

$$\int (\vec{E}\vec{D}^{(+)} - \vec{D}\vec{E}^{(+)}) d^3 r \tag{88}$$

vanishes due to the relations (2) and (6). Now, equating remaining terms, obtain

$$A(\omega) = \frac{1}{4} \int \vec{j}_s \vec{E}^{(+)} d\vec{r} \tag{89}$$

Comparing this expression with equation (79) obtain equation (81). Because of its relation to the fictitious antenna radiation, $\vec{E}^{(+)}$ will be referred to as the antenna beam. Equation (89) represents a formulation of the reciprocity theorem for the case of emission and relates the weight of a given point in the signal formation to the antenna ability to illuminate this point in the «transposed» plasma. In obtaining equation (89), no assumptions concerning the nature of the emitting substance has been made except general non-local relation (76) between $\vec{E}$ and $\vec{D}$. Thus equation (89) is valid for any medium, including arbitrary inhomogeneous hot magnetized plasma. The function $\vec{E}^{(+)}(\vec{r})$ in equation (89) is an exact solution of the wave equation (83), which can include cut-offs and resonances.

The reciprocity theorem takes in one-dimensional case the form:

$$A_s = \frac{1}{4} \int \vec{j}_s(x) \vec{E}^{(0)}(x) dx \tag{90}$$

The nonlinear current entering the expression is given by

$$\vec{j}_s = i \frac{e^2 \delta n(x)}{m_e \omega} \sqrt{S_i} \vec{E}^{(0)}(x) \tag{91}$$

where S_i and $|A_s|^2$ is an incident and scattered wave energy flux density correspondingly. Finally the expression for the scattering signal amplitude takes a form

$$A_s(\omega) = \frac{i\omega\sqrt{S_i}}{16\pi} \int_0^{+\infty} \frac{\delta n(x)}{n_c} \left(E^{(0)}(\omega, x) \right)^2 dx \tag{92}$$

where the integration is made from the plasma edge (x=0).

2.6. Scattering signal in case of linear plasma density profile

Firstly, we consider the linear density profile case $n(x) = n_c\, x/L$. The classical solution of the unperturbed equation (45) takes a form:

$$E^{(0)}(x) = \sqrt{2\omega} \frac{4\pi}{c} Ai\left((x - L)/\alpha \right) \tag{93}$$

where $Ai\left(\left(x-L\right)/\alpha\right)$ is the Airy function [119] and $\alpha=\left(Lc^2/\omega^2\right)^{1/3}$ is the Airy scale length [107] characterizing the distance between the cut-off and the first peak of the Airy function (see for example figure 2.4.).

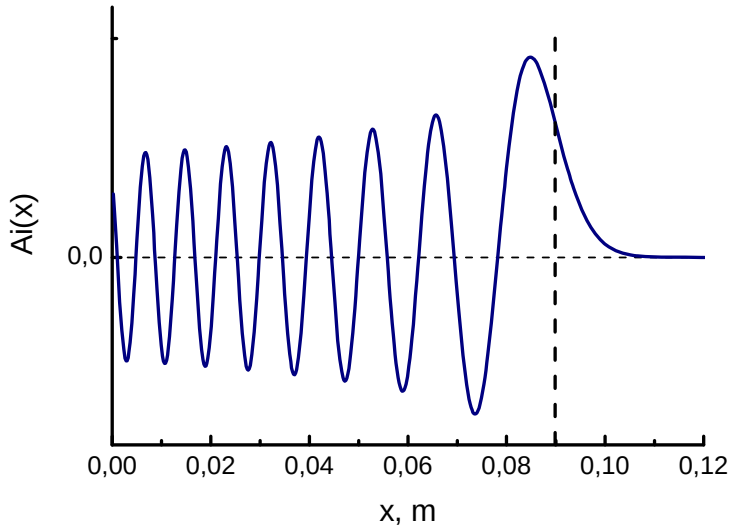

Figure 2.4. Airy function, $L=0.09m,\ f=40GHz,\ \alpha\approx 0.005m$.

Using the integral representation of Airy function the scattering signal can be calculated. In order to simplify the expression for the scattering signal (92) we substitute into the equation (92) the integral representation of the Airy function [119]:

$$Ai(z)=\frac{1}{2\pi}\int_{-\infty}^{+\infty}e^{i\left(\frac{t^3}{3}+tz\right)}dt \tag{94}$$

where $z=\left(x-L\right)/\alpha$. Thus the expression for the scattered signal amplitude is obtained in the following form:

$$A_s(\omega)=i2\pi\sqrt{S_i}\frac{\omega^2}{c^2}\frac{1}{4\pi^2}\int_{-L/\alpha}^{+\infty}\int_{-\infty}^{+\infty}\int_{-\infty}^{+\infty}\int_{-\infty}^{+\infty}e^{i\left(\frac{t^3}{3}+tz\right)}e^{i\left(\frac{p^3}{3}+pz\right)}\frac{\delta n_\kappa}{n_c}e^{i\kappa\left(L+\alpha z\right)}\frac{d\kappa}{2\pi}dtdpdz \tag{95}$$

Introducing new variables in the following way $u=t+p$, $v=t-p$, we obtain the integral representation as:

$$A_s(\omega)=i2\pi\sqrt{S_i}\frac{\omega^2}{c^2}\frac{1}{4\pi^2}\frac{1}{2}\int_{-L/\alpha}^{+\infty}\int_{-\infty}^{+\infty}\int_{-\infty}^{+\infty}\int_{-\infty}^{+\infty}e^{i\left(\frac{u^3}{12}+\frac{1}{4}uv^2+uz+\alpha\kappa z\right)}\frac{\delta n_\kappa}{n_c}e^{i\kappa L}dtdp\frac{d\kappa}{2\pi}dz \tag{96}$$

Integrals over v and z can be easily evaluated here, providing

$$\int_{-\infty}^{+\infty}e^{i\frac{1}{4}uv^2}dv=e^{i\frac{\pi}{4}}\sqrt{\pi}\Big/2\sqrt{u} \tag{97}$$

and

$$\int_{-L/\alpha}^{+\infty} e^{i(u+\alpha k)z}dz = -\frac{e^{-i(u+\alpha k)\frac{L}{\alpha}}}{i(u+\alpha k)} \tag{98}$$

under condition *Im(u)>0*. Finally the expression for scattered signal amplitude takes a form

$$A_s(\omega) = i2\pi\sqrt{S_i}\,\frac{\omega^2}{c^2}\frac{\sqrt{\pi}}{4\pi^2}\frac{1}{2}\int_{-\infty}^{+\infty}\int_{-\infty}^{+\infty}\frac{e^{i\frac{u^3}{12}-i\frac{L}{\alpha}u}}{\sqrt{u}\left(u+\alpha\kappa\right)}\frac{\delta n_\kappa}{n_c}\frac{d\kappa}{2\pi}du \tag{99}$$

Assuming the plasma size larger that Airy scale ($L>>\alpha$), the characteristic integral

$$I(\kappa) = \int_{-\infty}^{+\infty}\frac{e^{i\frac{u^3}{12}-i\frac{L}{\alpha}u}}{\sqrt{u}\left(u+\alpha\kappa\right)}du \tag{100}$$

can be calculated using the stationary-phase method [124] (see Appendix A).

2.6.1. Asymptotic forms of the characteristic integral

Taking in account the restriction *Im(u)>0* we deform the integration contour as it is shown in figure 2.5. The integration contour has two stationary phase points $u_1 = 2\sqrt{L/\alpha}$ and $u_2 = -2\sqrt{L/\alpha}$ and the branch point $u_3 = 0$. The shading in figure 2.5. shows the domain of exponential growth.

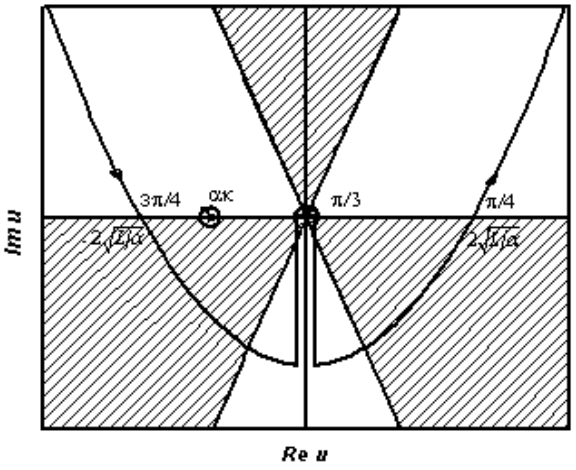

Figure 2.5. The integration contour of the integral.

2.6.1.1. Contribution of the pole

Firstly we examine the contribution to the integral by pole. In case $|\alpha\kappa| > 2\sqrt{L/\alpha}$ (or $|\kappa| > 2\omega/c$) the contour does not touch the pole, in the result there is no contribution. In case $1 << |\alpha\kappa| < 2\sqrt{L/\alpha}$ the contribution to the integral by pole could be estimated as

$$I(\kappa) = 2\pi \frac{e^{-i\frac{(\alpha\kappa)^3}{12}+i\kappa L}}{\sqrt{\alpha\kappa}} \tag{101}$$

This expression is proportional to $1/\sqrt{\kappa}$ and describes the Bragg backscattering contribution to the scattering signal. In case $|\alpha\kappa| = 2\sqrt{L/\alpha}$ the Bragg backscattering takes place directly at the plasma boundary with a wave number $|\kappa| = 2\omega/c$.

2.6.1.2. Contribution of the branch point

When calculating the contribution of the branch point $u_3 = 0$ it is necessary to note that the phase is different at two sides of the cut. In case $|\alpha\kappa| >> 1$ it is possible to neglect $u << \alpha\kappa$ in denominator of the integral (100), than we obtain the integral in the form

$$I(\kappa) = I_1 + I_2 \approx -\int_0^{+\infty} \frac{e^{-\frac{L}{\alpha}t}}{e^{i\frac{3\pi}{4}}\sqrt{t\alpha\kappa}} e^{i\frac{3\pi}{2}} dt + \int_0^{+\infty} \frac{e^{-\frac{L}{\alpha}t}}{e^{-i\frac{\pi}{4}}\sqrt{t\alpha\kappa}} e^{-i\frac{\pi}{2}} dt = -2e^{i\frac{3\pi}{4}}\sqrt{\pi}\frac{1}{\alpha\kappa}\sqrt{\frac{\alpha}{L}} \tag{102}$$

The integral scales as $1/\kappa$ with the wave number and is much smaller than contribution of the pole. Otherwise if $|\alpha\kappa| << 1$ the parameter in denominator could not be neglected, nevertheless we may assume the cubic term in the exponent to be small. Under this assumption it is possible to express the integral in terms of the error function

$$I(\kappa) = -4\sqrt{\pi}e^{i\kappa L}\, erf\sqrt{i|\kappa L|}\Big/\sqrt{\alpha\kappa} \tag{103}$$

where we use for the error function the definition $erf(x) = \int_0^x e^{-s^2} ds$. This expression can be further simplified, for instance for $1/\alpha << |\kappa| << 1/L$ we obtain

$$I \approx -2\pi e^{i\kappa L}\Big/\sqrt{\alpha\kappa} \tag{104}$$

whereas at $|\kappa L| \leq 1$ the integral takes a value:

$$I \approx -4\sqrt{\pi}e^{i\frac{\pi}{4}}e^{i\kappa L}\sqrt{L/\alpha} \tag{105}$$

2.6.1.3. Contribution of the stationary phase points

The stationary phase points contribution $u_1 = -2\sqrt{L/\alpha}$ and $u_2 = 2\sqrt{L/\alpha}$ is given by the expression

$$I \approx 2i\sqrt{\pi}\cos\left(\frac{4}{3}(L/\alpha)^{3/2} + \frac{\pi}{4}\right)\Big/\sqrt{L/\alpha} \tag{106}$$

which physically describes the scattering from plasma boundary. It could be noticed that this item is much smaller than contribution of the pole because of the large parameter $L/\alpha >> 1$ in denominator.

2.6.2. Asymptotic forms of scattering signal

Change of variables and integration leads to the expression for the scattering signal in the form

$$A_s = \int_{-\infty}^{+\infty} R(\kappa)\frac{\delta n_\kappa}{n_c}\frac{d\kappa}{2\pi} \tag{107}$$

where

$$R(\kappa) = \frac{i\sqrt{S_i}}{8\pi^{3/2}}\frac{\omega^2}{c^2}e^{-i\frac{\pi}{4}}\int_{-\infty}^{+\infty}\frac{e^{i\frac{u^3}{12}-i\frac{L}{\alpha}u}}{\sqrt{u}(u+\alpha\kappa)}du \tag{108}$$

As a result of the part 2.6.1, the partial amplitude $R(\kappa)$ takes the following simple form

$$R(\kappa) = \frac{i\sqrt{S_i}}{8\pi^{3/2}}\frac{\omega^2}{c^2}e^{-i\frac{\pi}{4}}e^{i\kappa L}\begin{cases} 2\pi\dfrac{e^{-i\frac{(\alpha\kappa)^3}{12}}}{\sqrt{\alpha\kappa}}, & 1/\alpha << |\kappa| < 2\,\omega/c \\ -4\sqrt{\pi}\dfrac{erf\left(\sqrt{i\kappa L}\right)}{\sqrt{\alpha\kappa}}, & |\kappa| << 1/\alpha \end{cases} \tag{109}$$

The expression (109) describes Bragg back scattering; it scales as $1/\sqrt{\kappa}$ with the turbulence wave number as it was predicted in [115]. In case $|\alpha\kappa| = 2\sqrt{L/\alpha}$ the Bragg condition is fulfilled ($\kappa = \pm 2k(x)$) for $|\kappa| = 2\omega/c$ and the scattering takes place directly at the plasma boundary.

The expression for the partial amplitude $R(\kappa)$ can be simplified using asymptotic representation for the error function. Furthermore, in the intervals $1/L << |\kappa| << 1/\alpha$ and $|\kappa| << 1/L$ corresponding to small angle scattering it can be written accordingly

$$R(\kappa) = \frac{i\sqrt{S_i}}{8\pi^{3/2}}\frac{\omega^2}{c^2}e^{-i\frac{\pi}{4}}e^{i\kappa L}\begin{cases} -\dfrac{2\pi}{\sqrt{\alpha\kappa}}, & 1/L << |\kappa| << 1/\alpha \\ -4\sqrt{\pi}e^{i\frac{\pi}{4}}\sqrt{L/\alpha}, & |\kappa| << 1/L \end{cases} \tag{110}$$

As it is seen from equation (110) for wave numbers of Airy range and smaller the singular dependence $1/\sqrt{\kappa}$ persists as well, in contradiction with unjustified assumption made in [115] by B. B. Afeyan in 1994:

$$A_s \propto \begin{cases} \dfrac{1}{\sqrt{\kappa}}, & |\kappa| > 1/\alpha \\ Const, & |\kappa| \le 1/\alpha \end{cases} \tag{111}$$

It is necessary to stress that in the analysis presented in this Chapter this singular dependence on κ saturates only at $|\kappa| << 1/L$ where relation (110) holds.

2.6.3. Numerical computation example

In order to check the accuracy of asymptotic expressions for the partial amplitude $R(\kappa)$ (109) and (110) numerical computations of integral (108) were performed. Figure 2.6. shows the comparison of numerically computed absolute value of the integral (108) (the calculation parameters are as follows: $L = 0.08m$, $\alpha = 0.00464\,m$, $f = 45GHz$), expression (109) and a simple dependence $1/\sqrt{\kappa}$. It can be seen that proposed asymptotic form (109) describes the behaviour of the integral perfectly even for large wave numbers. In general the behaviour of both asymptotic form and integral is well described by $1/\sqrt{\kappa}$ dependence. For $|\alpha\kappa| > 2\sqrt{L/\alpha}$ it is no longer possible to satisfy the Bragg condition within the plasma slab therefore the behaviour of integral and its asymptotic representation is different (figure 2.6.(a)) in agreement with results of 1D numerical computations [125] , where it was stated that the wave numbers higher than the Bragg detection limit do not contribute to the phase fluctuations. Figure 2.6.(b) illustrates also the singularity saturation at small wave numbers $|\kappa| << 1/L$. In spite of the fact there is no simple analytical description of the partial amplitude $R(\kappa)$ for $|\alpha\kappa| \approx 1$ the numerical calculations show that the function is smooth and its behaviour can be described by proposed analytical asymptotic form (109) also in this region.

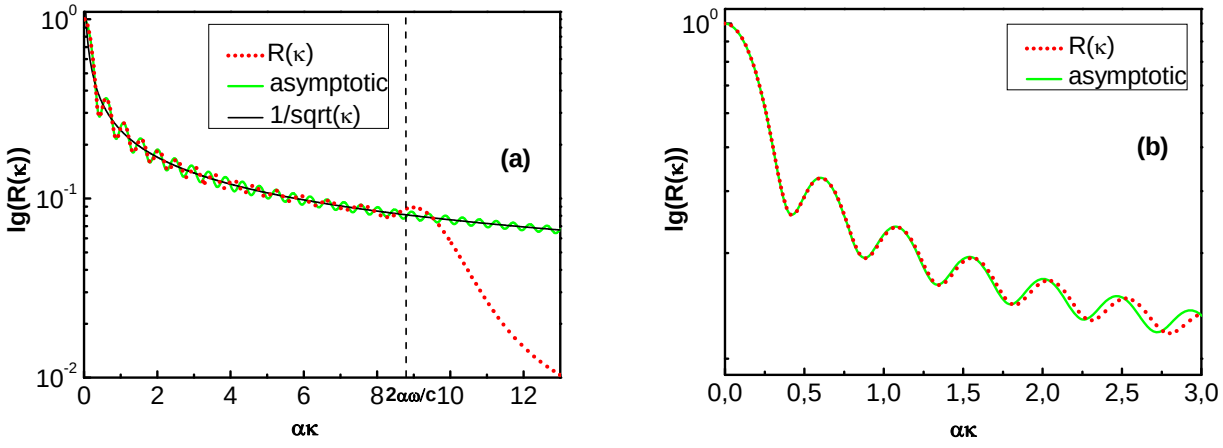

Figure 2.6. The comparison of absolute values of analytical approximations (109) and the partial amplitude $R(\kappa)$ directly using (92) shown in relative units in range $0 < \kappa \approx 2\omega/c$ (a) and $0 < \alpha\kappa < 3$ (b). The dependence $1/\sqrt{\kappa}$ is represented in (a), the double vacuum wave number $\kappa = 2\omega/c$ is shown by vertical dashed line in (a).

2.6.4. WKB representation of Airy function

Unfortunately the above simple asymptotic expressions for the partial amplitude were obtained using the technique specific for the linear density profile, which is not applicable directly to the arbitrary profile case. Nevertheless, the asymptotic representations (109) and (110) can be derived in the framework of more general approaches not utilising the integral representation for the Airy function and formula (108). Namely, the asymptotic form (109) corresponding to the Bragg backscattering can be obtained using the WKB representation of Airy function which provides for the field $E^{(0)}$ the following expressions

$$E^{(0)}(\xi)=\frac{4\sqrt{2\pi\omega}}{c}\frac{\sin(\frac{2}{3}|\xi|^{3/2}+\frac{\pi}{4})}{\sqrt[4]{|\xi|}},\quad \xi<-1 \tag{112}$$

$$E^{(0)}(\xi)=\frac{2\sqrt{2\pi\omega}}{c}\frac{e^{-\frac{2}{3}\xi^{3/2}}}{\sqrt[4]{\xi}},\quad \xi>>1 \tag{113}$$

Here it is assumed that the experimental scheme is calibrated to provide the same probing wave phase at the cut-off not depending on frequency. This kind of calibration is the most beneficial for the RCR experiment.

Substituting this formula into equation (92) and performing integration there using the stationary phase method we obtain for partial amplitude $R(\kappa)$ the expression (109) valid for $|\kappa|>>1/\alpha$. In the opposite case the stationary phase method is no longer applicable. The entire integration interval including the cut-off vicinity where (110) is not valid contribute to the $R(\kappa)$. However in this case we may approximate in the transparency

$$\left(E^{(0)}\right)^2\approx 16\,\omega/c^2\sqrt{|\xi|},\quad \xi<0 \tag{114}$$

and obtain after the integration over this region expression (110) for $R(\kappa)$.

2.6.5. Long wavelength limit

It should be noted that in the long wavelength limit $|\kappa|<<1/\alpha$ we may also directly apply the WKB approximation to describe the fluctuation contribution to the reflected wave phase. The solution of (45) may be written in this case as a superposition of incident and reflected waves:

$$E_z=\frac{4\sqrt{2\pi\omega}}{c}\left(e^{i\int_L^x\frac{\omega}{c}\sqrt{1-\frac{x}{L}-\frac{\delta n(x)}{n_c}}dx-i\frac{\pi}{4}}-e^{-i\int_L^x\frac{\omega}{c}\sqrt{1-\frac{x}{L}-\frac{\delta n(x)}{n_c}}dx-i\frac{3\pi}{4}}\right)\frac{E_0}{\sqrt[4]{1-\frac{x}{L}-\frac{\delta n(x)}{n_c}}} \tag{115}$$

This form is valid everywhere except the very neighbourhood of the cut-off point. In the case the turbulence level is low enough, so that the reflected wave phase perturbations are small

$$\delta\varphi(\omega)=\frac{\omega}{c}\int_0^{x_c}\frac{\delta n(x)}{n_c(\omega)}\frac{dx}{\sqrt{1-x/L}}<1 \tag{116}$$

the fluctuation reflectometry signal is given by simple expression $\delta E = i\delta\varphi(\omega)E_z$. When we substitute the density perturbation Fourier spectrum there we obtain the phase perturbation in the following form

$$\delta\varphi(\omega)=\frac{\omega}{c}\int_{-\infty}^{+\infty}\frac{\delta n(\kappa)}{n_c}\int_0^{L}\frac{e^{i\kappa x}dx}{\sqrt{1-x/L}}\frac{d\kappa}{2\pi} \tag{117}$$

We utilize the substitution $s=\sqrt{1-x/L}$ to calculate this integral. Finally, the corresponding expression for $R(\kappa)$ obtained from (117) coincides with the expression (109).

2.7. Scattering signal in case of arbitrary plasma density profile

Plasma density profile in a tokamak in general is not linear; therefore the theoretical description of the wave propagation into the realistic plasma density profile is required.

We analyze the arbitrary profile case by means of approximate methods introduced in previous sections for investigation of the linear density profile case. Supposing the density profile to be monotonous, we find the solution of the unperturbed Helmholtz equation (45) using WKB approximation in the form

$$E^{(0)}(x)\cong\frac{4\sqrt{2\pi\omega}}{c}\sin\left(\int_{x_c}^{x}k(x)dx+\frac{\pi}{4}\right)\Bigg/\sqrt{\frac{c}{\omega}k(x)} \tag{118}$$

$E^{(0)}(x)$ gives the distribution of the probing wave electric field in plasma in the case of unit incident energy flux density as it was shown in part 2.5. When substituting $E^{(0)}(x)$ into the integral (92) we derive

$$A_s=\int_{-\infty}^{+\infty}\tilde{R}(\kappa)\frac{\delta n_\kappa}{n_c}\frac{d\kappa}{2\pi} \tag{119}$$

where the partial amplitude $\tilde{R}(\kappa)$ may be represented as

$$\tilde{R}(\kappa)\cong\frac{i\sqrt{S_i}}{8\pi^{3/2}}\frac{\omega^2}{c^2}\left\{\int_0^{x_c}\frac{e^{i2\int_{x_c}^{x}k(x')dx'-i\frac{\pi}{2}}}{4k(x)}e^{i\kappa x}dx-\int_0^{x_c}\frac{e^{i\kappa x-i\pi}}{2k(x)}dx+\int_0^{x_c}\frac{e^{-i2\int_{x_c}^{x}k(x')dx'-i\frac{3\pi}{2}}}{4k(x)}e^{i\kappa x}dx\right\} \tag{120}$$

Here we integrate from the plasma edge to the cut-off ($x=x_c$). The largest contribution to (120) at $1/\alpha_n << |\kappa| < 2\omega/c$ is provided by the first or the third item under the integral (120).

Here $\alpha_n = \left(L_n c^2/\omega^2\right)^{1/3}$ and $L_n = \left|\frac{1}{n_c}\frac{dn(x)}{dx}\right|^{-1}_{x=x_c}$.

We use the stationary phase method (see Appendix A) analogous to part 2.6.2. for an asymptotic evaluation of the integral (120) in this case. Stationary phase point x_B is determined by the equation

$$\kappa^2 = 4\frac{\omega^2}{c^2}\left(1-\frac{n(x_B)}{n_c}\right) \tag{121}$$

corresponding to Bragg backscattering conditions.

Neglecting the contribution of the second term we obtain the expression for the partial amplitude in the form:

$$\tilde{R}(\kappa) \cong \frac{i\sqrt{S_i}}{8\pi^{3/2}}\frac{\omega^2}{c^2}\frac{i}{4\sqrt{2\pi}}\begin{cases}\dfrac{1}{\sqrt{\kappa}}\dfrac{e^{-i2\int_{x_c}^{x_B}k(x')dx'+i\kappa x_B+i\frac{\pi}{2}}}{\sqrt{2\left|\frac{1}{n_c}\frac{dn(x)}{dx}\right|_{x_B}}}, & 1/\alpha_n << \kappa < 2\,\omega/c \\ \dfrac{1}{\sqrt{\kappa}}\dfrac{e^{i2\int_{x_c}^{x_B}k(x')dx'+i\kappa x_B+i\frac{\pi}{2}}}{\sqrt{2\left|\frac{1}{n_c}\frac{dn(x)}{dx}\right|_{x_B}}}, & -2\,\omega/c < \kappa << -1/\alpha_n\end{cases} \tag{122}$$

In the opposite case of long scale fluctuations, at $|\kappa| << 1/\alpha$, the second term in (120) provides the dominant contribution to the integral which is given by

$$\tilde{R}(\kappa) \cong \frac{i\sqrt{S_i}}{8\pi^{3/2}}\frac{\omega^2}{c^2}\frac{i}{4\sqrt{2\pi}}\int_0^{x_c}\frac{e^{i\kappa x}dx}{\sqrt{1-\frac{n(x)}{n_c}}}dx, \quad |\kappa| << 1/\alpha_n \tag{123}$$

It is significant that for $1/L_n << |\kappa| << 1/\alpha_n$ the main contribution to the integral over coordinate in (123) is provided by the vicinity of the cut-off, where the density profile is linear and it is quite naturally that the partial amplitude in this case is given by the expression $\tilde{R}(\kappa) \propto \frac{1}{\sqrt{\alpha_n \kappa}}$.

For $|\kappa| \le 1/L$ the signal scattering does not take place only in the cut-off vicinity so that the profile can not be supposed linear, therefore taking in account $e^{i\kappa x} \approx 1$ for $|\kappa| << 1/L_n$, we obtain the expression (123) in the form

$$\tilde{R}(\kappa) = \frac{i\sqrt{S_i}}{8\pi^{3/2}}\frac{\omega^2}{c^2}\frac{i}{4\sqrt{2\pi}}\int_0^{x_c}\frac{dx}{\sqrt{1-\frac{n(x)}{n_c}}}dx, \quad |\kappa| << 1/L_n \tag{124}$$

2.7.1. Numerical computation example for parabolic plasma density profile

In case of parabolic plasma density profile $n(x) = n_c \frac{(1-(1-x/L_{pl})^2)}{(1-(1-L_0/L_{pl})^2)}$, (where plasma characteristic length is $L_{pl} = 0.9m$, the cut-off position $L_0 = 0.7m$, probing frequency $f = 55.7GHz$, Airy scale length $\alpha_n \approx 0.008m$) we compare the partial amplitude directly computed from the Helmholtz equation using (92) and its approximation (122) (figure 2.7.). It can be seen that the asymptotic form describes the absolute value as well as real and imaginary parts of the partial amplitude rather precisely for $\kappa > 1/\alpha_n$ (figure 2.7.(b)). Therewith only in the very vicinity of zero κ (figure 2.7.(a)) and in the domain where Bragg condition is not fulfilled (figure 2.7.(c)) the behavior of function and its asymptotic form differs.

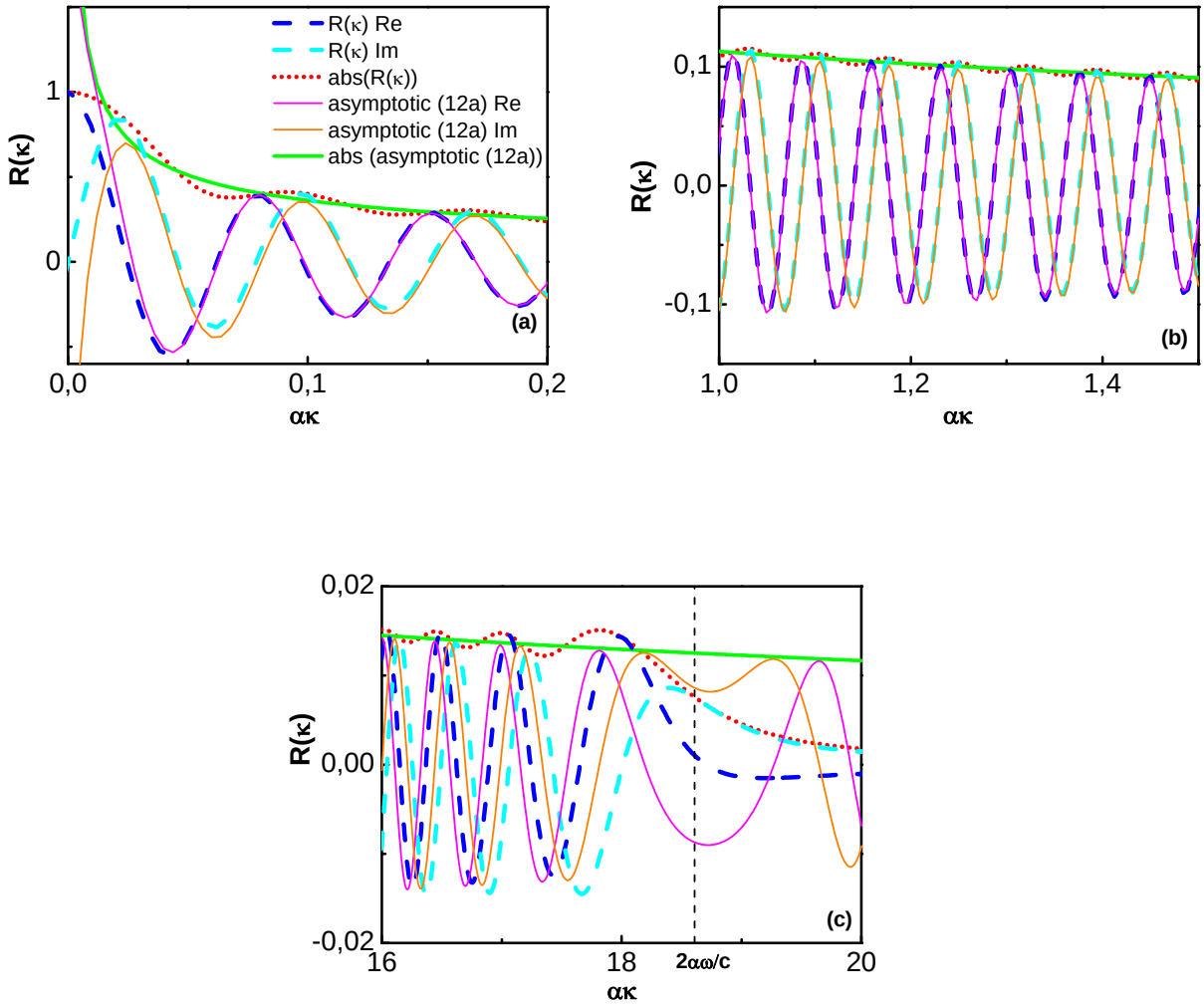

Figure 2.7. The comparison of real, imaginary parts and modules of analytical approximation (123) (solid lines) and numerically calculated partial amplitude $\tilde{R}(\kappa)$ ((a) – (c)) (dotted lines) shown in relative units, the vertical dashed line shows the value $\kappa = 2\omega/c$ in (c).

The comparison of the partial amplitude directly computed from the Helmholtz equation using (92) and its approximation (123) is shown in figure 2.8., where $L_0 = 0.304m$, $f = 42.9GHz$ and $\alpha_n = 0.007203m$. In the range $\alpha\kappa \le 1$ one can observe that the asymptotic form precisely coincides with the partial amplitude. However, the partial amplitude could not be described by the formula (123) for $1/\alpha_n << |\kappa| < 2\omega/c$, as it is seen in figure 2.8.(c).

Thereby it is possible to draw a conclusion that both the approximations (122) and (123) could be utilized to describe the scattering signal partial amplitude with a sufficient accuracy.

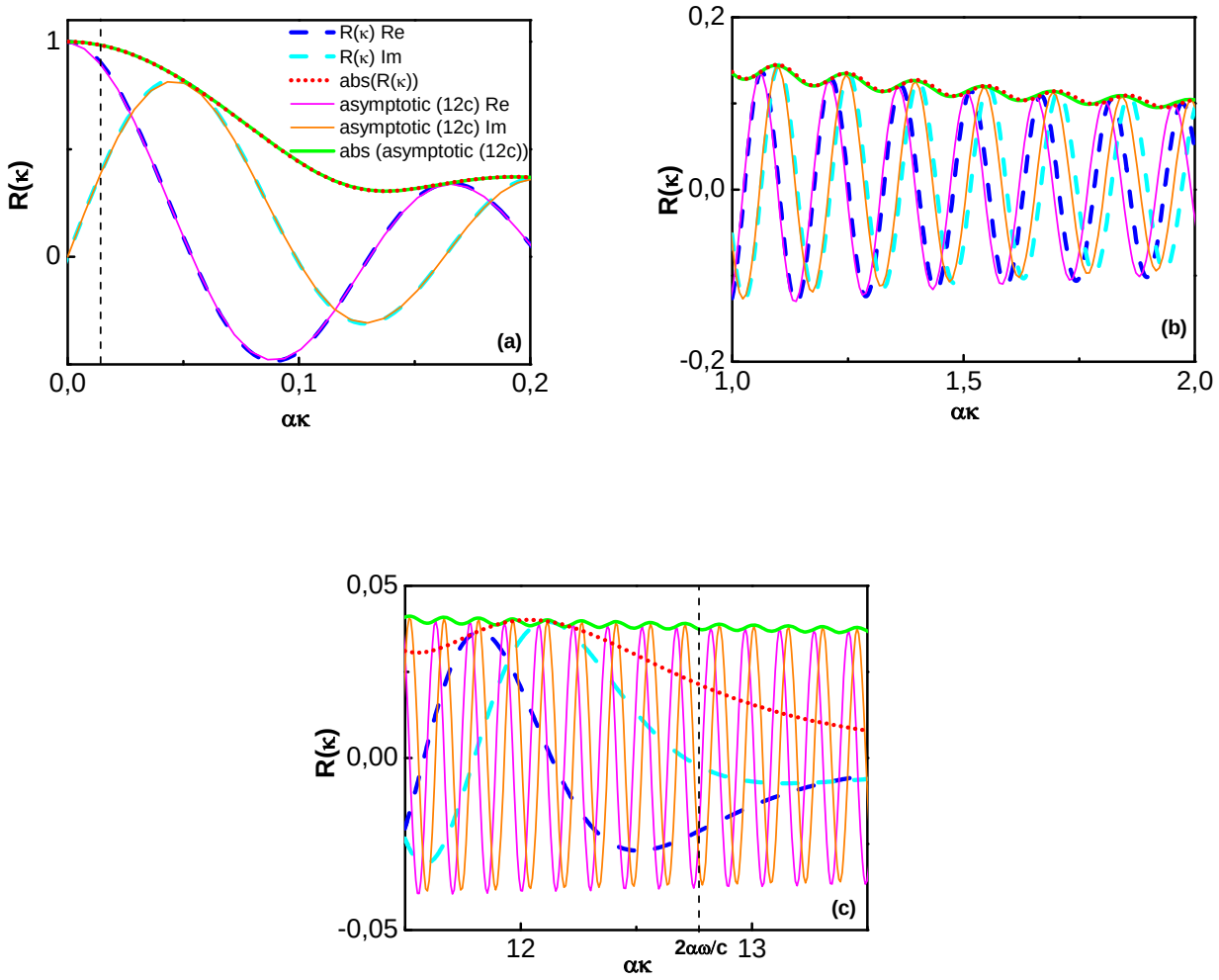

Figure 2.8. The comparison of real, imaginary parts and modules of analytical approximation (123) (solid lines) and numerically calculated partial amplitude $\tilde{R}(\kappa)$ ((a) – (c)) (dotted lines) shown in relative units, the vertical dashed line shows the values $\kappa = 1/L_n$ in (a) and $\kappa = 2\omega/c$ in (c)

2.7.2. Short summary on validity domain of Helmholtz equation solutions

In case of linear plasma density profile the precise solution of the unperturbed equation is the Airy function. In presence of small fluctuations $\delta n/n < 1\%$ the linear (Born) approximation

is valid and the perturbation theory could be applied. The analytical solution derived in part 2.6 describes the scattering wave up to the cut-off.

The WKB representation of the Airy function has been used as another approach to obtain the solution of the perturbed equation (45). The WKB approximation and its limitations were described in sub-section 2.1.3.1. In case of arbitrary plasma density profile the only way to obtain analytical solution is to apply WKB approximation. In the vicinity of cut-off where it is no more valid the behavior of scattering signal has no analytical description and the solution of the equation (45) is given by numerical computations.

2.8. The RCR CCF

In this section we derive the analytical formula expressing the RCR CCF in terms of the turbulence spectrum for both linear and arbitrary plasma density profiles. In order to carry out the correlation analysis expressions for scattering signals at different probing frequencies are used. The correlation decay of two scattering signals with growing difference of probing frequencies is studied. We introduce the RCR CCF as

$$CCF(\omega) = \left\langle \left(A_s(\omega_0) - \left\langle A_s(\omega_0) \right\rangle \right) \left(A_s(\omega) - \left\langle A_s(\omega) \right\rangle \right)^* \right\rangle \tag{125}$$

where averaging is held over ensemble. Thus, we choose one reference frequency ω_0 and change the probing frequency ω.

2.8.1. RCR CCF for linear plasma density profile

In case of linear density profile appealing to the formula for scattering signal and assuming statistically homogeneous turbulence for which the relation (58) holds, we finally obtain the expression for the RCR CCF in the form

$$CCF(\omega) = \int_{-\infty}^{+\infty} \left| R(\kappa) \right|^2 n_\kappa^2 e^{i\kappa \frac{L_0}{\omega_0}(\omega - \omega_0)} d\kappa \tag{126}$$

where

$$\left| R(\kappa) \right|^2 = \frac{S_i}{16\pi} \sqrt{L_0 L} \frac{(\omega_0 \omega)^2}{c^4} \begin{cases} \dfrac{1}{|\kappa|}, & 1/\alpha << |\kappa| < 2\omega/c \\ \dfrac{4}{\pi} \dfrac{erf\left(\sqrt{i\kappa L_0}\right) erf^*\left(\sqrt{i\kappa L}\right)}{|\kappa|}, & |\kappa| << 1/\alpha \end{cases} \tag{127}$$

and $\frac{L_0}{\omega_0}(\omega - \omega_0) = L - L_0$, L_0 and L are the cut-off positions for reference and probing frequencies correspondingly. Expression (127) for the partial amplitude can be simplified as it

was done for the equation (109) using asymptotic representation (110) in the intervals $1/L << |\kappa| << 1/\alpha$ and $|\kappa| << 1/L$ it can be written accordingly

$$|R(\kappa)|^2 = \frac{S_i}{16\pi}\sqrt{L_0 L}\frac{(\omega_0\omega)^2}{c^4}\begin{cases}\dfrac{1}{|\kappa|}, & 1/L << |\kappa| << 1/\alpha \\ \dfrac{4}{\pi}\sqrt{L_0 L}, & |\kappa| << 1/L\end{cases} \tag{128}$$

The $1/\kappa$ factor in the function is responsible for underlining the contribution of small angle scattering off long scale fluctuations into the RCR signal. It is important to stress here that asymptotic expression (128) correctly describes the behaviour of $|R(\kappa)|^2$ also at higher wave numbers $1/\alpha < |\kappa| < 2\omega/c$. Using the proposed asymptotic form (109) for scattering signal we obtain the following representation of the CCF in terms of the turbulence spectrum

$$D^{-1}\cdot CCF(L) = \int_{-\infty}^{+\infty}\frac{d\kappa}{|\kappa|}n_\kappa^2 e^{i\kappa(L_0-L)}erf\left(\sqrt{i\kappa L_0}\right)erf^*\left(\sqrt{i\kappa L}\right) \tag{129}$$

where

$$D = \frac{S_i}{4\pi^2}\sqrt{L_0 L}\frac{(\omega_0\omega)^2}{c^4} \tag{130}$$

The $1/\kappa$ singularity in this formula saturates for small wave numbers due to the term $erf\left(\sqrt{i\kappa L_0}\right)erf^*\left(\sqrt{i\kappa L}\right)$. The dependence of CCF on the probing wave cut-off position can be obtained in experiment by sweeping the probing frequency.

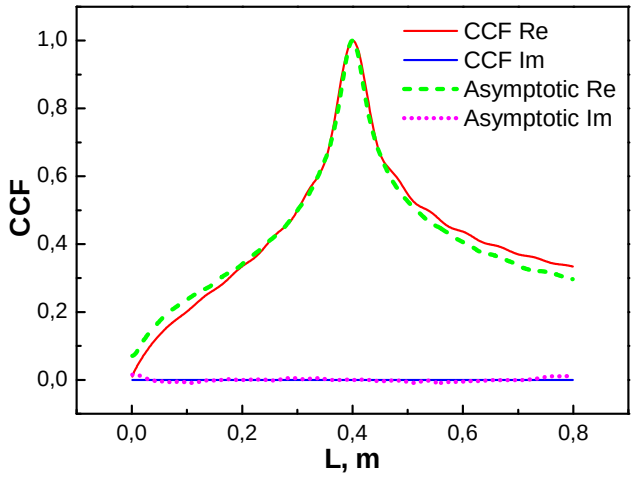

Figure 2.9. The comparison of analytical approximations (127) (dashed line real part and dotted line imaginary part) and the CCF (solid line real part and thin dotted line imaginary part) numerically calculated in Born approximation. $L_0 = 0.4m$, $f_0 = 95GHz$, Gaussian spectrum, $l_c = 0.02m$.

To check the approximate formula (128) we compare it after normalization to the CCF calculated using the Born approximation formula (92). The random density fluctuation is taken in the form

$$\delta n(x) = \sum_{j=0}^{j=N_s} \delta n_{jq} \cos(jqx - \varphi_j) \tag{131}$$

in which $\delta n_{jq} = \delta n_0 \, \mathrm{e}^{-\frac{(jq)^2 l_c^2}{4}}$ corresponds to the Gaussian turbulence correlation function possessing correlation length $l_c = 0.02m$ and phases φ_j were randomly distributed in the interval $[0, 2\pi]$. The averaging is performed over ensemble of N_s=1000 random phase samples. The calculation parameters are as follows: $L_0 = 0.4m$; $f_0 = 95GHz$. The result of comparison is shown in figure 2.9. illustrating the applicability of the proposed formula for the wide probing range.

Formula (128) can be used to compute the signal CCF for different spectra in order to compare to CCF obtained in experiments and to determine real turbulence spectra as a result of fitting procedure. However we demonstrate in section 2.9 the possibility of strict analytical inversion of the integral relation (128) and derive a formula which allows correct wave number spectrum reconstruction from RCR experimental data.

2.8.2. RCR CCF for arbitrary plasma density profile

In case of the arbitrary profile we derive the expression for the signal CCF referring to the formulae (122)-(124) for scattering signals in arbitrary profile case. Thus, we multiply the scattering signals for reference and probing frequencies. Subject to short-wave case let us consider the difference of two signal exponents.

$$\Delta = 2\left(\int_{x_c}^{x_B} k(x')dx' - \int_{x_c}^{x_{B0}} k_0(x')dx' \right) + i\kappa(x_{B0} - x_B) \tag{132}$$

Utilizing Taylor series expansion we obtain

$$\int_{x_c}^{x_B} k(x', \omega)dx' = \left(\int_{x_c}^{x_B(\omega_0)} \frac{dk(x')}{d\omega}\Big|_{\omega_0} dx' + k(x', \omega_0)\frac{dx}{d\omega}\Big|_{\omega_0} \right) \cdot (\omega - \omega_0) + \int_{x_c}^{x_{B0}} k(x', \omega_0)dx' \tag{133}$$

Using Bragg condition we consider $\kappa = 2k(x', \omega)$. Mention that $x_B(\omega_0) = x_{B0}$ and $\frac{dx_B}{d\omega}\Big|_{\omega_0} \cong \frac{x_B - x_{B0}}{\omega - \omega_0}$ we derive:

$$\Delta = 2(\omega - \omega_0) \int_{x_c}^{x_{B0}} \frac{dk(x')}{d\omega}\Big|_{\omega_0} dx' = 2t_d(\kappa)(\omega - \omega_0) \tag{134}$$

where

$$t_d(\kappa) = \int_{x_c}^{x_B(\kappa)} \left. \frac{\partial k(x')}{\partial \omega} \right|_{\omega} dx' \tag{135}$$

is the probing wave propagation time between the cut-off and the Bragg resonance point. In case of long scale fluctuations satisfying condition $2\omega/c >> |\kappa| > 2/\alpha_n$ the density profile between the cut-off and the Bragg resonance point can be considered as linear, so that the delay time in expression (134) takes a form

$$t_d(\kappa) = \kappa \frac{L_0}{2\omega_0} \tag{136}$$

The expression for RCR CCF takes the form:

$$CCF(\omega) = \int_{-\infty}^{+\infty} \left|\tilde{R}\right|^2 (\kappa) n_\kappa^2 e^{i2t_d(\kappa)(\omega-\omega_0)} d\kappa \tag{137}$$

where

$$\left|\tilde{R}(\kappa)\right|^2 = \frac{S_i}{2048\pi^2} \frac{\left(\omega_0 \omega\right)^2}{c^4} \begin{cases} \sqrt{\dfrac{n_{c0} n_c}{\left.\dfrac{dn(x)}{dx}\right|_{x_{B0}} \left.\dfrac{dn(x)}{dx}\right|_{x_B}}} \dfrac{1}{\kappa}, & \dfrac{1}{\alpha_n} << |\kappa| << 2\dfrac{\omega_0}{c} \\ \dfrac{4}{\pi} \sqrt{L_{n0} L_n} \dfrac{1}{\kappa}, & \dfrac{1}{L_{n0}} << |\kappa| < \dfrac{1}{\alpha_n} \end{cases} \tag{138}$$

Analogous to formulae (122)-(124) we consider limits of the long scale fluctuations and obtain the expression for the partial amplitude in the form:

$$\left|\tilde{R}(\kappa)\right|^2 = \frac{S_i}{2048\pi^2} \frac{\left(\omega_0 \omega\right)^2}{c^4} \begin{cases} \displaystyle\int_0^{x_{c0}} \frac{e^{i\kappa x_0 + 2t_d(\kappa)\omega_0} dx_0}{\sqrt{1 - \dfrac{n(x_0)}{n_c}}} \int_0^{x_c} \frac{e^{-i\kappa x - 2t_d(\kappa)\omega} dx}{\sqrt{1 - \dfrac{n(x)}{n_c}}}, & \dfrac{1}{x_{nc}} < |\kappa| << \dfrac{1}{\alpha_n} \\ \displaystyle\int_0^{x_{n0}} \frac{e^{2t_d(\kappa)\omega_0} dx_0}{\sqrt{1 - \dfrac{n(x_0)}{n_c}}} \int_0^{x_n} \frac{e^{-2t_d(\kappa)\omega} dx}{\sqrt{1 - \dfrac{n(x)}{n_c}}}, & |\kappa| << \dfrac{1}{x_{nc}} \end{cases} \tag{139}$$

At small fluctuation wave number $2\omega/c >> |\kappa| > 2/\alpha_n$ the Bragg backscattering point is located close to the cut-off ($|x_c - x_B|/x_c << 1$), where we may approximate the density profile by the linear dependence. The propagation time in this case is given by expression (136). In (139) the additional dependence on wave number is hidden in the dependence of the Bragg backscattering point $x_B(\kappa)$. However at $2\omega/c >> |\kappa| > 2/\alpha_n$ in case the density profile can be supposed linear, formula (139) in the region $1/x_{nc} < |\kappa| << 1/\alpha_n$ smoothly transforms into the region $|\kappa| << 1/x_{nc}$ and coincides with (122)-(124). In this wave number domain equation (137) appears to be similar to (126).

2.9. Turbulence spectrum reconstruction from the RCR CCF

In this section the main result of this thesis is derived.

Essentially, the formula (129) shows that the expression for CCF in case of linear density profile looks similar to Fourier transform of the function n_κ^2. It differs from Fourier transform of turbulence spectrum only because of weak dependence of the error function $erf\left(\sqrt{i\kappa L}\right)$ on the probing wave cut-off position. Inversion of integral equation (129) giving the expression for turbulence wave number spectrum can be obtained after converting it into the Abel equation.

We treat the integral equation (129) by applying Fourier transform and obtain

$$\frac{1}{2\pi}\int_{-\infty}^{+\infty}\frac{CCF(L)}{\sqrt{L}}e^{iLy}dL=\frac{e^{i\frac{\pi}{4}}}{2\pi}\int_{-\infty}^{+\infty}\left(\int_{-\infty}^{+\infty}\frac{d\kappa}{\sqrt{|\kappa|}}n_\kappa^2 e^{i\kappa(L_0-L)}erf^*\left(\sqrt{i\kappa L_0}\right)\int_0^1 e^{-i|\kappa L|p^2}dp\right)e^{iLy}dL \qquad (140)$$

Left part of the equation (140) can be denoted as

$$F(y)=\frac{1}{2\pi}\int_{-\infty}^{+\infty}\frac{CCF(L)}{\sqrt{L}}e^{iLy}dL \qquad (141)$$

Expressing the internal $\int_{-\infty}^{+\infty}e^{iL(y-\kappa-\kappa p^2)}dL$ as the Dirac $\delta-$function we find

$$F(y)=\frac{e^{i\frac{\pi}{4}}}{2\pi}\int_{-\infty}^{+\infty}\int_0^1\frac{d\kappa}{\sqrt{|\kappa|}}n_\kappa^2 erf^*\left(\sqrt{i\kappa L_0}\right)e^{i\kappa L_0}\frac{\delta\left(\kappa+\frac{y}{1-p^2}\right)}{\left|1-p^2\right|}dpd\kappa \qquad (142)$$

Using the Dirac $\delta-$function features we substitute $\kappa=-\frac{y}{1-p^2}$ and obtain

$$F(y)=\frac{e^{i\frac{\pi}{4}}}{2\pi}\int_0^1 n^2_{\frac{y}{1-p^2}}\frac{erf^*\left(\sqrt{i\left|\frac{yL_0}{1-p^2}\right|}\right)}{\sqrt{\left|\frac{y}{1-p^2}\right|}}e^{i\frac{yL_0}{1-p^2}}\frac{dp}{\left|1-p^2\right|} \qquad (143)$$

After variable exchange $t=\frac{y}{1-p^2}$ the equation (143) takes a form of the Abel equation:

$$F(y)=\frac{e^{i\frac{\pi}{4}}}{4\pi}\begin{cases}\int_y^{+\infty}n_t^2\frac{erf^*\left(\sqrt{itL_0}\right)}{t\sqrt{t-y}}e^{-itL_0}dt, & y\geq 0\\ \int_{-\infty}^{y}n_t^2\frac{erf^*\left(\sqrt{-itL_0}\right)}{t\sqrt{y-t}}e^{-itL_0}dt, & y<0\end{cases} \qquad (144)$$

The solution of the Abel equation is found as

$$n_\kappa^2 = 4e^{-i\frac{\pi}{4}} \begin{cases} \dfrac{\kappa e^{-i\kappa L_0}}{erf^*\sqrt{i\kappa L_0}} \dfrac{d}{d\kappa} \displaystyle\int_\kappa^{+\infty} \frac{F(y)}{\sqrt{y-\kappa}} dy, & \kappa \geq 0 \\ \dfrac{\kappa e^{-i\kappa L_0}}{erf^*\sqrt{-i\kappa L_0}} \dfrac{d}{d\kappa} \displaystyle\int_{-\infty}^{\kappa} \frac{F(y)}{\sqrt{\kappa-y}} dy, & \kappa < 0 \end{cases} \tag{145}$$

Changing variables $p = y - \kappa$ and substituting the expression (141) into (145) we obtain

$$n_\kappa^2 = \frac{2}{\pi} e^{-i\frac{\pi}{4}} \frac{\kappa e^{-i\kappa L_0}}{erf^*\sqrt{i\kappa L_0}} \frac{d}{d\kappa} \int_0^{+\infty} \frac{1}{\sqrt{p}} \int_{-\infty}^{+\infty} \frac{CCF(L)}{\sqrt{L}} e^{iL(p+\kappa)} dL dp \tag{146}$$

Integral over p there is taken explicitly

$$\int_0^{+\infty} \frac{dp}{\sqrt{p}} e^{iLp} = \frac{2e^{i\frac{\pi}{4}}}{\sqrt{L}} \int_0^{+\infty} e^{-s^2} ds = e^{i\frac{\pi}{4}} \sqrt{\frac{\pi}{L}} \tag{147}$$

Differentiating the expression (147) over κ finally we obtain the expression for the wave number spectrum:

$$\boxed{n_\kappa^2 = D^{-1} \cdot \frac{2}{\sqrt{\pi}} \frac{\kappa}{erf^*\left(\sqrt{i\kappa L_0}\right)} \int_{-\infty}^{+\infty} CCF(\Delta L) e^{i\kappa \Delta L} d\Delta L} \tag{148}$$

where $\Delta L = L - L_0$ is the distance between the cut-off positions for reference and probing frequencies. Formula (148) is one of the main results of this thesis. It suggests the procedure of wave number spectrum reconstruction from RCR experimental data.

In figure 2.10. for the same parameters as in figure 2.6. we show the weighting coefficient

$$S(\kappa) = \frac{\kappa}{erf^*\sqrt{i\kappa L_0}} \tag{149}$$

in region $|\kappa| < 1/\alpha$ this function behaves as $S(\kappa) \propto \sqrt{\kappa}$.

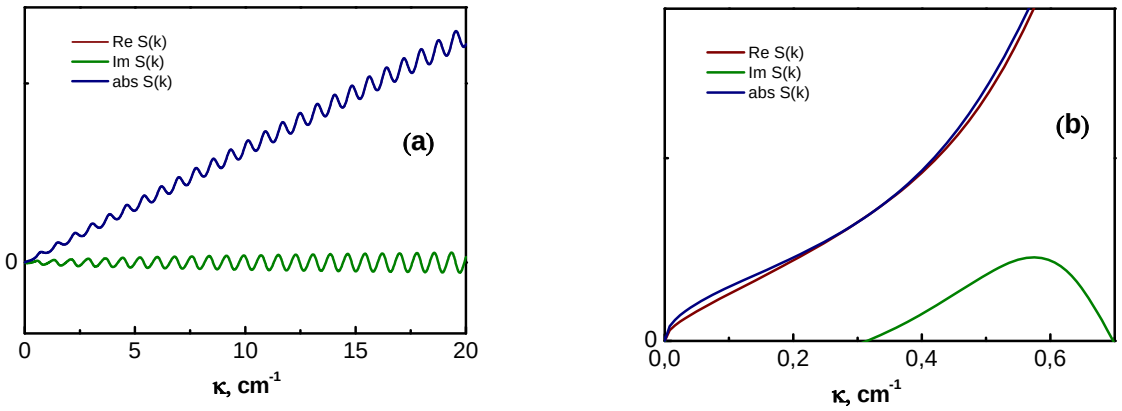

Figure 2.10. (a) Function $S(\kappa)$; (b) $S(\kappa) \propto \sqrt{\kappa}$ at $|\kappa| < 1/\alpha$.

Multiplication by the function $S(\kappa)$ will result in shortcoming of 1D theory as $n_\kappa^2(0)=0$ leading to inaccuracy of spectrum reconstruction. Nevertheless as we show in Chapter III by numerical simulations in most RCR experiments the suggested formula gives rather precise reconstruction of turbulence properties.

So far as we use the Born approximation to derive the formula (148) it is applicable only at low enough fluctuation amplitude when the reflected wave phase modulation is not strong. The corresponding criteria of the linear regime proposed in [110] and [111] takes a form:

$$\frac{\omega^2 x_c l_c}{c^2}\frac{\delta n^2}{n_c^2}\ln\frac{x_c}{l_c} << 1 \tag{150}$$

It should be noted that the expression for CCF (137) obtained in arbitrary profile case takes a form of nearly Fourier transform as well. Therefore one may expect that inverse Fourier transform of CCF given by

$$S(q)=\int_{-\infty}^{+\infty} CCF(\omega)\,\mathrm{e}^{iqL_0\frac{\omega_0-\omega}{\omega_0}}\,d\left(\omega-\omega_0\right) \tag{151}$$

can be used for turbulence spectrum reconstruction from experimental data.

2.10. Direct transform formulae for RCR

This section addresses the theoretical expression for integral kernel, which converts directly the correlation function $CCF(\Delta L)$ into the two-point CCF of plasma turbulence $C(r)$ should be quite useful for experimentalists in order to compute TCCF avoiding error accumulation during two-step conversion. Inverse transformation is also discussed.

2.10.1. Forward transformation kernel

Expression (148) allows to compute the turbulence radial wave number spectrum from the signal CCF measured in experiment. The TCCF $C(r)$ is related to the spectrum by Fourier transformation

$$C(r)=\int_{-2\omega/c}^{2\omega/c} n_\kappa^2 e^{-i\kappa r}\,d\kappa \tag{152}$$

where integration is held within Bragg backscattering limits $-2\omega/c<\kappa<2\omega/c$.

We propose the integral transformation to compute the TCCF straight from the signal CCF on purpose to avoid the error accumulated during numerical procedure of turbulence spectrum reconstruction and further Fourier transformation and to provide a simple formula determining TCCF directly from reflectometry measurements.

When substituting the expression (148) for the spectrum into the expression (152) the expression for a forward transformation of signal CCF into the TCCF in a simple form of convolution is obtained

$$C(\hat{r}) = \int_{-1}^{1} \hat{A} \cdot CCF(\Delta\hat{L})\ K(\hat{r} - \Delta\hat{L}) d\Delta\hat{L} \tag{153}$$

where a spatial variable $\hat{L} = \frac{L}{L_0}$ and a wave number variable $\hat{\kappa} = \kappa L_0$ are normalized to the reference frequency cut-off position. Integration is performed over the interval where the signal CCF is defined. The coefficient

$$\hat{A} = \frac{8\pi^{3/2} e^{i\pi/2}}{S_i} \frac{\alpha^6}{L_0^4} \left(1 + \Delta\hat{L}\right)^{-5/2} \tag{154}$$

is calculated from the expression for the coefficient (130) taking into account the relation $\Delta\hat{L} = \Delta\omega/\omega_0$ for linear plasma density profile and Airy scale.

The expression for the forward transformation kernel is given in the form of Fourier transform:

$$K(\hat{r} - \Delta\hat{L}) = \int_{-2\omega/c}^{2\omega/c} e^{-i\hat{\kappa}(\hat{r} - \Delta\hat{L})} \left[e^{i\frac{\pi}{2} sign(\hat{\kappa})} \frac{\left|\hat{\kappa}\right|}{erf^*\left(\sqrt{i\hat{\kappa}}\right)} \right] d\hat{\kappa} \tag{155}$$

The converted function is performed by an anti-symmetric fast oscillating complex function, which gives after being processed by Fourier transform, the real function of the kernel. The integration limits depend on the probing frequency ω which in its turn is related to the distance between the cut-off positions as $\omega = \omega_0(1 + \Delta\hat{L})$ for linear plasma density profile.

2.10.2. Numerical simulation example of forward kernel usage

To illustrate possibilities of this method, we simulate a case close to FT-2 tokamak experiment with the following parameters: linear plasma density profile, reference cut-off position $L_0 = 0.08m$, reference probing frequency $f_0 = 45GHz$ and Gaussian radial wave number spectrum $n_\kappa^2 = \sqrt{\pi} l_c e^{-l_c^2 \kappa^2/4}$, where correlation length is $l_c = 0.004m$. In this case, Airy scale length is equal to $\alpha = 0.0045m$.

In figure 2.11. an example of computation of forward transformation kernel $K(\hat{r})$ in relative units versus normalized distance from the cut-off position is shown. As it is seen the kernel represents oscillatory behavior which comes from integration limits corresponding to Bragg backscattering limits. Vertical dashed lines express the interval $-L_0 < \Delta L < L_0$ where the signal CCF is defined. The kernel has two characteristic scales. One is the sharp peak near the zero-

separation limit. The other is the long and logarithmic tail, which has characteristic scale of the global density gradient.

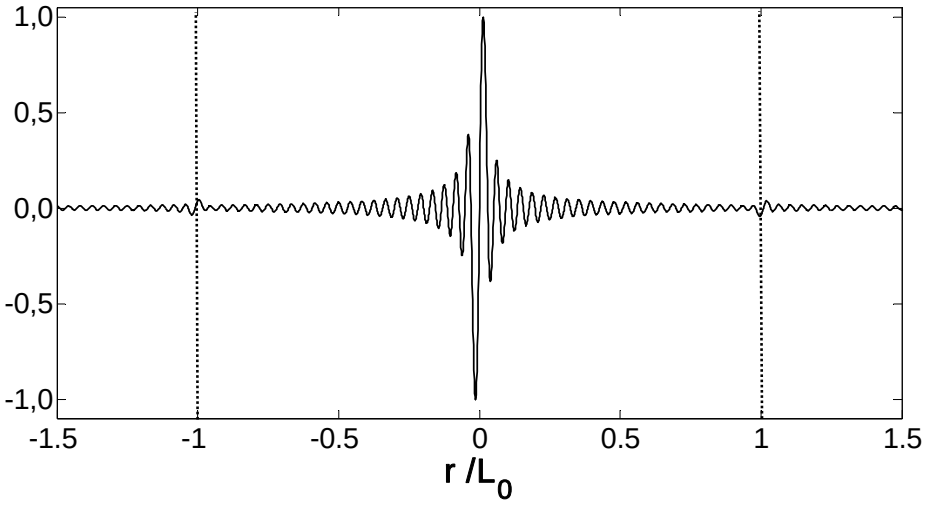

Figure 2.11. The kernel of normalized forward transformation shown in relative units versus normalized distance from the cut-off position. Vertical dashed lines express the interval $-L_0 < \Delta L < L_0$.

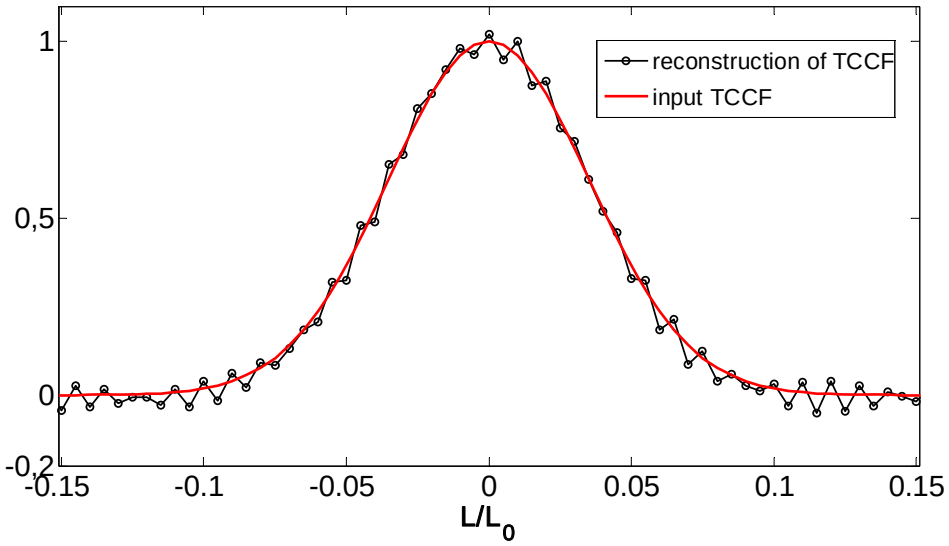

Figure 2.12. An example of TCCF computed using forward transform shown by red line marked with circles versus normalized distance from the reference cut-off position.

In figure 2.12. we demonstrate the conversion of the signal CCF into the TCCF. Formula (153) is applied to the signal CCF which is computed using formula (129), the result of the conversion is shown by thin solid line marked with circles. The computed signal CCF was given in figure 2.9. This reconstructed TCCF is compared to the initial Gaussian TCCF (thick solid line). It is confirmed that the operator equation is able to reproduce the TCCF, although the signal CCF is associated with the long tail. The signal CCF is defined on the finite interval and possesses a subsequent discontinuity at $\Delta L = L_0$ (see figure 2.14, green line) which causes oscillations (in the scale lengths shorter than c/ω) in computed TCCF.

We would like to stress that the experimental signal CCF is measured on finite distance between probing frequency cut-offs as well as on finite probing interval. In this case one should apply numerical procedures of interpolation and extrapolation by exponential function to avoid discontinuities; an explicit demonstration of such procedures will be given in Chapters III and IV. We should also note that simplifying transformation thus additional complexity associated with integration of rapidly oscillating functions is introduced.

2.10.3. Inverse transformation kernel

Inverse procedure of transformation is also based on formula (129). We substitute the expression for the radial wave number spectrum as a Fourier transformation of the TCCF into equation (129):

$$n_\kappa^2 = \frac{1}{2\pi}\int_{-L_0}^{L_0} C(r)e^{i\kappa r}dr \tag{156}$$

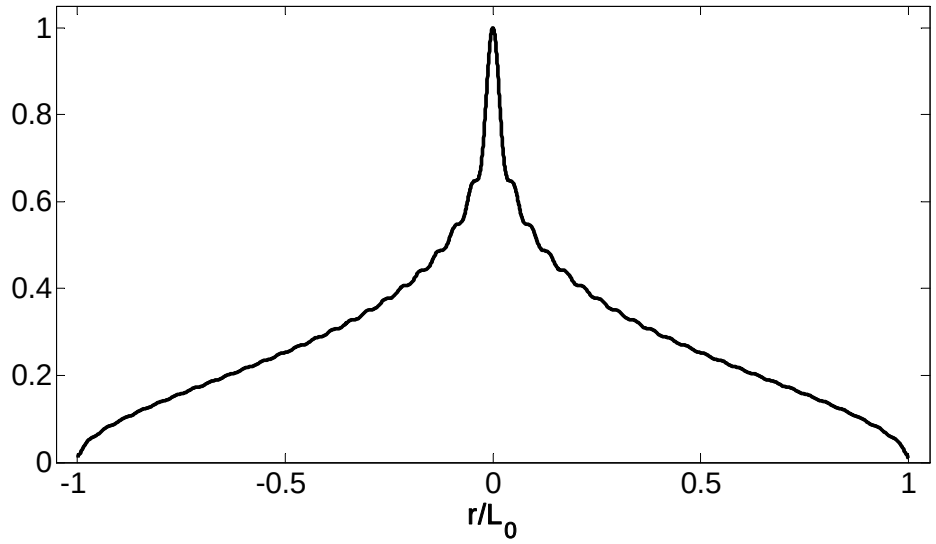

Figure 2.13. The kernel of the normalized inverse transformation.

Integration here is held over the interval where the TCCF is defined. The expression for the inverse transformation takes the following form

$$CCF(\Delta\hat{L}) = \int_{-1}^{1} \hat{B}\cdot C(\hat{r})\ U(\hat{r}-\Delta\hat{L})d\hat{r} \tag{157}$$

where the normalized coefficient $\hat{B}$ is

$$\hat{B} = \frac{S_i}{8\pi^3}\frac{L_0^4}{\alpha^2}\left(1+\Delta\hat{L}\right)^{5/2} \tag{158}$$

and the expression for the kernel is described by

$$U(\hat{r}-\Delta\hat{L})=\int_{-2\omega/c}^{2\omega/c}\frac{d\kappa}{\left|\hat{\kappa}\right|}e^{i\hat{\kappa}(\hat{r}-\Delta\hat{L})}erf\left(\sqrt{i\hat{\kappa}\widehat{L_0}}\right)erf^*\left(\sqrt{i\hat{\kappa}(\widehat{L_0}+\Delta\hat{L})}\right) \tag{159}$$

that seems to be similar to Fourier transformation however this kernel possesses the dependence on ΔL in the argument of complex conjugate error function. Integration is performed in Bragg backscattering limits as was mentioned in the previous sub-section.

Figure 2.13. shows the normalized inverse transformation kernel $U(\hat{r})$ in relative units versus normalized distance from the cut-off position. The function decays logarithmically therefore the long range tail is introduced into the signal CCF computed using formula (157).

2.11. Ideas for a combined diagnostic using reflectometry and other density fluctuation diagnostic

In this section we consider correlation between the reflectometry signal and other local fluctuation measurement such as HIBP in order to simplify the procedure of data processing and to open new approaches of reflectometry usage. The reason for this prediction is provided by different behavior of complementary diagnostic sensitivity to long wave length fluctuations, which was supposed homogeneous, whereas for reflectometry it is growing towards small wave numbers. It is also necessary to stress that nowadays no experiment exists for applying this new kind of turbulence characterization.

We represent the correlation by inter–correlation function (ICF) $ICF(\Delta L)$ where L_0 denotes the position of local measurement and L indicates the position of the reflection for reflectometry. It is shown that the long range tail of correlation which is much longer than the correlation length of turbulence persists in $ICF(\Delta L)$ (see figure 2.14.), however it decays faster than that of $CCF(\Delta L)$. We propose formulae to compute wave number spectrum and spatial TCCF from these measurements.

The interest to define expressions of ICF is to change the dependencies of CCF, and if it is possible to reduce the contribution of the long wavelength in the CCF as it will be shown. In this sub-section we develop theoretically the method of data interpretation of combined reflectometry and other local diagnostics (e.g.HIBP). We introduce ICF as

$$ICF(\Delta L)=<\delta n(L_0)A_s^*(L_0+\Delta L)> \tag{160}$$

between the reflectometry signal $A_s(L_0+\Delta L)$ and one other local fluctuation measurement $\delta n(L_0)$ in linear regime, $\delta n(L_0)/n(L_0)\approx 1\%$. We also assume that reflectometry and other fluctuation diagnostic measurements can be held simultaneously.

We modify formula (129) according to the expression for ICF in the following way:

$$P^{-1}\cdot CCF(\Delta L)=\int_{-\infty}^{+\infty}\frac{d\kappa}{\sqrt{|\kappa|}}n_\kappa^2 e^{-i\kappa\Delta L}erf^*\left(\sqrt{i\kappa(L_0+\Delta L)}\right) \tag{161}$$

where the coefficient P is equal to

$$P=\frac{\sqrt{S_i}}{2\pi}\sqrt{(L_0+\Delta L)}\frac{(\omega_0+\Delta\omega)^2}{c^2} \tag{162}$$

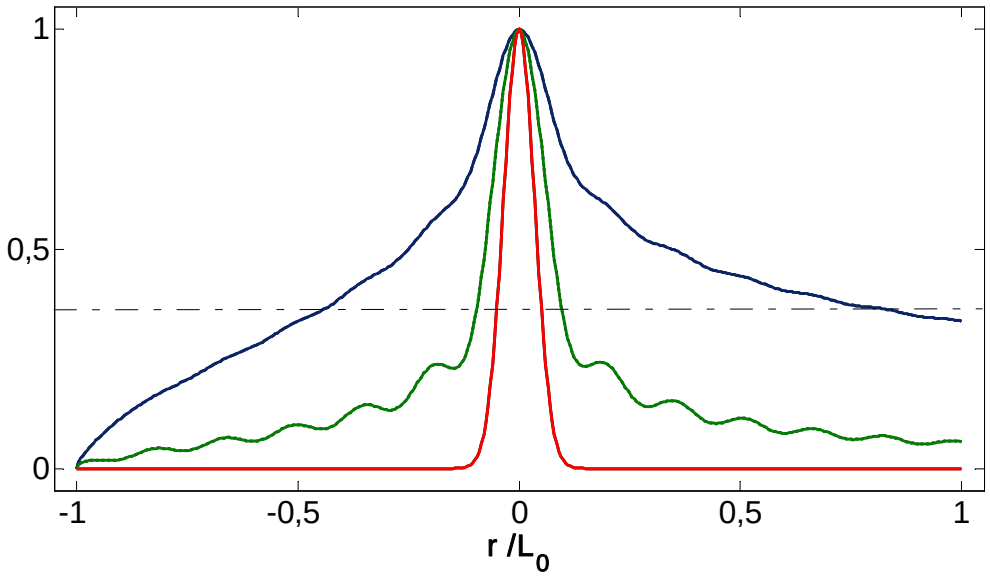

Figure 2.14. Comparison of TCCF (red line), ICF (green line) and signal CCF (blue line). Horizontal dashed line shows the *1/e* CCF level.

In figure 2.14. we show the comparison of Gaussian TCCF (red line), ICF (green line) given by expression (160) and signal CCF (blue line) given by expression (129) versus normalized distance between fluctuation measurement and the cut-off position of the probing frequency. Horizontal dashed line shows the *1/e* CCF level. Signal CCF demonstrates slow logarithmical decay. The dependency of the ICF on the wave number is no more singular and it decays faster comparing to the signal CCF however it is still not possible to determine the TCCF or at least turbulence correlation length directly from the measurements.In the present paper we give a method to determine spatial TCCF from the ICF. Similarly to computations performed in section 2.9 we derive an expression for the radial wave number spectrum in terms of ICF:

$$n_\kappa^2=\sqrt{\pi}e^{i\frac{\pi}{2}(1+sign(\kappa))}\sqrt{\kappa}\left[\int_{-\infty}^{+\infty}\left[P^{-1}\cdot CCF(\Delta L)\right]e^{-i(L_0+\Delta L)\kappa}d\Delta L\right] \tag{163}$$

2.11.1. Forward and inverse transforms for ICF

We derive the expressions for the forward and inverse transforms of the ICF into TCCF.

Thus, we substitute the expression for the spectrum (163) into Fourier transformation (152) and obtain the expression for the TCCF in form of convolution

$$C(r) = \int_{-L_0}^{L_0} \left[A \cdot CCF(\Delta L) \right] K(r + \Delta L) d\Delta L \tag{164}$$

where the expression for the forward transformation kernel is given by the integral

$$K(r + \Delta L) = \int_{-2\omega/c}^{2\omega/c} \sqrt{\kappa} e^{-i(r+\Delta L)\kappa} d\kappa \tag{165}$$

and the coefficient A is equal to

$$A = \sqrt{\pi} e^{i\frac{\pi}{2}(1+sign(\kappa))} P^{-1} \tag{166}$$

The expression for the inverse transformation is computed by substituting the equation (156) into relation (161)

$$CCF(\Delta L) = \int_{-L_0}^{L_0} \left[\frac{P}{2\pi} \cdot C(r) \right] U(r - \Delta L) dr \tag{167}$$

where the expression for the inverse transformation kernel is presented by the integral

$$U(r - \Delta L) = \int_{-2\omega/c}^{2\omega/c} \frac{d\kappa}{\sqrt{|\kappa|}} e^{i\kappa(r-\Delta L)} erf^* \left(\sqrt{i\kappa \left(L_0 + \Delta L \right)} \right) \tag{168}$$

In figures 2.15. and 2.16. we show the forward and inverse kernel functions correspondingly in relative units versus normalized distance from the fluctuation measurement position. Vertical dashed lines show the interval where the ICF is defined.

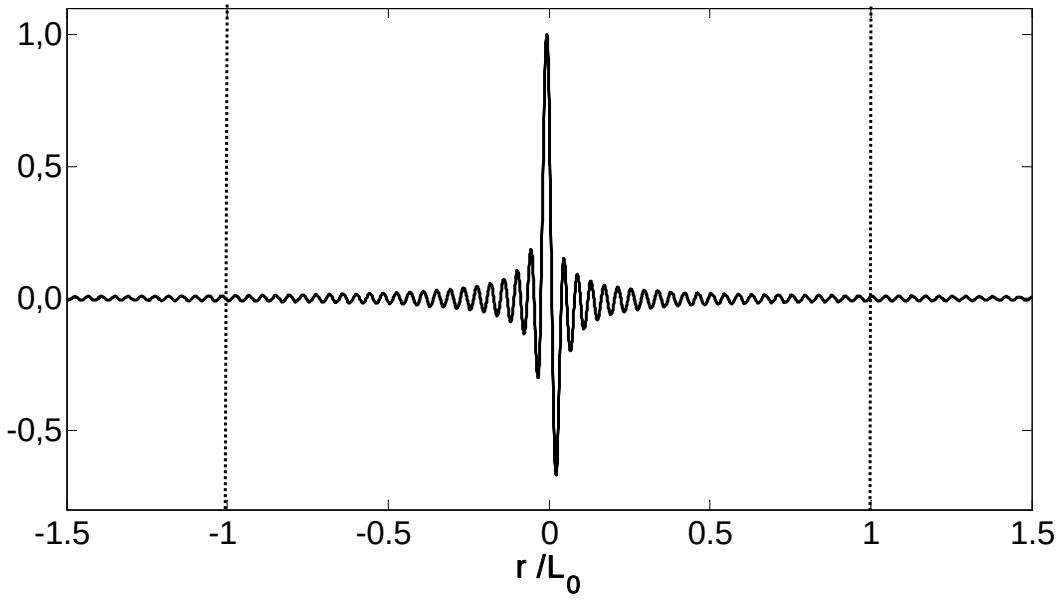

Figure 2.15. The kernel of the normalized forward transformation for ICF.

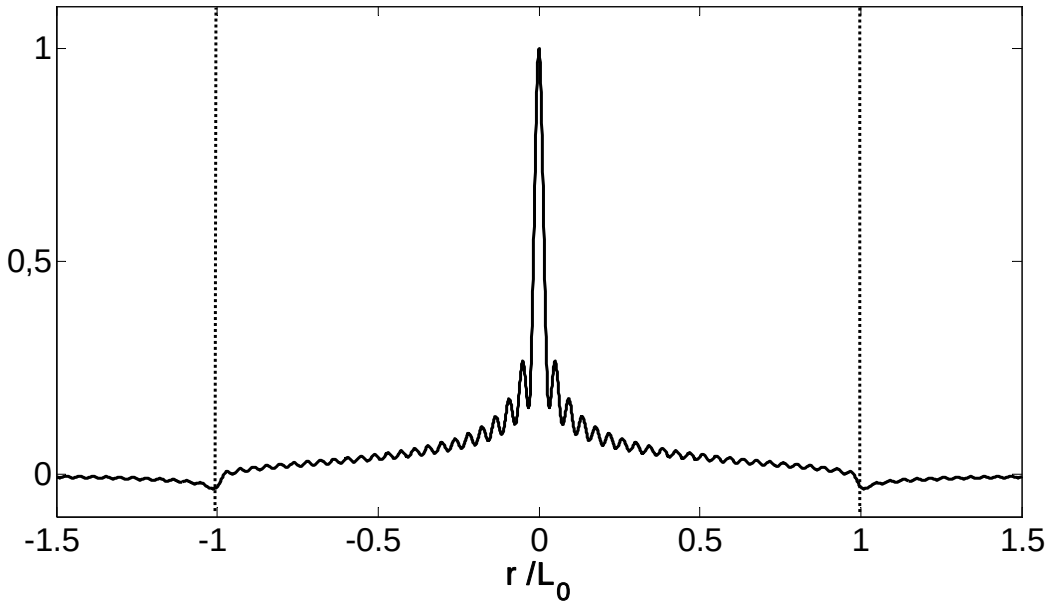

Figure 2.16. The kernel of the normalized inverse transformation for ICF.

We should underline that formulae shown in this section are derived for infinite limits however the ICF as well as the TCCF are defined on finite interval which causes difficulties in theory applications to the experiment. Moreover integration over wave number should be performed within Bragg limits. Before using the proposed method it is necessary to process the ICF in a proper way applying interpolation and extrapolation procedures.

2.12. Summary

In this chapter the new analytical theory of RCR has been presented.

Existing 2D approaches [107, 126] are quite sophisticated and as we suppose 2D effects do not strongly influence reflectometry diagnostic which is generally one-dimensional, therefore the development of 1D analytical approach is evident.

In section 2.6 the analytical solution of 1D Helmholtz equation in Born approximation for linear plasma density profile has been derived. As a result of this simple approach it was shown that scattering signal singular dependency on fluctuation wave number saturates for smaller wave number of the order of the inverse distance between plasma boundary and the cut-off position $|\kappa| << 1/L$ that is significantly smaller than Airy scale length as it was supposed in earlier analytical approach [115] as of the order of Airy scale length. As it could be seen from figure 2.17 where the comparison of the two approaches is illustrated the difference between the correct scattering signal function and the assumption of [115] can reach a factor of 10.

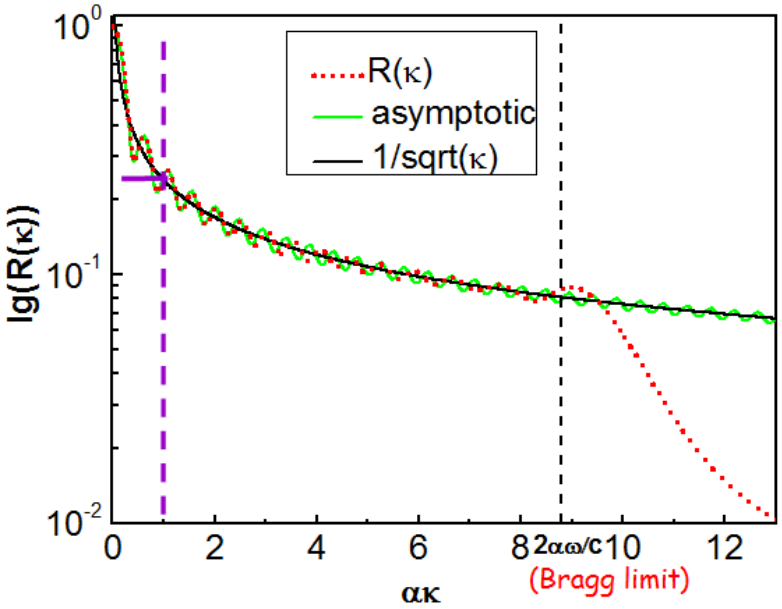

Figure 2.17. Comparison between the new analytical scattering signal representation (red line) and previous assumption (marked by solid violet line). Vertical violet dashed line signifies Airy scale at which the scattering signal dependency on wave number was supposed to saturate.

The strong scattering signal dependency proportional to $1/\sqrt{\kappa}$ in the region $1/L << |\kappa| << 1/\alpha$ missed in previous approach is in charge of long logarithmic tail in the signal RCR CCF (see figure 2.9.) numerically demonstrated in [76]. In Chapter III this result will be confirmed in 1D numerical model in Born approximation.

The same exercise was performed in WKB approximation in case of arbitrary plasma density profile which is closer to real experiment. In vicinity of the cut-off position where WKB approximation is no more valid the scattering signal is described by the Airy function.

The relation between the signal RCR CCF which could be measured in RCR experiment and the turbulence radial wave number spectrum is the primary new result of this Chapter. Despite the huge difference between correlation functions of signals and turbulence it gives a simple and correct method of experimental data interpretation. Though this inverse relation is derived in case of linear plasma density profile in O-mode it is applicable for smooth monotonic experimental profiles as well as for X-mode probing and gives satisfying result as it will be demonstrated in Chapters 4 and 5. Definitively there are restrictions for the obtained results provided by the initial assumptions made in the beginning of this chapter. Thus, the method of RCR CCF transformation is applicable in case of small level of plasma density fluctuations $\delta n/n_c < 1\%$, i.e. in linear regime, however this does not disparage the value of new formulae.

Analytical asymptotic forms and direct transforms have been confirmed by numerical computations of corresponding integrals and shown in figures 2.6. – 2.17. of this Chapter.

Direct transforms simplifying the calculation of turbulence spatial properties were also proposed in section 2.10.

Another breakthrough of the developed analytical theory is the expansion of its applications on other fluctuation diagnostics such as for example HIBP. The analytical basis of the diagnostic based on simultaneous usage of one reflectometry channel and HIBP data is developed in section 2.11. At present day there is no experiment exploiting such a method. Certainly, when setting up the experiment, one would face difficulties in data collection and interpretation nevertheless the ICF gives a commencement of this kind of investigation.

Obviously there is wide field for further research and analytical theory improvement namely connection between 1D and 2D expressions, corrections to the inverse relation due to 2D effects which are the subject of future research.

Chapter III

Numerical modeling

In this Chapter simulation results are given firstly, to validate the new theory of RCR able to access to turbulence characteristics, secondly to determine the limits and the sensitivity of the radial correlation reflectometer to different parameters encountered in experiments and possibilities of this diagnostic to detect relevant events existing in fusion plasmas. Results of reflectometry experiment numerical modeling in simplest linear plasma density profile as well as in conditions close to real experiments are presented.

3.1. Numerical model

In this sub-section the numerical code is described. The numerical model is based on the theoretical approach developed in Chapter II resulting in unperturbed differential equation (45) to be solved and further integral (99) and inversion relation (148) to be computed. The programming language Fortran is used to develop the code.

Analytical formulae are derived in Born approximation linear regime and possess no dependence on fluctuation amplitude therefore the numerical code is not sensitive to fluctuation amplitude and gives only linear solution of the Helmholtz equation.

As soon as our goal is to study the RCR diagnostic from the experimental point of view we choose the set of input parameters of the code close to experimental. The numerical procedure consists of four parts: solution of the unperturbed Helmholtz equation; partial amplitude calculation (calculation of the integral over κ); signal CCF calculation; turbulence wave number and CCF reconstruction.

3.1.1. Numerical solution of unperturbed Helmholtz equation.

Firstly, the unperturbed Helmholtz equation (45) with $\delta n(x) = 0$ is solved numerically applying finite difference scheme based on forth-order Numerov method. Finite difference method is selected due to its simplicity (less computing time) and easiness to implement. The equidistant grid with the step h is used. The solution is the unperturbed electric field $E_0^j(x, \omega^j)$ for the set of probing frequencies where j is the index of probing frequency. Initially the Helmholtz equation takes a form:

$$E_z^{(2)}(x) + 4\pi^2 N_0^2(x) E_z(x) = 0 \tag{169}$$

To solve the Helmholtz equation the 4th order Numerov scheme (see Appendix B) is used:

$$\begin{aligned} &E_z(x+h)\left[1+4\pi^2\frac{h^2}{12}N_0^2(x+h)\right] - E_z(x)\left[2-4\pi^2\frac{5h^2}{6}N_0^2(x)\right] + \\ &+E_z(x-h)\left[1+4\pi^2\frac{h^2}{12}N_0^2(x-h)\right] = 0 \end{aligned} \tag{170}$$

The Helmholtz equation is finally represented by a matrix equation:

$$\mathrm{A}\vec{E} = \vec{B} \tag{171}$$

where A is a tridiagonal matrix defined by equation (170). $\vec{B}$ is the vector defined by boundary conditions of finite amplitude in vacuum $E(xL) = 1.0$ and the evanescence of the wave behind the cut-off $E(xR) = 0.0$, thus $B_1 = -E(xL)\cdot\left[1+\frac{h^2}{12}N_0^2(xL)\right]$, $B_{2..N_x} = 0.0$. The

dimension of the matrix A is $[N_x, N_x]$, of the vectors $\vec{E}$ and $\vec{B}$ is $[N_x, 1]$. The solution of the equation is found by inverting the matrix A. In Fortran it is done by means of "DLSLTR" function.

In this part we also introduce the following physical parameters of computation:

xL	left plasma boundary
xR	right plasma boundary
$\delta\Delta$	probing step
$\omega^j = \omega(xL + j \cdot \delta\Delta)$	probing frequency
$n_e(x)$	plasma density profile
$B(x)$	magnetic field profile

and numerical parameters:

N_x	the number of integration x-grid points
h_x	x-grid step

The result of this computation is the matrix $\left[\vec{E}^1, ..., \vec{E}^{N_\omega}\right]$ containing N_ω vectors of length N_x and the matrix $\Omega = \left[\vec{\omega}, \vec{L}\right]$ containing the vector $\vec{\omega}$ of probing frequencies and the vector $\vec{L}$ of cut-off positions, both of length N_x. Equidistant interval is chosen for cut-off positions.

3.1.2. Reflectometry signal partial amplitude integral computation

Substituting the expression for the fluctuations (56) to the formula (92) we obtain:

$$A_s(\omega^j) = \frac{i\omega\sqrt{S_i}}{32\pi^2} \int_0^{+\infty} \int_{-\infty}^{+\infty} \frac{\delta n_\kappa}{n_c} \left(E^{j(0)}(\omega^j, x)\right)^2 e^{-i\kappa x} d\kappa dx \tag{172}$$

In the second part we firstly compute the integral over wave numbers changing the integration limits according to the conditions of computations:

$$I(\omega^j, \kappa_k) = \sum_{i=1}^{i=N_x} \left(E^{j(0)}(\omega^j, x_i)\right)^2 e^{-i\kappa_k x_i} \cdot h_x \tag{173}$$

The x-grid of integration is already defined by previous computations of the matrix $\left[\vec{E}^1, ..., \vec{E}^{N_\omega}\right]$. The κ-grid is defined in this part with the resolution of $2N_\kappa + 1$ points in the wave number interval $-2\omega^j/c < \kappa < 2\omega^j/c$ specified by Bragg conditions. Here we define the following parameters:

$2N_\kappa + 1$	the number of integration κ-grid points
h_κ	κ-grid step

The result of this computation is the matrix $M_\kappa = \left[\vec{\kappa}, \vec{I}(\omega^1, \kappa), ..., \vec{I}(\omega^{N_\omega}, \kappa)\right]$ containing the vector of wave numbers $\vec{\kappa}$, $\kappa_k = -2\omega^j/c + k \cdot h_\kappa$, $i = -N_\kappa ... N_\kappa$ and vectors of the integrals for each frequency ω^j and wave number κ.

Plasma fluctuations are modeled in the following way:

$$\delta n(x) = \sum_{k=-N_\kappa}^{k=N_\kappa} \sqrt{n_\kappa^2} e^{i\kappa_k x} e^{i\varphi_k^s} \tag{174}$$

where amplitude $\sqrt{n_\kappa^2}$ is distributed in accordance with the input turbulence spectrum, random phases φ_k^s are generated anti-symmetrically for the wave numbers κ_k of opposite sign and to the number of samples of averaging *s*.

Further we compute the partial amplitudes as

$$A_s(\omega^j) = \sum_{k=-N_\kappa}^{k=N_\kappa} I(\omega^j, \kappa_k) \sqrt{n_\kappa^2} e^{i\kappa_k x} e^{i\varphi_k^s} \tag{175}$$

Here we introduce one more parameter:

N_s	the number of sets of samples of averaging

The result of this part of computations is a matrix $\left[\vec{A}_s(\omega)^1, ..., \vec{A}_s(\omega)^{N_s}\right]$ containing N_s vectors of partial amplitudes for each sample of random phase. Finally, the signal is represented in terms of real and imaginary parts as $A_s(\omega) = re(A_s(\omega)) + im(A_s(\omega))$.

3.1.3. Signal CCF computation

In the third part we compute the signal CCF according to formula (125). Simplifying calculations, we normalize it in the following way:

$$\overline{CCF}(\omega^j) = \frac{\left\langle \left(A_s(\omega_0) - \langle A_s(\omega_0)\rangle\right)\left(A_s(\omega^j) - \langle A_s(\omega^j)\rangle\right)^* \right\rangle_s}{\sqrt{\left\langle \left(A_s(\omega_0) - \langle A_s(\omega_0)\rangle\right)^2 \right\rangle_s \left\langle \left(A_s(\omega^j) - \langle A_s(\omega^j)\rangle\right)^2 \right\rangle_s}} \tag{176}$$

We chose one of the frequencies ω^j to set as reference. We also chose the interval of probing which corresponds to experimental. Therefore new parameters are used:

ω_0	reference probing frequency
Δ	probing interval
N_ω	number of probing frequencies

Essentially, to compute the CCF we make the averaging numerically over random phase samples and therefore we allow numerical modeling of experimental noise. The result of the

computation is a vector $\overline{CCF}(\omega^j(\Delta L)) = \overline{CCF}(\Delta L)$, vector of probing frequencies $\vec{\omega}$ and the vector of the difference between reference and probing cut-off positions $\Delta\vec{L}$.

3.1.4. Turbulence wave number spectrum and TCCF reconstruction

In the fourth part we determine the spectrum utilizing equation (148):

$$n_{\kappa k}^2 = D^{-1} \cdot \frac{2}{\sqrt{\pi}} e^{i\frac{\pi}{2}(1+sign(\kappa))} \frac{|\kappa_k|}{erf^*\left(\sqrt{i\kappa_k L_0}\right)} \sum_{i=1}^{i=N_\omega} \overline{CCF}(\Delta L) e^{i\kappa_k \Delta L} \delta\Delta \tag{177}$$

where $\Delta L = L_0 - L^j$. The TCCF is computed utilizing simple fast Fourier Transform (152):

$$C(L^j) = \sum_{k=-N_\kappa^*}^{k=N_\kappa^*} n_\kappa^2 e^{-i\kappa_k L^j} h_\kappa^* \tag{178}$$

Output data are the vector of the wave number spectrum of the length $2N_\kappa^* + 1$ and the vector of turbulence of the length N_x^*. The new parameters of the reconstruction are introduced:

$2N_\kappa^* + 1$	the number of integration κ-grid points
h_κ^*	κ-grid step
N_x^*	the number of integration *x*-grid points

3.2. O-mode probing in case of linear plasma density profile

In this section the capabilities of the proposed procedure are shown numerically. Here we just give qualitative criteria deduced from simulations done in cases of relevant density gradient lengths for actual fusion devices.

3.2.1. Reconstruction of turbulence spectrum and CCF for large machine

An example of simulations is given for large tokamak plasma where wave propagation region width is much larger than the turbulence correlation length in the simplest linear plasma density profile case where the parameter set satisfies fully all the validity conditions of the theory.

Results of computations in this section are obtained under the following common parameters: reference frequency f_0=95.5GHz which corresponds to the reference cut-off position L_0=0.4m; the number of integration grid points is also fixed N_x=10000 and number of

wave number harmonics N_k=10000. The ratio of wave propagation region width to the vacuum wavelength in considered case is $L_0 f_0 / c \approx 127.3$.

3.2.1.1. Broad probing region and fine resolution

Firstly we consider the case without limitations by diagnostic technique parameters and we test capabilities of the method assuming the probing to be realized in plasma within the interval $\Delta = 0.8m$ corresponding to $-20l_c < \Delta L < 20l_c$, where correlation length is $l_c = 0.02m$, with spatial probing step $\delta\Delta = 0.04l_c$, which corresponds to the number of probing frequencies $N_\omega = 1000$, and introduce the number of sets of random density fluctuation phase samples N_s=500.

3.2.1.1.1. Simple Gaussian turbulence spectrum

We suppose a linear plasma density profile with the Gaussian turbulence spectrum [127] used in the analysis:

$$n_\kappa^2 = \sqrt{\pi} l_c e^{-l_c^2 \kappa^2 / 4} \tag{179}$$

The choice represents the simplest single-component one-parameter spectrum often used in numerical modeling of fluctuation reflectometry as it was described in section 1.4.3.

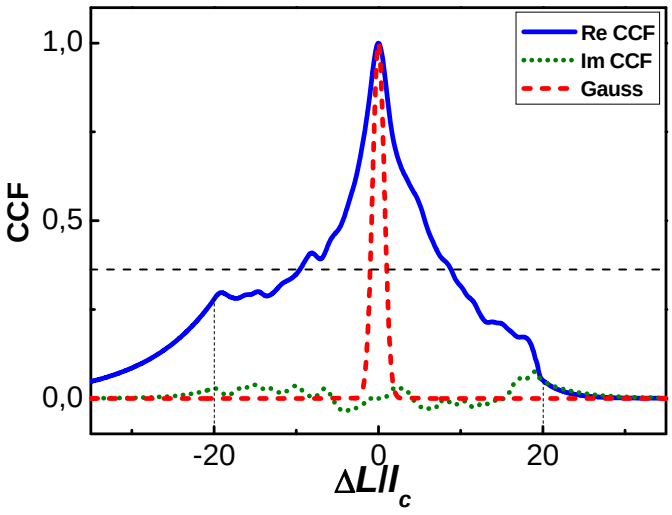

Figure 3.1. Signal CCF (real solid blue and imaginary dotted green) and input Gaussian TCCF (dashed red line) calculated in the interval $\Delta = 40l_c$. Horizontal dashed line shows the *1/e* CCF level.

The calculated CCF in the interval $-20l_c < \Delta L < 20l_c$ is shown in figure 3.1., real part by blue solid line and imaginary part by green dotted line. Its real part is much broader than

turbulence Gaussian correlation function (red dashed curve) and asymmetric and possesses small, but finite imaginary part, shown by dotted line. The *1/e* CCF level is shown by horizontal dashed black line. As it is obvious, the CCF contains information on turbulence but does not provide direct information on the TCCF. Accordingly, the calculated CCF is very peaked about zero and shows slow logarithmic decay, unlike the initial Gaussian TCCF.

As soon as Fourier transform over signal CCF is performed we apply the extrapolation procedure to the signal CCF by exponential function in order to avoid fast oscillations of the resulting spectrum caused by delta-function. After extrapolation of the CCF to higher ΔL values and data processing according to (148) the real part of the reconstructed spectrum takes a form similar to the Gaussian (see figure 3.2.). The oscillations of the real part around the Gaussian spectrum are produced by discontinuities of the extrapolation procedure at $\Delta L = \pm 20 l_c$. A smaller imaginary part of the reconstructed spectrum is oscillating around the zero line. Smoothing of these oscillations results in a spectrum similar to Gaussian and possessing very small imaginary part, as it is shown in figure 3.2.

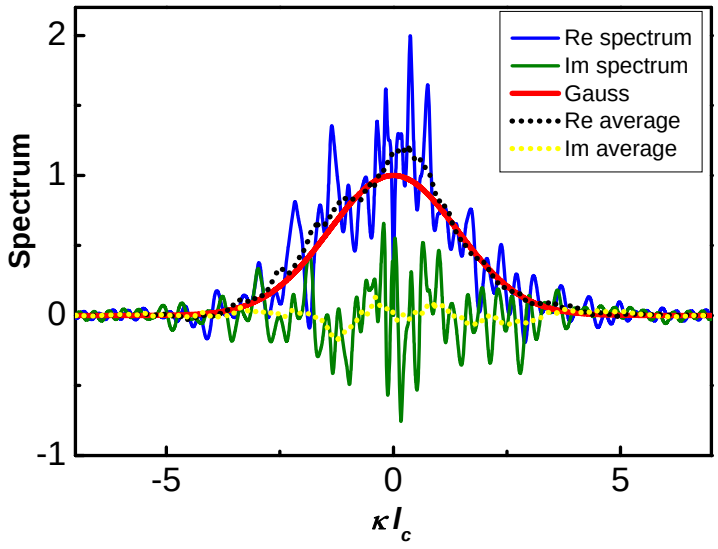

Figure 3.2. The computed spectrum versus normalized wave number. Reconstructed real (blue solid line) and imaginary (green solid line) parts, averaged curves by dotted black and yellow lines, input Gaussian spectrum by red solid line.

It is important to note that these oscillations originated from extrapolation procedure could be removed to the matching region $\Delta L = \pm 20 l_c$ by performing Fourier transform (152) of the reconstructed spectrum over a wave number interval $-2\omega_0/c < \kappa < 2\omega_0/c$, which corresponds to all the contribution of the Bragg scattering processes, in accordance with (59) providing the TCCF. The result of this transformation in the same case as in figure 3.2. is shown in figure 3.3.

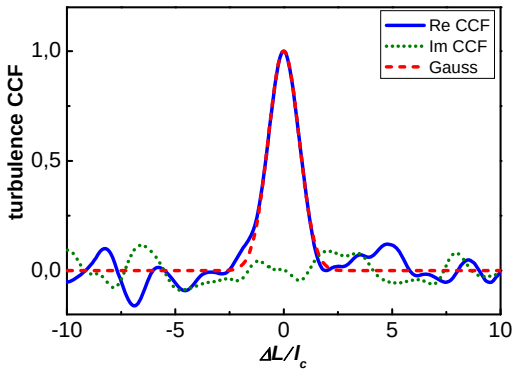

Figure 3.3. The TCCF (blue line) compared to Gaussian (red dashed line) given in relative units, N_s=500 in the same conditions as figure 3.1.

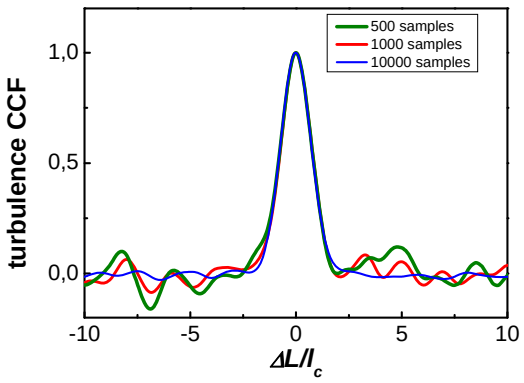

Figure 3.4. Comparison of the Gaussian TCCF (real part), N_s=500, N_s=1000 and N_s=10000, given in related units in the same conditions as figure 3.1.

As it is seen there, the reconstructed real part of the TCCF recovers the shape of initial Gaussian correlator at $|\Delta L| < 2l_c$. The finite value of the CCF imaginary part, as well as CCF random behavior at $|\Delta L| > 2l_c$ should be attributed to an imperfect averaging.

As it is seen in figure 3.4., the level of the oscillations of the reconstructed TCCF real part at $|\Delta L| > 2l_c$ is suppressed by increasing the averaging set from 500 to 1000 and further to 10000 samples (with reference to maximal sweeping step number, for example, on Tore Supra [128]).

3.2.1.1.2. Multi-component turbulence spectra

Using the approach based on equation (148) it is also possible to reconstruct more complicated, in particular, multi-component spectra.

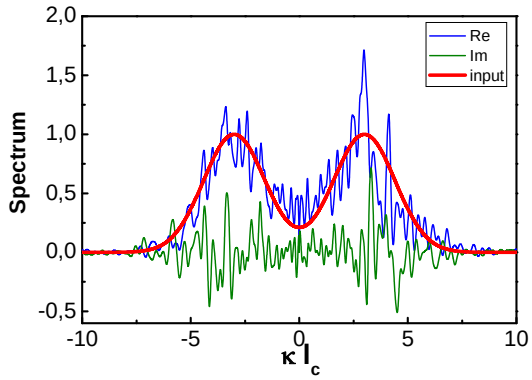

Figure 3.5.1.

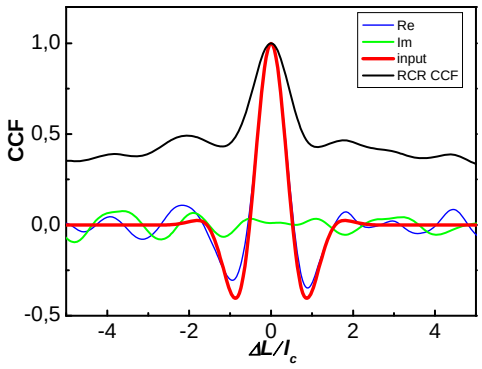

Figure 3.6.1.

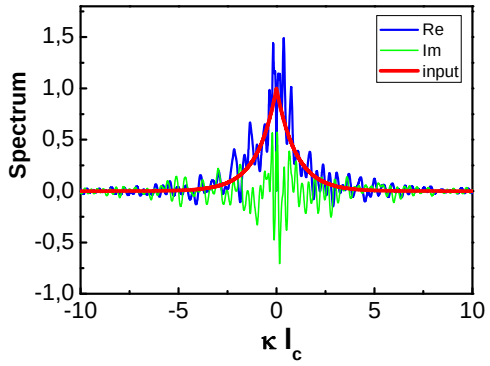

Figure 3.5.2.

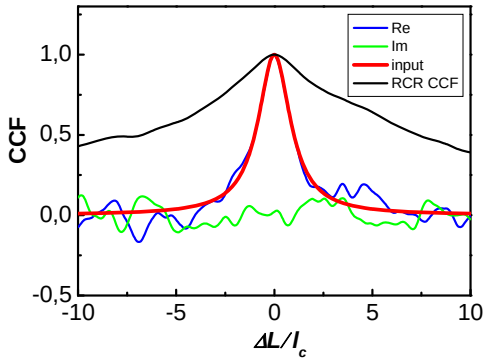

Figure 3.6.2

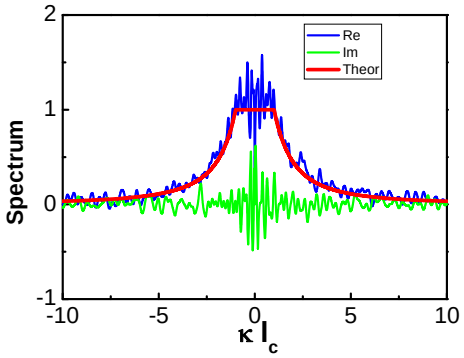

Figure 3.5.3.

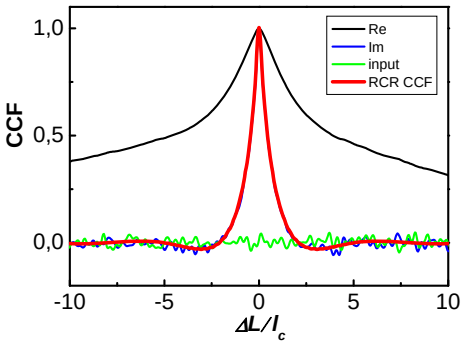

Figure 3.6.3.

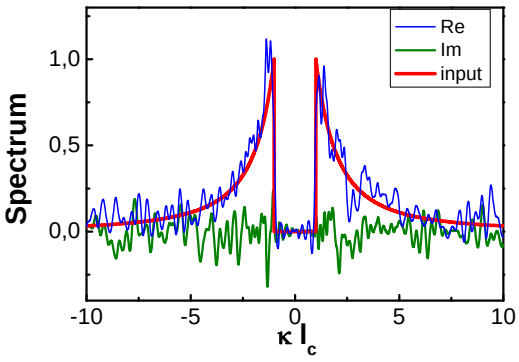

Figure 3.5.4.

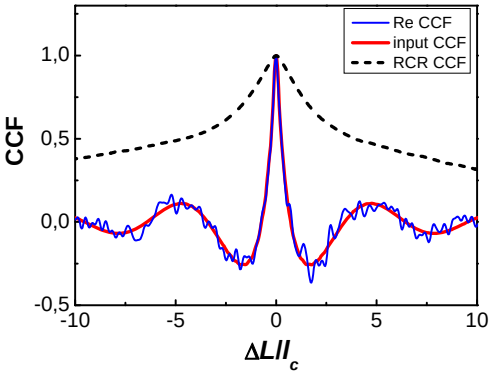

Figure 3.6.4.

Figure 3.5. Calculated spectrum versus normalized wave number. Reconstructed real and imaginary parts are presented by blue and green lines correspondingly, input spectrum by red line.

Figure 3.6. Signal CCF shown in relative units. Reconstructed real part is presented by blue line. Input TCCF is shown by red line, RCR CCF – by black line.

In figures 3.5.1. – 3.5.4. examples of several spectra are shown. The choice of these spectra corresponds to possible or encountered cases. The signal CCF for each spectrum has been compared to corresponding TCCF. The aim of these computations is to test capabilities of the

numerical method to reconstruct various types of spectra and to study the behavior of signal CCF and TCCF depending on distribution of spatial scales in spectra.

As we began with the Gaussian spectrum in section 3.2.1.1.1 we consider double-Gaussian spectrum shown in figure 3.5.1. This spectrum is notable for its decrease in the region $\left|\kappa l_c\right| < 3$ which cause sigh changes in the TCCF shown in figure 3.6.1.

As a more realistic example of spectrum we choose the exponential turbulence spectrum $\tilde{n}_\kappa^2 = 0.5 l_c e^{-|\kappa| l_c}$ shown in figure 3.5.2. observed in experiments [47, 129], with a flat part (figure 3.5.3.) and suppressed at small wave numbers $\left|\kappa l_c\right| < 1$ (figure 3.5.4.) reproducing discontinuity very well, in order to demonstrate the accuracy of very sharp spectral reconstruction. The signal CCF (dashed curve in figure 3.6) as in the example of previous section is also much broader than the input TCCF.

These spectra being treated in agreement with equation (148) (blue line real part in figures 3.5.1. – 3.5.4.) coincide with the input exponential spectrum (red line), imaginary part (green line) is oscillating around the zero line. Oscillations of the reconstructed real part of the spectrum around the initial one are produced by input signal CCF discontinuities in the extrapolation region and can be suppressed by increasing of number of sets of random phase samples as it was shown in section 3.2.1.1.1. The TCCF resulting from the spectrum Fourier transformation (blue line real part in figures 3.6.1. – 3.6.4.) fits the input one, as in case of Gaussian spectrum (see figure 3.3). The signal CCF shown in figure 3.6.4. possesses oscillatory behavior and changes sign due to spectrum suppression in the region $\left|\kappa l_c\right| < 1$ by analogy with signal CCF shown in figure 3.6.1.

Summarizing we underline that numerical computations presented in this paragraph distinctly demonstrate the capability of the proposed method to determine different kinds of radial wave number spectra even containing discontinuities and the associated CCF accurately. Moreover one could predict the turbulence wave number behavior and presenting spatial scales relying on the signal CCF and TCCF dependencies. Thus, if the TCCF real part is negative the prediction that the turbulence wave number spectrum is suppressed for small wave numbers could be made.

3.2.1.2. CCF and spectrum reconstruction in conditions relevant to experiment

The role played by simulations is essential for setting the experimental parameters. The numerical computations are required to determine the parameters in the frame of technical limitations according to validity domain and theoretical expectations. Thus, in this section we aim to precise the parameters at which the reconstruction of turbulence characteristics could be held successfully.

3.2.1.2.1. Determination of optimized realistic spatial probing interval

In the previous sub-section we have performed reconstruction based on the signal CCF computed in a very wide probing frequency range corresponding to $\Delta = 40 l_c$ never possible in experiments. Thus to hold numerical modeling in conditions relevant to experiment we reduce the probing interval in order to determine the conditions critical for reconstruction.

Figure 3.7. shows the reconstructed Gaussian TCCF for realistic cases $\Delta = 4 l_c$ (a) and (b). The computations are done for the parameters of large machine. It is clearly seen from figure 3.7. (b) that the probing interval $\Delta = 2 l_c$ is not sufficient to provide the correlation length within the error level of 25% in contrary to the interval $\Delta = 4 l_c$, figure 3.7. (a), where the error is less than 5%. Furthermore the shape of the TCCF can be determined from the figure 3.7. (a). Therefore we demonstrate numerically that the probing interval corresponding to technical possibilities which also allows turbulence characteristics reconstruction is $\Delta \geq 2 l_c$.

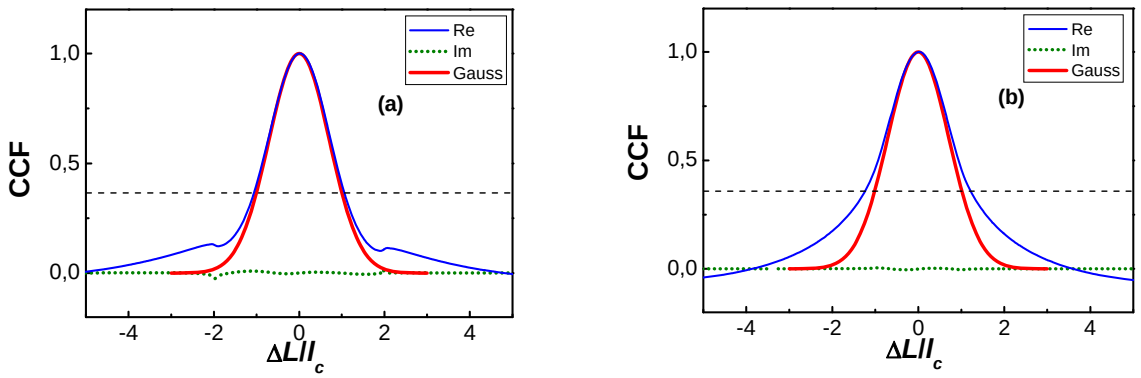

Figure. 3.7. The TCCF, $\Delta = 4 l_c$ (a) and $\Delta = 2 l_c$ (b). Input TCCF is shown by red line, reconstructed CCF by blue line (real part) and green line (imaginary part).

3.2.1.2.2. Realistic spatial probing step

The evaluation of the CCF used for the reconstruction in figure 3.1. was performed with fine spatial resolution within a wide region (1000 points within the $\Delta = 40 l_c$ interval), which corresponds to probing with a very detailed resolution and in a very wide range unrealizable in experiment. In more realistic conditions of only 16 RCR measurements the reconstruction of the TCCF is also feasible, as we show in figure 3.8. based on the RCR data obtained at $\Delta = 10 l_c$ ($-5 l_c < \Delta L < 5 l_c$) with the signal frequency cut-off step $\delta\Delta = 0.08 l_c$ and $\delta\Delta = 0.64 l_c$ (figure 3.9.). Comparing the result of TCCF reconstruction for the two cases it is possible to draw a conclusion that though the reconstruction for $\delta\Delta = 0.64 l_c$ possesses an oscillatory structure due

to spatial discretezation effect and discrepancy caused by extrapolation procedure, nevertheless it is still conceivable to determine the TCCF and correlation length therefore we consider the probing step $\delta\Delta = 0.64 l_c$ to be enough for reconstruction.

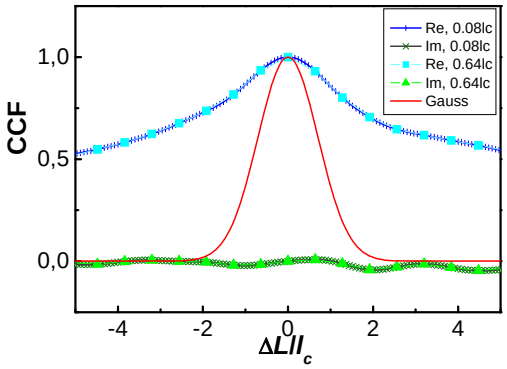

Figure 3.8. CCF shown in relative units for $\delta\Delta = 0.08 l_c$ (blue crosses real part and green crosses imaginary part) and $\delta\Delta = 0.64 l_c$ (cyan squares real part and green triangles imaginary part). Input TCCF is shown by red line.

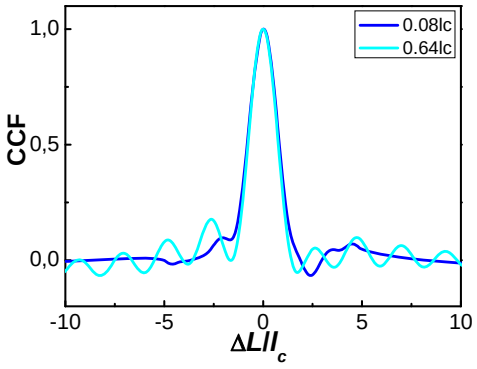

Figure 3.9. TCCF reconstructed at $\Delta = 10 l_c$, $\delta\Delta = 0.08 l_c$ (blue line) and $\delta\Delta = 0.64 l_c$ (cyan line).

3.2.1.2.3. Reconstruction in presence of uncorrelated noise

In this sub-section we study limitations of the reconstruction procedure associated with broadband noise. We model it as the white noise in the following way $A_{sN} = A_s + \eta A_s e^{i\varphi(\omega_j)}$ where A_{sN} is the measured signal, A_s is the scattering signal, η is the noise level, $\varphi(\omega_j)$ – random uncorrelated phase.

Here we represent the numerical simulation results obtained only for noise level of $\eta = 1.0$, whereas for the wide range of parameters (noise level $0.1 < \eta < 1.5$) the simulations were held as well. Figure 10 shows the CCF computed for Gaussian spectrum $\tilde{n}_\kappa^2 = \sqrt{\pi} l_c e^{-l_c^2 \kappa^2 / 4}$ in the case of $\eta = 1.0$ and N_s=*500* random phase samples by the solid line the real part and dotted line the imaginary part. The CCF oscillations could be reduced by increasing the number of sets of samples up to N_s=*10000* (see figure 3.10.). It could be seen that the maximum value of CCF is damped due to the presence of noise in comparison with figure 3.1.

In figure 3.12. we represent the turbulence radial wave number spectrum for N_s=*500*. The Gaussian spectrum kernel is observable there at $-5 < \kappa l_c < 5$ (shown by vertical dashed lines) however the noise level at wings is very high, not allowing the TCCF reconstruction (see huge oscillations in figure 3.13). We overcome the oscillations by decreasing the spectrum interval used for the Fourier transform. Thus, to obtain the TCCF shown in figure 3.14, we process the

spectrum from figure 3.12. in the interval $-5 < \kappa l_c < 5$. Therefore despite the high noise level there is still a possibility to select a spectrum interval for the Fourier transform which allows to decrease the oscillations in the TCCF. Meanwhile using the CCF computed for increased number of samples *Ns=10000* (see figure 3.11.) we are able to apply the Fourier transform directly to the interval $-20 < \kappa l_c < 20$ as presented in figure 3.15., though we should mention that this method is rather difficult to be realized in experiment.

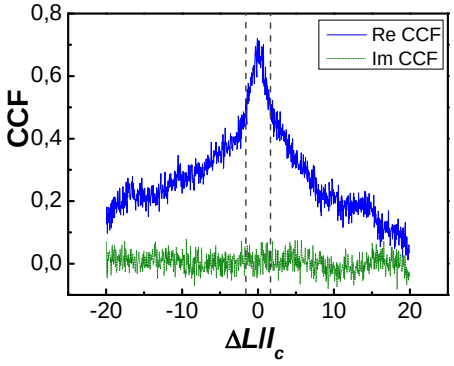

Figure 3.10. CCF at $\eta = 1.0$, Ns=500.

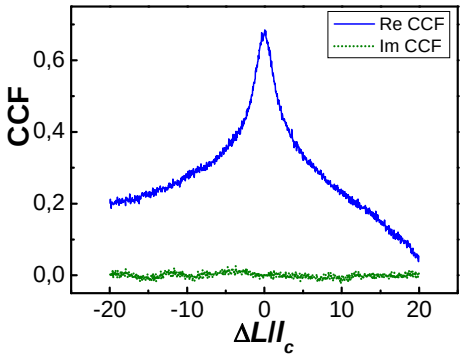

Figure 3.11. CCF at $\eta = 1.0$, Ns=10000.

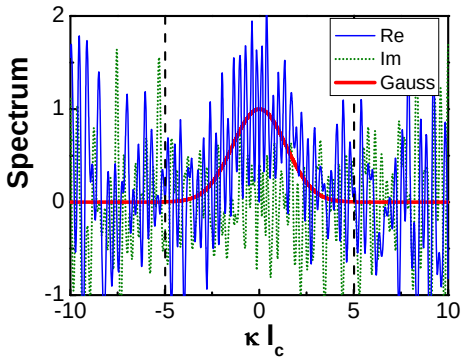

Figure 3.12. Spectrum at $\eta = 1.0$, Ns=500.

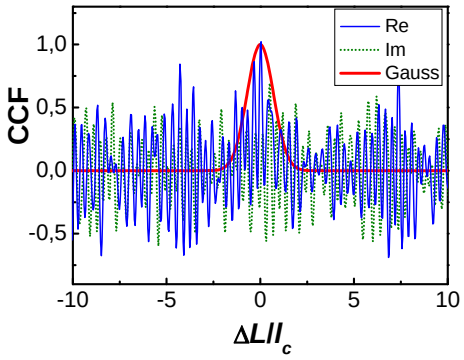

Figure 3.13. TCCF reconstruction at $\eta = 1.0$, Ns=500, spectrum interval $-20 < \kappa l_c < 20$.

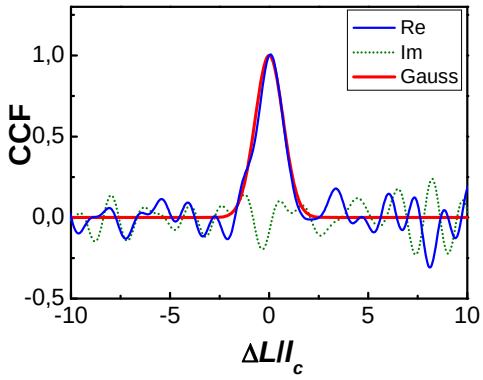

Figure 3.14. The TCCF reconstruction at $\eta = 1.0$, Ns=500, spectrum interval $-5 < \kappa l_c < 5$.

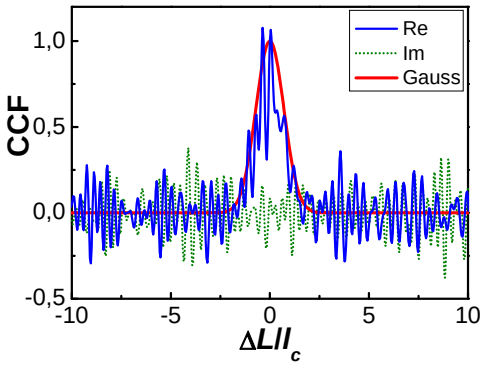

Figure 3.15. The TCCF reconstruction at $\eta = 1.0$, Ns=10000, spectrum interval $-20 < \kappa l_c < 20$.

3.2.1.2.4. Reconstruction in the condition close to experiment

Accounting for realistic experimental conditions we select from the CCF shown in figure 3.12. only 11 points in the probing range $\Delta = 3.2l_c$ ($-1.6l_c < \Delta L < 1.6l_c$) with resolution corresponding to $\delta\Delta = 0.32l_c$ (circles in figure 3.16. showing the points to be taken from the real part of the CCF) and extrapolate by exponential function further (blue squares) to the region $-20l_c < \Delta L < 20l_c$. The TCCF reconstructed from the CCF shown in figure 3.16. is shown in figure 3.17. in comparison to input Gaussian TCCF (red line). Therefore we underline that the proposed procedure gives proper correlation length and shape of TCCF even in very strict conditions.

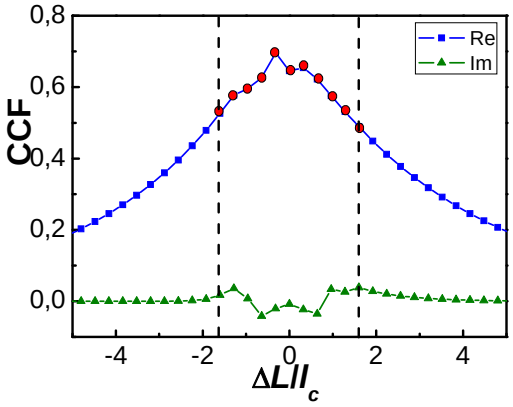

Figure 3.16. CCF cut at $\Delta = 3.2l_c$ and $\delta\Delta = 0.32l_c$.

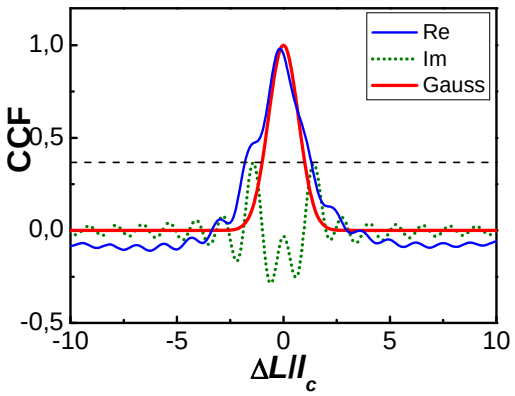

Figure 3.17. The TCCF reconstruction from CCF shown in figure 3.16.

3.2.2. Reconstruction of the turbulence spectrum and CCF for small machine

In this section we study the feasibility of the proposed wave number spectrum reconstruction procedure to explore quite different conditions when unlike previous cases the size of the probing region is comparable to the probing vacuum wavelength. This case corresponds to a study at the border of the validity domain and it is done to give a clearer idea on the possible application of the method on an existing experiment.

The probing frequency range is not wide enough in small machines, moreover the ratio of wave propagation region width to the vacuum wave length is small. For example at small research FT-2 tokamak it is given by $L_0 f_0 / c \approx 5.3$ where the reference frequency is f_0=40.1GHz and the reference frequency cut-off position is L_0=0.04m. Nevertheless, according to experimental results [40] a rather steep plasma density profile in FT-2 tokamak could be assumed linear that allows us to test the proposed reconstruction scheme in this tight geometry.

3.2.2.1. Standard conditions of reconstruction at FT-2

We make firstly computations using the following parameters: central plasma density $n_l=4.10^{19}\ m^{-3}$, probing frequency range for O-mode $21.1GHz < f < 52.7GHz$ which corresponds to probing interval $0.01m<L<0.07m$, Gaussian radial wave number spectrum $\tilde{n}_\kappa^2 = \sqrt{\pi} l_c e^{-l_c^2\kappa^2/4}$, correlation length $l_c = 0.02m$; number of sets of random phase samples $N_s=500$.

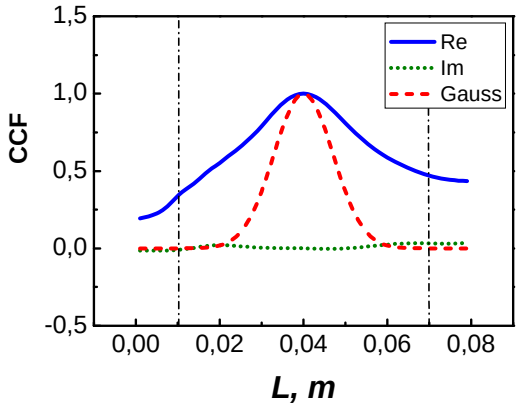

Figure 3.18. Signal CCF (blue line real part and green line imaginary part) and TCCF (red line) shown in relative units. Dashed-dotted vertical lines show the probing interval used for computation.

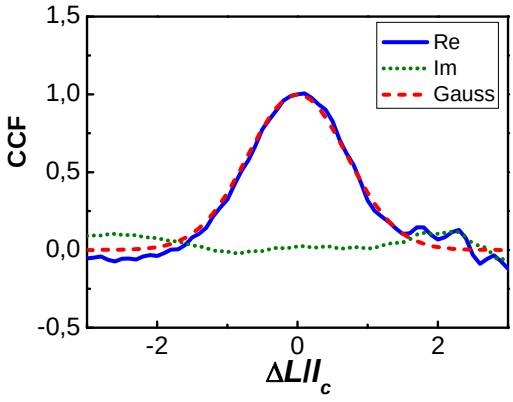

Figure 3.19. TCCF (real part by blue line and imaginary part by green line) compared to the input TCCF (red line) shown in relative units.

The RCR CCF computed in the corresponding interval $-1.5l_c < \Delta L < 1.5l_c$ (solid line in figure 3.18.) possesses slow decay as it has been proved above. Also it can be clearly seen that the kernel of the reconstructed TCCF fits well the input Gaussian TCCF (see figure 3.19).

3.2.2.2. Optimized reconstruction in more realistic conditions

Secondly we reduce the probing interval and change the calculation parameters as follows: reference frequency $f_0 = 31.7GHz$, reference cut-off position $L_0 = 0.05m$; probing frequency range for O-mode $24.5GHz < f < 37.5GHz$ which corresponds to probing interval $0.03m<L<0.07m$. The signal CCF computed in the interval $-l_c < \Delta L < l_c$ is shown in figure 3.20. by the blue line the real part and green line the imaginary part, red line shows the input Gaussian TCCF. As it was mentioned before that the behavior of the signal CCF and the initial TCCF is different. The TCCF is reconstructed rather precisely as it is shown in figure 3.21. in

spite of the fact the plasma size in FT-2 is only 10 wave lengths and the turbulence correlation length is only twice larger then it.

It is important to note that the probing range must be no less than $\Delta \approx 2l_c$ correlation lengths to obtain 10% error reconstruction on FT-2 tokamak. The discrepancy between the reconstructed TCCF and the input one could be explained as a consequence of small parameter $|\Delta L|/l_c = 1$. According to the framework of the proposed method it is applicable for higher densities (n_i=*8.0 10*^{19} *m*$^{-3}$) subject to utilizing higher frequencies up to 80GHz and probing range $\Delta \approx 8l_c$.

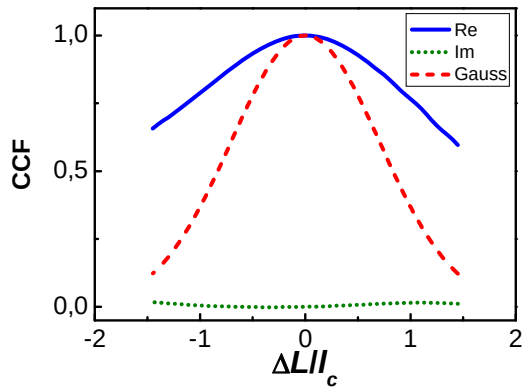

Figure 3.20. RCR CCF (real part by blue line and imaginary part by green line) compared to TCCF (red line).

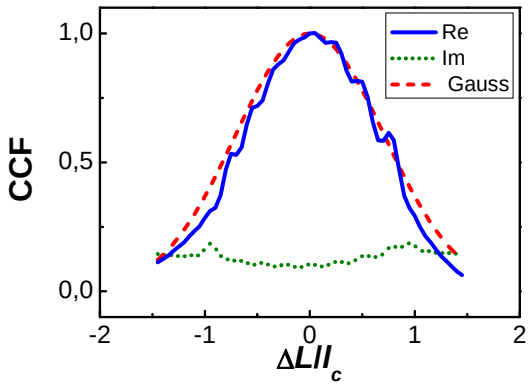

Figure 3.21. Reconstructed TCCF compared to the input Gaussian.

3.2.3. Amplitude CCF computation

In this section we present computations of the amplitude CCF (ACCF) held in case of linear plasma density profile according to formula:

$$\overline{ACCF}(\omega^j) = \frac{\left\langle \left(|A_s(\omega_0)| - \left\langle |A_s(\omega_0)| \right\rangle \right) \left(|A_s(\omega^j)| - \left\langle |A_s(\omega^j)| \right\rangle \right) \right\rangle_s}{\sqrt{\left\langle \left(|A_s(\omega_0)| - \left\langle |A_s(\omega_0)| \right\rangle \right)^2 \right\rangle_s \left\langle \left(|A_s(\omega^j)| - \left\langle |A_s(\omega^j)| \right\rangle \right)^2 \right\rangle_s}} \tag{180}$$

Computation parameters are the following: plasma size: *a=0.1 m,* reference cut-off: $L_0 = 0.09m$, reference frequency: $f_0 = 40GHz$, ($\omega_0 = 2.51 \cdot 10^{11} rad/s$, $\lambda_0 = 0.0075m$). The radial wave number spectrum is modeled as:

$$\delta n(\kappa) = \begin{cases} 1, & 0 \le |\kappa| \le \kappa_{\max} \\ 0, & \text{otherwise} \end{cases} \tag{181}$$

The correlation length is related to the spectral width via $l_c = 2.1/\kappa_{\max}$.

We consider several cases, the scan in the radial correlation length is $l_c / \lambda_0 \approx 0.4 - 2$, the computed ACCFs are shown in figure 3.22.1. – 3.22.4. 1D computations show that although the correlation length of the ACCF is significantly shorter than the correlation of reflectometry signals, the ACCF decay is slower than TCCF for all cases in linear regime. It is possible to draw a conclusion that the result of 1D computations differs from the result show in [130]. The measurement of radial correlation length can not be obtained from the amplitude signal in the linear regime.

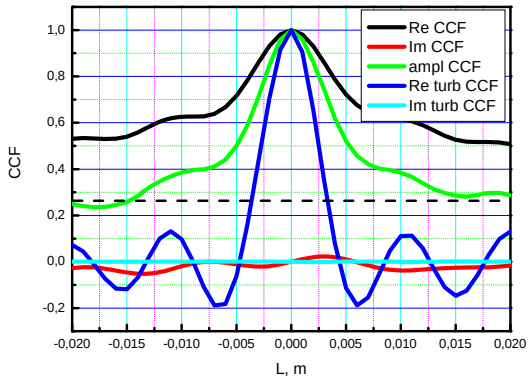

Figure 3.22.1. Signal CCF, ACCF and TCCF. $l_c / \lambda_0 \approx 0.4$, $l_c = 0.003m$, $\kappa_{\max} = 700m^{-1}$, $\alpha = 0.003m$

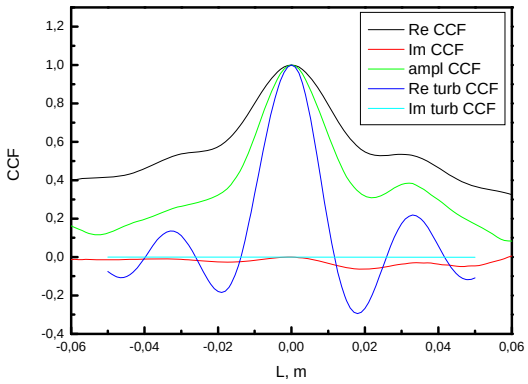

Figure 3.22.2. Signal CCF, ACCF and TCCF. $l_c / \lambda_0 \approx 1.2$, $l_c = 0.009m$, $\kappa_{\max} = 234m^{-1}$, $\alpha = 0.003m$

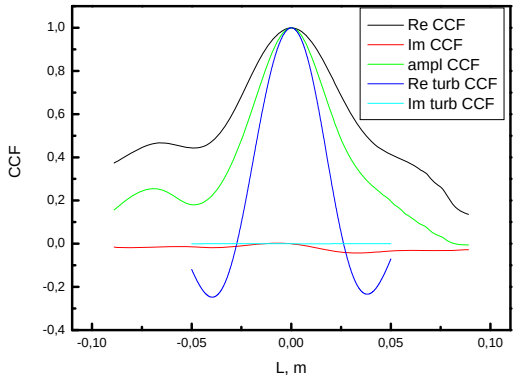

Figure 3.22.3. Signal CCF, ACCF and TCCF. $l_c / \lambda_0 \approx 2.5$, $l_c = 0.01875m$, $\kappa_{\max} = 112m^{-1}$, $\alpha = 0.003m$

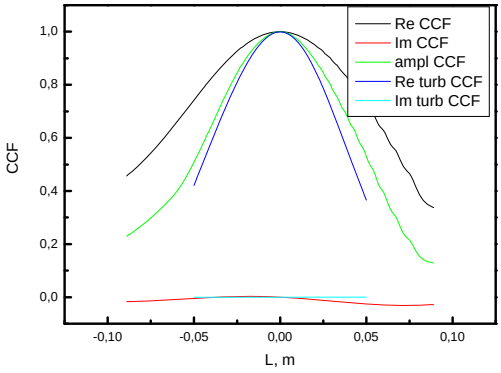

Figure 3.22.4. Signal CCF, ACCF and TCCF. $l_c / \lambda_0 \approx 6.67$, $l_c = 0.05m$, $\kappa_{\max} = 42m^{-1}$, $\alpha = 0.003m$

3.2.4. Inhomogeneous turbulence

In this section we consider inhomogeneous turbulence spectra and reconstruction of the turbulence suppression in internal transport barriers (ITBs). In order to show the possibility to detect transport barriers it is very important to perform the numerical modeling in case of

inhomogeneous spectrum. We model the ITB in the following way: the correlation length of Gaussian spectrum changes from $l_c = 0.01m$ at $0.37m < L < 0.43m$ to $l_c = 0.02m$ for other cut-offs.

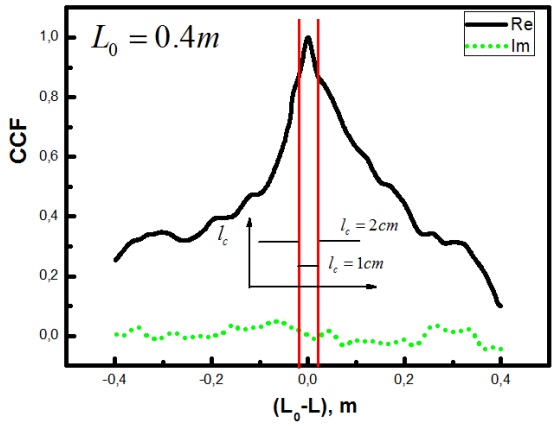

Figure 3.23. CCF, reference cut-off $L_0 = 0.4m$

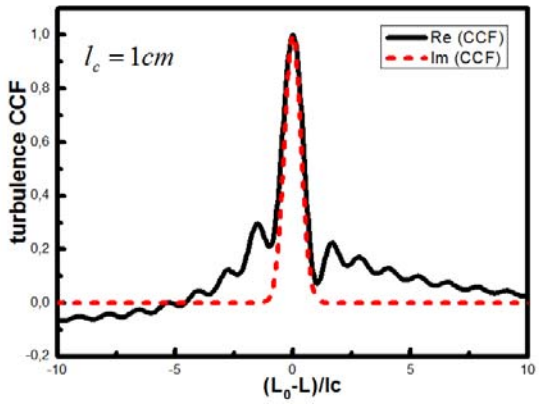

Figure 3.24. The TCCF reconstruction, $l_c = 0.01m$

Figure 3.23. presents the signal CCF, vertical red lines show the probing limits $0.37m < L < 0.43m$ which correspond to the boards of the ITB. The reconstructed TCCF is shown in figure 3.24. by black curve possesses the correlation length $l_c = 0.01m$. Therefore we show the locality of the method able to reconstruct local parameters of turbulence inside the ITB.

Probing limits shown by red lines in figure 3.25. are $0.2m < L < 0.8m$ for the reference frequency cut-off position $L_0 = 0.5m$. The shaded area shows the zone where the turbulence spectrum changes. It is worth to underline that the obtained result (figure 3.26) in the presence of inhomogeneity fits the initial TCCF (shown by red line). Thus we demonstrate high local sensitivity of the method to turbulence properties outside the barrier. The quality of local parameter reconstruction is not affected by presence of ITB inside the probing zone.

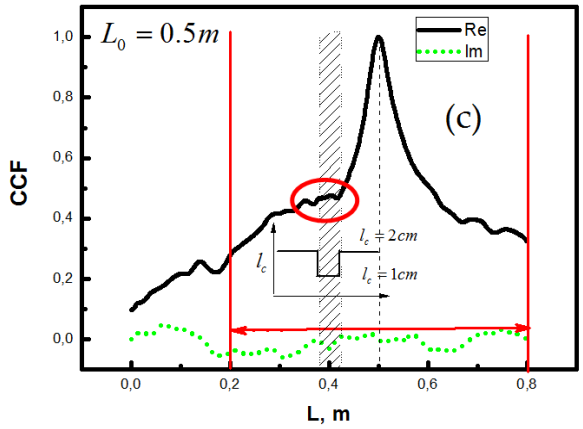

Figure 3.25. CCF, reference cut-off $L_0 = 0.5m$

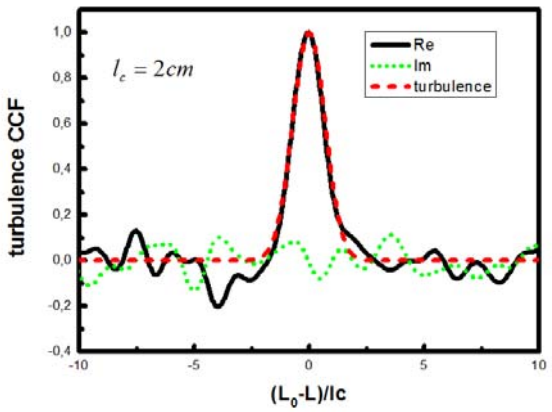

Figure 3.26. The TCCF reconstruction, $l_c = 0.02m$

3.3. O-mode probing in case of density profile close to experimental one

This section is a first transition step from theory and simple numerical simulations to realistic experiments. Thus, we perform numerical simulations for O-mode probing by the example of Tore Supra-like smooth plasma density profile as well as ITER-like plasma density profile with a steep gradient zone.

3.3.1. Tore Supra – like plasma density profile

A synthetic density profile according to experimental data [121] has been generated using four parameters and can be written as following:

$$n(x) = n_c \cdot 0.5\left(1 + th\left(\alpha\left(x - x_a\right)\right)\right) \cdot \left(1 - \frac{\left(x - x_b\right)^2}{a^2}\right) \tag{182}$$

where $\alpha = 80m^{-1},\ x_a = 0.05m,\ x_b = 0.8m,\ a = \frac{\sqrt{3}}{2}m,\ n_c = 3.9 \cdot 10^{13} cm^{-3}$ (see figure 3.27.).

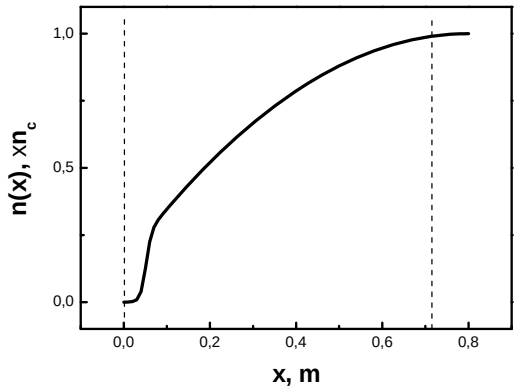

Figure 3.27. Density profile for Tore Supra as a function of radial position. Dashed lines show the computation probing interval.

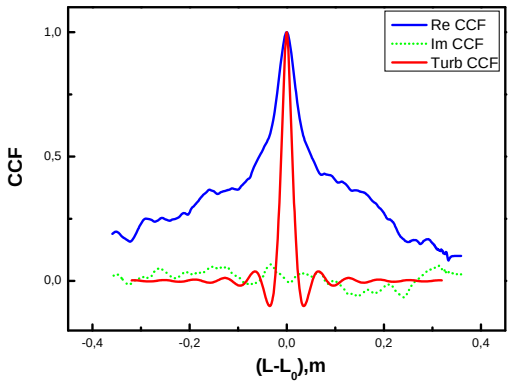

Figure 3.28. The RCR CCF (real part by blue line and imaginary part by green line) compared to the TCCF (red line) shown in relative units.

Modeling is performed within the O-mode reflectometer bandwidth $30GHz < f < 60GHz$, which corresponds to rather wide probing interval *0.075m<L<0.719m* shown by vertical dashed lines in figure 3.27.; reference frequency: $f_0 = 47GHz$; reference frequency cut-off position $L_0 = 0.36m$. Averaging is performed over ensemble of N_s=*500* random phase samples. The turbulence spectrum used in the analysis given by [47]:

$$\delta n_{\kappa}^{2} = \begin{cases} 1, |\kappa| < 1cm^{-1} \\ \kappa^{-3}, 1cm^{-1} < |\kappa| < 6cm^{-1} \\ \kappa^{-6}, |\kappa| > 6cm^{-1} \end{cases} \quad (183)$$

is shown in figure 3.29. by red line.

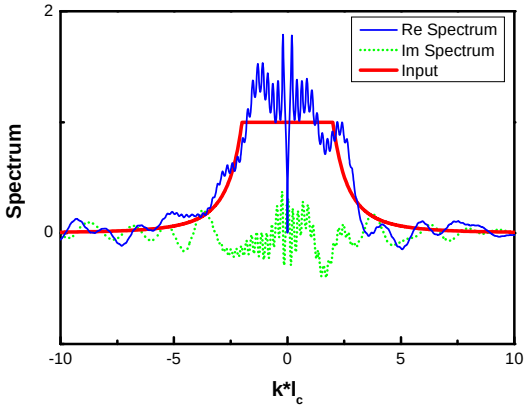

Figure 3.29. Calculated spectrum versus normalized wave number. Reconstructed real part (blue), imaginary part (green) and input spectrum (red).

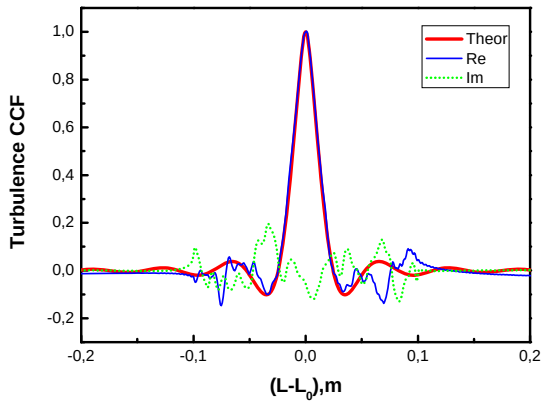

Figure 3.30. TCCF (real part by blue and imaginary part by green) compared to input TCCF (red) shown in relative units.

In figure 3.28. we present the numerically calculated signal CCF (blue line real part) compared to the TCCF (red line). The reconstructed turbulence wave number spectrum (blue line real part) compared to the input one (red line) is shown in figure 3.29. The same comparison is shown in figure 3.30. for the reconstructed TCCF (blue real part). It is clearly seen from these figures that though the inverse relation was derived from equations for linear plasma density profile it is applicable at more complicated monotonic smooth plasma density profile and provides the width of the spectrum, its shape and correlation length from computations.

3.3.2. Plasma density profile with a steep gradient

We model a synthetic plasma density profile shown in figure 3.31. close to JET profile and baseline scenario profile at ITER machine (see figure 3.32.) by introducing the following parameters to the expression (182): $\alpha = 100m^{-1}$, $x_a = 0.045m$, $x_b = 0.8m$, $a^2 = 2.55m^2$.

Calculations have been performed in two principal cases. Firstly we simulate probing in the interval *0.01m<L<0.128m,* at reference frequency $f_0 = 73.3GHz$. Plasma density profile is no more linear however we apply the reconstruction procedure derived in case of linear density

profile (148). Therefore we suppose that locally plasma density profile is linear and substitute the reference cut-off position with local gradient scale $L_0 = 0.069m$. Input radial wave number spectrum is shown in figure 3.29. by red line and is similar to that one used in previous subsection. Probing interval covers steep gradient zone as well as transition zone to the smooth profile. Changing of gradient complicates the reconstruction due to the diagnostic is local and provides information on turbulence properties at the position of reference cut-off. Reconstructed TCCF compared to the input one is shown in figure 3.33. Due to strong plasma density profile asymmetry we obtain some discrepancy between these two functions, nevertheless it can be asserted that the TCCF is reconstructed qualitatively.

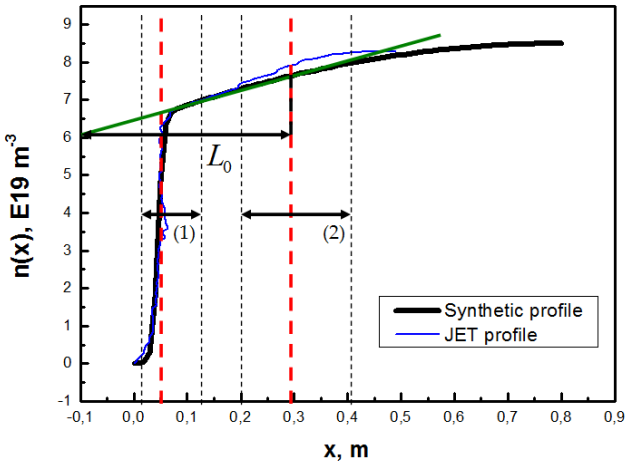

Figure 3.31. Plasma density profile, dashed lines show the cut-off positions $L_0 = 0.069m$ (1) and $L_0 = 0.3m$ (2), dash-dotted lines show the corresponding probing range boundaries.

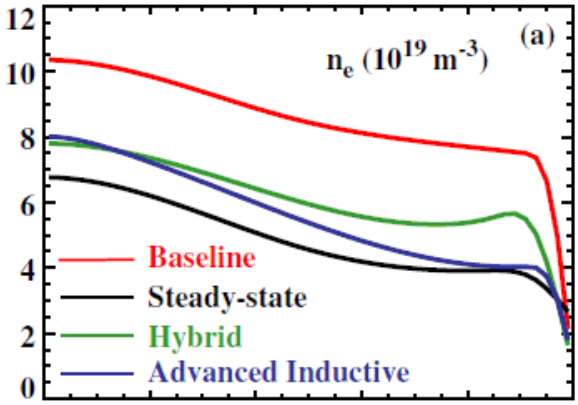

Figure 3.32. Profiles as a function of normalized radius for electron density, for baseline (131498, in red), steady-state (131198, in black), hybrid (131711, in green) and AI (133137, in blue) scenario plasmas. Taken from [131].

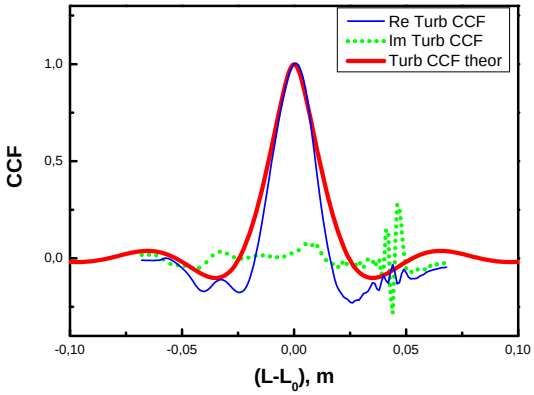

Figure 3.33. TCCF, $L_0 = 0.069m$, $\Delta = 0.118m$.

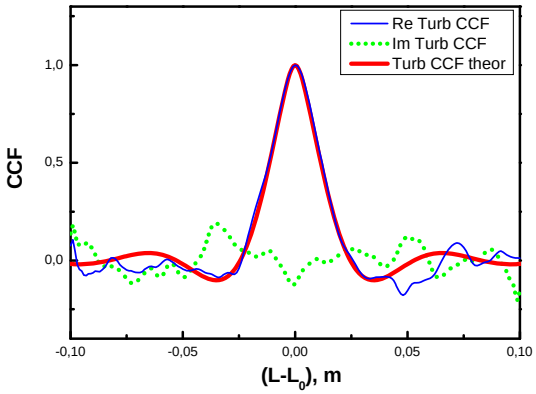

Figure 3.34. TCCF, $L_0 = 0.3m$, $\Delta = 0.2m$.

Secondly we model the probing held within the spatial interval 0.2m<L<0.4m covering smooth plasma density profile, reference frequency is $f_0 = 78.6GHz$ corresponding to the local gradient scale $L_0 = 0.3m$, the reconstructed TCCF (blue) coinciding to the input one (red) is shown in figure 3.32.

Computations discussed in this subsection prove the applicability of the method in case of probing in the steep gradient zone of plasma. This result offers opportunities of measuring plasma properties in pedestal of ITER and JET huge machines.

3.4. Synthetic X-mode RCR experiment

Till now we have considered wave propagation in O-mode. Usually in experiments X-mode wave is used to reach the high field side of the torus. In order to test the reconstruction of plasma turbulence properties in real experiment, simulations were undertaken in conditions of shot #47669 performed in June 2011 at Tore Supra machine. Experimental plasma density profile and magnetic field profile are shown in figures 3.35 and 3.36 correspondingly.

These simulations are focused on studying the quality of reconstruction in Tore Supra experiment in idealistic conditions not taking into account MHD activity in the center of plasma and considering only the impact of homogeneous turbulence to the signal RCR CCF.

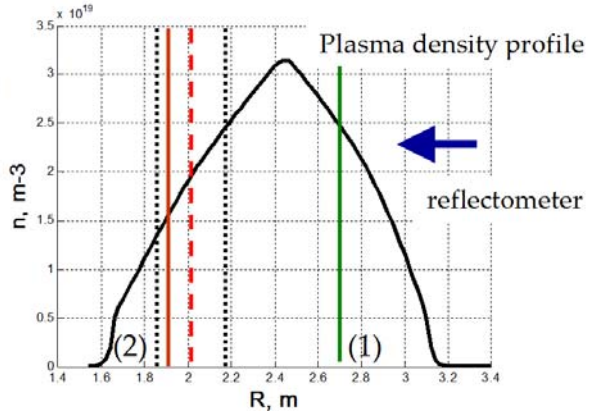

Figure 3.35. Plasma density profile, shot #47669, t=9.55s, Tore Supra.

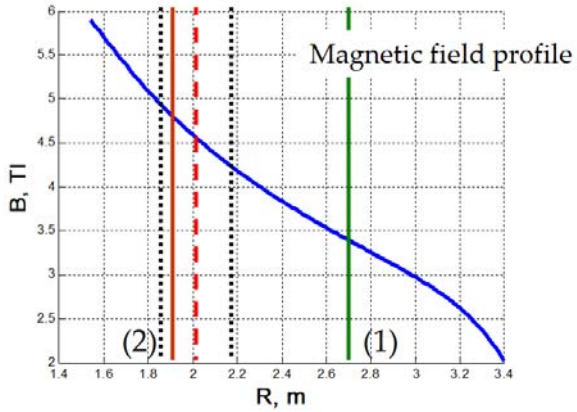

Figure 3.36. Magnetic field profile, shot #47669, t=9.55s, Tore Supra.

Probing frequency range was chosen according to the settings of the D-band (110-150 GHz) X-mode reflectometer installed at the low field side of Tore Supra tokamak $135GHz < f < 145GHz$ corresponding to the probing interval 1.85m<x<2.15m shown in figures 3.35. and 3.36. by vertical dotted black lines. Reference frequency $f_0 = 140GHz$ corresponds to reference cut-off position R_0= 0.85m shown in figures 3.35. and 3.36. by vertical dashed red line. The number of frequencies is N_ω=110 that corresponds to spatial probing step and frequency

step $\delta\Delta = 3mm$ of the order $\delta f = 97MHz$. The statistical averaging was held over N_s=500 random samples. The input turbulence spectrum is specified as [134]:

$$\delta n_\kappa^2 = \begin{cases} 1, & |\kappa| < 1cm^{-1} \\ \dfrac{\kappa^{-3}}{\left(1+\kappa^2\right)^2}, & |\kappa| \geq 1cm^{-1} \end{cases} \qquad (184)$$

shown in figure 3.38 by red line. The number of wave number modes N_κ=10000 is specified within the wave number interval $|\kappa| < 10cm^{-1}$.

We compute RCR CCF numerically for these parameters in Born approximation according to procedure described in subsections 3.1.1-3.1.3. Further we apply to this simulated RCR CCF the spectrum reconstruction procedure (148).

In figure 3.37. we show the X-mode refractive index dependency on the radial position. In both cases of the cut-off position before (1) and behind (2) the density peak the refractive index can be assumed to be close to linear as soon as we suppose that plasma density profile is close to linear in the vicinity of the reference cut-off position. Taking this into account we use formula (148) derived in case of O-mode probing of linear profile to realistic experimental case and check the capability of this procedure numerically.

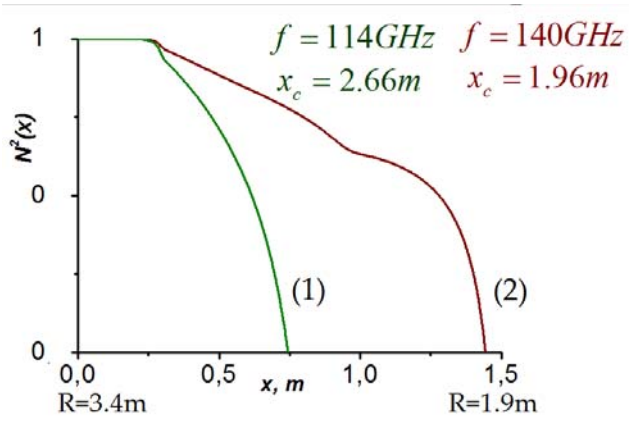

Figure 3.37. Refractive index of the probing X-mode wave for cut-off positions (1) $x_c = 2.66m$ and (2) $x_c = 1.96m$.

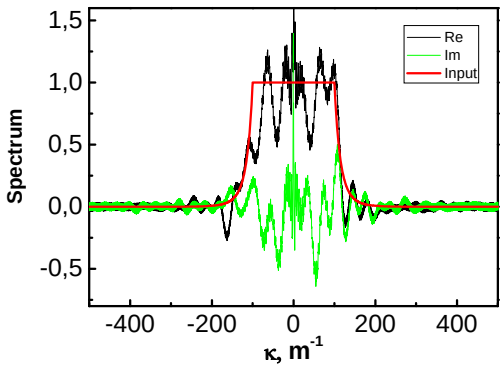

Figure 3.38. Turbulence spectrum reconstruction compared to the input one. Black lines show the interval taken for Fourier transform.

In figure 3.38. the reconstructed turbulence spectrum (blue real part) in comparison to the input spectrum (red line) is shown, the complicated $\sim\kappa^{-7}$ dependency is followed by the reconstructed spectrum however the flat part of the spectrum is not reconstructed perfectly. The error level is estimated by imaginary part oscillations and reaches 30% level that could be explained by discontinitues produces by extrapolation procedure and discontinitues in wave number spectrum.

In figure 3.39 we show RCR CCF (blue line) which as in O-mode probing case possesses slow logarithmical decay comparing to the input TCCF (red line). The reconstructed TCCF comparing to the inpur one is shown in figure 3.40. by black (real part) and green (imaginary part) lines.

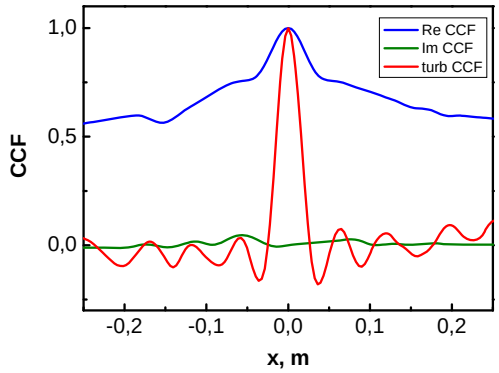

Figure 3.39. RCR CCF (blue line real part, green line imaginary part) and input TCCF.

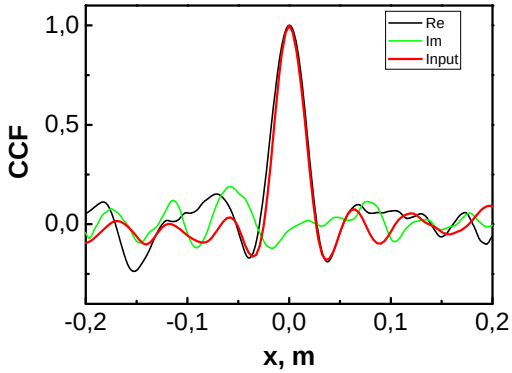

Figure 3.40. Reconstructed TCCF (black line real part and green line imaginary part) and input TCCF (red line).

3.5. Summary

Concluding we would like to stress that application of the proposed procedure to the turbulence spectrum and CCF reconstruction from RCR data have led to very promising results. Numerical modeling in conditions relevant to experiment in case of few averaging random phase samples, small probing range and high white noise level recovers the input parameters. The demonstrated possibility of fine reconstruction, at least in 1D geometry, is proving the procedure feasibility and appealing for further optimization and tests in 2D numerical modeling.

Basing on results of this Chapter we have determined the following parameters for reconstruction required in experiments: number of probing frequencies N_ω=80..150, probing step $\delta\Delta = 1..5mm$ and probing frequency step $\delta f = 50..150MHz$.

It is also necessary to mention that the spectrum reconstruction procedure developed for O-mode linear plasma density profile needs to be improved to be applied for X-mode arbitrary profile case to decrease inaccuracy of reconstruction.

Chapter IV

Applications to experiments

Previous Chapters of this thesis covered theoretical background of RCR applications and numerical modeling of experiments which are certainly convincing however experimental approbation of the method is also required. How to move from the theory and simulations to the real world? Passing from theoretical models to real experiments we face plenty of additional tasks and problems: hardware volatility, additional noise, shot conditions, technical problems of data acquisition and huge volumes of data to be processed…

Since there were no RCR experiments applying the new method of radial wave number spectrum reconstruction undertaken before results described in this section are preliminary and are focused on estimation of experimental parameters and settings. Besides that the more ambitious task was to estimate and compare turbulence parameters such as correlation length, radial wave number spectrum and turbulence spatial CCF in small and large machines and give an insight into capabilities of RCR diagnostic. We would like to notice as well that there is no universal method applicable to all machines; different hardware and different plasmas demand unique approach and it is needed to develop specific software and data interpretation methods for each experiment.

This part of the thesis is devoted to three separate methods of data processing obtained at three different machines – FT-2, Tore Supra and JET. Furthermore experimental results using the proposed method of turbulence properties determination are discussed.

4.1. General remarks on data analysis

Although the RCR systems installed at Tore Supra, FT-2 and JET machines are different in terms of possibilities, constraints and specifications due to the specificity of each device. However the reflectometer principal scheme is similar and the reflectometry signal acquisition is realized in the same way as well as statistical analysis. The former numerical computations specify general experimental parameters such as probing interval, step and statistics depending on experimental conditions. In this section we summarize these findings and determine necessary parameters for data analysis.

4.1.1. Reflectometer generic scheme

Firstly we precise a simplest synthetic circuit of heterodyne reflectometer in figure 4.1. Refectometers consist of a microwave source, transmission lines and a detection system. The microwave source is typically a solid state oscillator with a frequency range dependent on the applied voltage and semiconductor structure. Transmission lines are generally low-loss oversized waveguides since the microwave source and detection system are usually located at a great distance from the plasma.

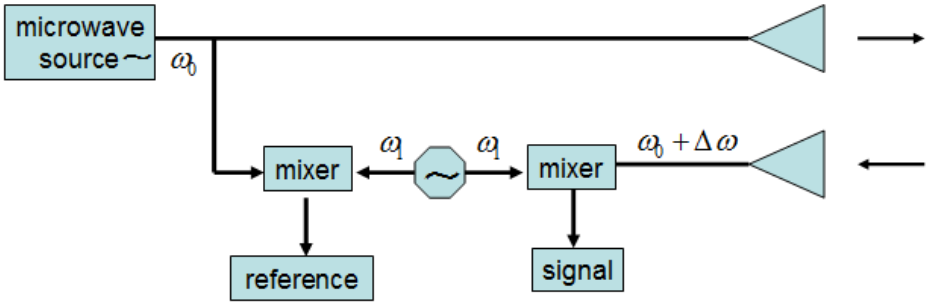

Figure 4.1. Circuit diagram of one channel of a heterodyne reflectometer.

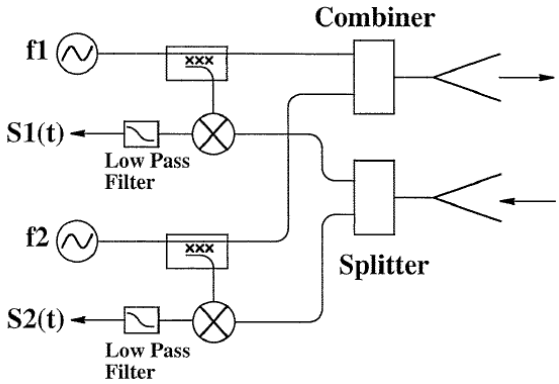

Figure 4.2. Simplified radial correlation reflectometer circuit diagram. Taken from [132].

In this Chapter three different reflectometer systems will be discussed further for Tore Supra, FT-2 and JET tokamaks. Typical scheme of two-channel correlation reflectometer is shown in figure 4.2

4.1.2. Quadrature phase detection

The hardware used in this thesis exploits heterodyne detection which is applied for amplitude and phase fluctuations detecting. For full information on the spectral characteristics of the received signals, quadrature detection is required. The reference and received signals enter a so called IQ detector. In figure 4.3 the circuit diagram of an IQ detector is shown.

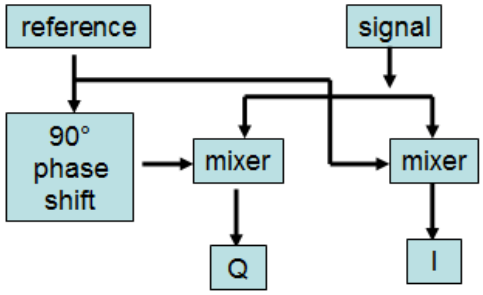

Figure 4.3. Circuit diagram of an IQ detector.

The signal received is obtained as the complex amplitude signal. It is mixed with the reference signal and the two components are obtained: in-phase (I) component and 90° – quadrature (Q) component:

$$A_s(f,t) = I(f,t) + iQ(f,t) = A_0(f,t)\cos\Phi(f,t) + iA_0(f,t)\sin\Phi(f,t) = A_0(f,t)e^{i\Phi(f,t)} \quad (185)$$

where f is a probing frequency, t is a moment of time.

$$I(f,t) = A_0(f,t)\cos\Phi(f,t) \quad (186)$$

$$Q(f,t) = A_0(f,t)\sin\Phi(f,t) \quad (187)$$

The amplitude and phase are obtained from the signal:

$$A_0 = \sqrt{A_s A_s^*} = \sqrt{I^2 + Q^2} \quad (188)$$

$$\Phi = \pm\arctan\frac{Q}{I} \quad (189)$$

Since the phase is changing in time the angular velocity is given as:

$$\omega = \frac{d\Phi(f,t)}{dt} \quad (190)$$

The received signal is complex therefore both the positive and negative frequencies are resolved and the fluctuation spectra are two-sided. In this work the IQ-detection is used.

4.1.3. Probing range and step

In general the RCR experiment is realized as following: the reference frequency is fixed, it determines the reference cut-off position at which the turbulence parameters are defined. The probing frequency is swept within the specified frequency range. It is important to choose the probing frequency step which in its turn predetermines probing spatial steps. Here we would like to underline that equidistant spatial step is required due to subsequent FFT applied to the measured signal RCR CCF. Moreover the probing step should be less than half correlation length. In addition as it was pointed out in Chapter III for satisfactory reconstruction the minimum probing range is limited by $\Delta \approx 4 l_c$ therefore its is needed to estimate the correlation length in advance.

4.1.4. Statistical analysis

In figure 4.4. the example of experiment realization is shown. Within a window the set of steps is realized by the sweeping channel, the number of steps N_ω (is equal to number of probing frequencies). The time acquisition rate provides the upper frequency seen and the time step the lowest one. The reference channel is synchronized to the sweeping channel. Plateau duration $t_{plateau}$ and time step t_{step} determine the number of steps within a plateau:

$$N_{plateau} = \frac{t_{plateau}}{t_{step}} \tag{191}$$

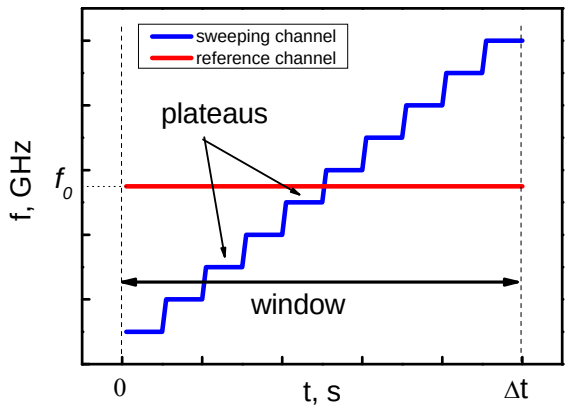

Figure 4.4. Probing frequency evolution in a time window during RCR experiment.

The received signal is discrete and depends on time point $A_s(f, t_i)$ where t_i is the moment of time. The total number of points in a window is determined by number of frequencies and number of points per plateau:

$$N_{window} = N_{plateau} \cdot N_{\omega} \tag{192}$$

To analyze turbulence frequencies presenting in a signal we should transform the signal using FFT into turbulence frequency space. It is evident that the number of points in plateau is formed by number of samples of averaging N_s and number of turbulence frequencies N_Ω:

$$N_{plateau} = N_s \cdot N_\Omega \tag{193}$$

The summation is carried out over N_s, this determines statistical averaging. The resolution in turbulence frequency space is given by N_Ω. The number of points in a plateau is determined by technical settings of experiment however it is limited by plasma conditions. When probing we assume that the plasma is "frozen". Thus, the total window duration should be less than plasma correlation time. Therefore, the total number of points in a window is limited and we should balance between increasing N_s, N_Ω or N_ω:

$$N_{window} = N_s \cdot N_\Omega \cdot N_\omega \tag{194}$$

In other words, N_ω is dictated by probing range and step limits, N_Ω should correspond the required turbulence frequency resolution, N_s should be enough for satisfactory statistical averaging. Finally, having fixed the parameters, we obtain the signal RCR CCF depending on probing frequency (or cut-off) difference Δf for each turbulence frequency Ω separately.

All these parameters are determined individually for each reflectometry system.

4.2. Results of RCR experiment at Tore Supra

Experiments on Tore Supra were the first attempt to apply the theoretical method of turbulence properties determination at real machine.

Tore Supra machine was described in section 1.3.1.1. In this section we discuss experimental results obtained during the campaigns on the 24th of November 2010 and on the 23rd of June 2011. The aim of experiments is to determine plasma turbulence characteristics using the fast-sweeping correlation reflectometer installed on Tore Supra.

4.2.1. Reflectometers at Tore Supra

A list of the reflectometer systems installed at Tore Supra is given in table 4.1. For more detailed information the reader is referred to [34].

Table 4.1. List of reflectometers installed at Tore Supra

Reflectometer type	Year	Probing range
O-mode	1995 [121]	26-36 GHz

X-mode (V-band)	2003 [121] 2009 (upgrade)	52-78 GHz
O-mode (V-band) Doppler setup	2004 [121]	50-75 GHz
X-mode (E-band)	2011 [133]	60-90 GHz
X-mode (W-band)	2003 [128] 2009 (upgrade)	74-109 GHz
X-mode (D-band) fast-sweeping	2010 (upgrade) [121]	110-150 GHz

Tore Supra is equipped with profile reflectometers covering V and W bands, a fluctuation one on the D band and a Doppler setup using the V band [128]. All the Tore-Supra reflectometers have the similar design based on a heterodyne detection achieved thanks to a Single Sideband Modulator (SSBM). The scheme of V and W band fast-sweep reflectometers is shown in figure 4.6 [121].

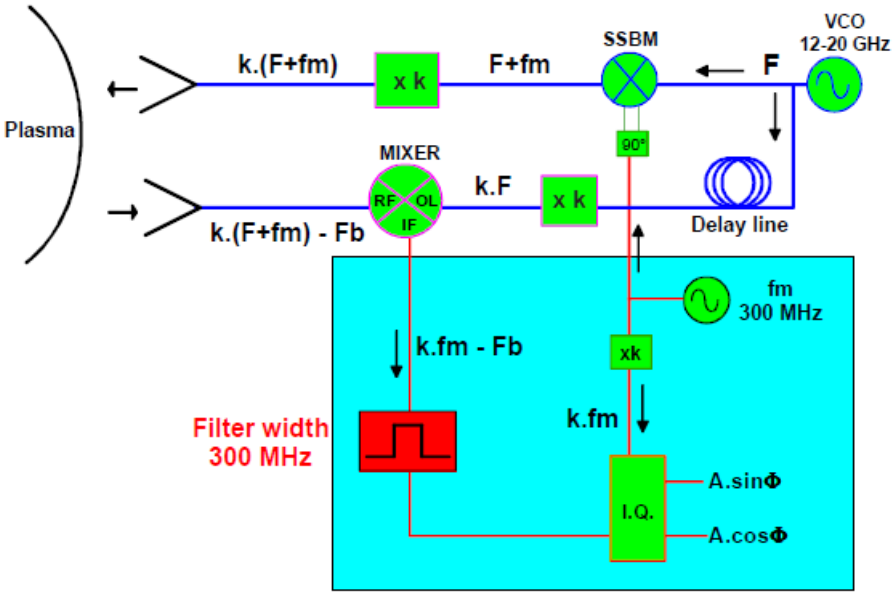

Figure 4.6. Schematic of the reflectometers, V and W bands. Taken from [121].

Measurements discussed in this section were made using D-band upgrade fast sweeping reflectometer. This reflectometer was primary designed to study density fluctuations by doing steps of fixed probe frequencies. Thanks to a fast switch, the D-band reflectometer can now perform during the same shot frequency steps and fast sweeps [135].

4.2.2. Phase calibration

The waveguide dispersion and the vacuum propagation is removed using a wall reflection signal which is acquired before each shot. The calibration phase Φ_{cal} is extracted by unwrapping the angle of the complex signal. Phase in vacuum for reference and sweeping frequencies:

$$\Phi = 2(L_3 - L_1)\,\omega/c \tag{195}$$

where $L_1 = 1.54m$ the inner wall coordinate, $L_2 = 3.2m$ plasma boundary, $L_3 = 4.4m$ the position of the receiver. The phase collected in waveguides is computed as:

$$\Phi_{wg} = \Phi_{cal} - \Phi \tag{196}$$

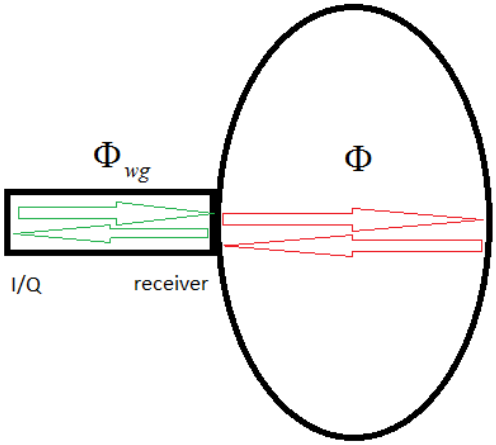

Figure 4.7. Phase in waveguides and inside the vacuum vessel without plasma.

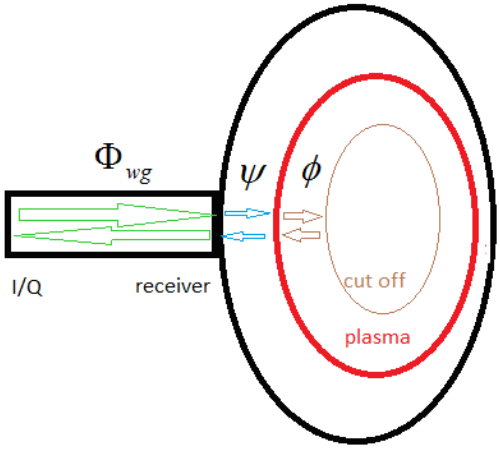

Figure 4.8. Phase in waveguides, vacuum and plasma.

In plasma, the phases of X-mode are given by:

$$\phi = 2\int_{L_2}^{x_c} \sqrt{\varepsilon_1}\,\frac{\omega}{c}\,dx \tag{197}$$

where x_c is the cut-off position and the permittivity is given by

$$\varepsilon = \left[1 - \frac{\omega_p^2}{\omega^2}\frac{(\omega^2 - \omega_p^2)}{(\omega^2 - \omega_p^2 - \omega_c^2)}\right] \tag{198}$$

Phase of the propagation in vacuum between plasma and receiver:

$$\psi = 2(L_3 - L_2)\,\omega/c \tag{199}$$

The total phase contains the part collected in the waveguides, the part in vacuum and the part obtained due to propagation in plasma:

$$\Phi_{total} = \Phi_{wg} + \psi + \phi + \delta\tilde{\Phi} \tag{200}$$

where $\delta\tilde{\Phi}$ is a fluctuating phase. As we analyze the fluctuating phase the rest terms should be removed by multiplying the weighting function $e^{-i[\Phi_{wg}+\psi+\phi]}$.

Finally the correlation function is computed according to the phase correction:

$$CCF(\Delta L) = \left\langle A_s(\omega_0)A_s^*(\omega)\right\rangle e^{-i[(\phi_0+\psi_0-\phi-\psi)+((\Phi_{cal\,0}-\Phi_0)-(\Phi_{cal}-\Phi))]} \tag{201}$$

where index *"0"* corresponds to the reference frequency.

4.2.3. Data analysis and interpretation

In this section we describe several RCR measurements held at Tore Supra tokamak using the D-band of X-mode reflectometer from the low field side of the torus.

4.2.3.1. Probing with equidistant spatial step

In this section the interpretation of RCR measurements held during shots #46323 and #46333 are presented. Plasma core was probed by $N_\omega = 80$ electromagnetic wave with probing frequencies $115GHz < f < 135GHz$ with equidistant spatial step $\delta\Delta \approx 0.6cm$ within the probing interval $2.24m<R<2.74m$ $(0 < r/a < 0.6)$, reference frequency was $f_0 = 125GHz$ possessing probing wave length $\lambda \approx 0.2mm$. The parameters of probing are as follows: N_s=250, N_Ω=100.

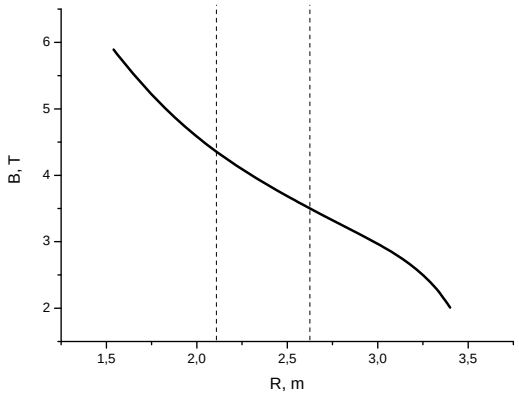

Figure 4.9. Magnetic field profile, shots #46323 and #46333. Vertical dashed line show probing interval.

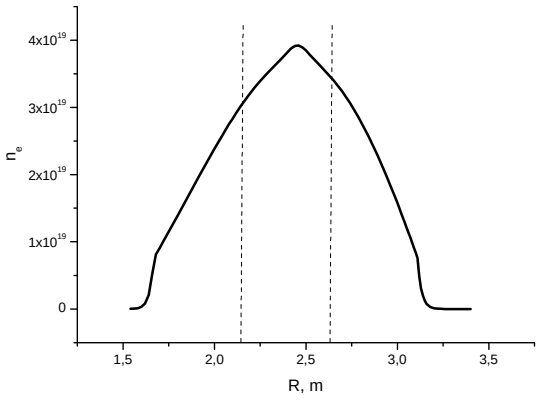

Figure 4.10. Plasma density profile, shots #46323 and #46333. Vertical dashed line show probing interval.

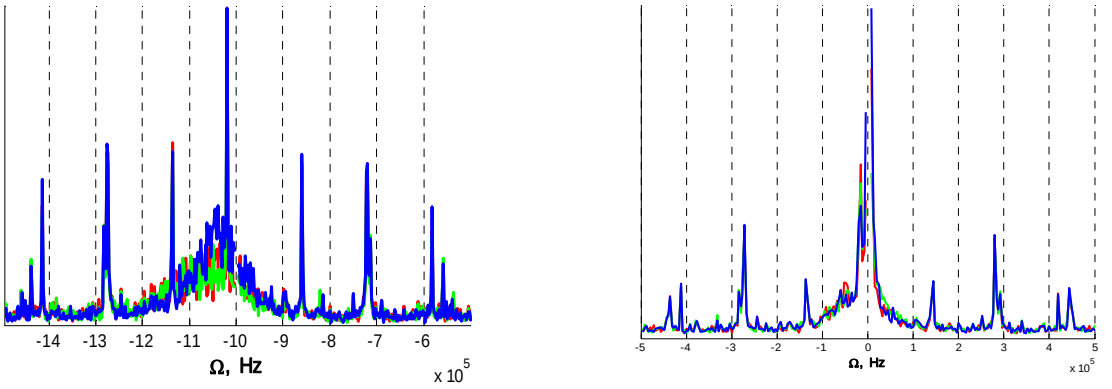

Figure 4.11. Signal frequency spectrum, shot #46323(a) and shot # 46333(b).

Magnetic field profile is shown in figure 4.9, plasma density profile is presented in figure 4.10. Vertical dashed lines show the spatial probing interval in the center of plasma. Actually the probing interval covers the very center of plasma nd the top of plasma density profile where strong MHD activity takes place. This strongly influences on obtained result overlapping the information in the received signal coming from turbulence.

In figure 4.11 it is clearly seen that signal frequency spectrum possesses a shift of ~0.5kHz, moreover parasitic frequencies could be observed on the both spectra for shots # 46323 (a) and #46333 (b).

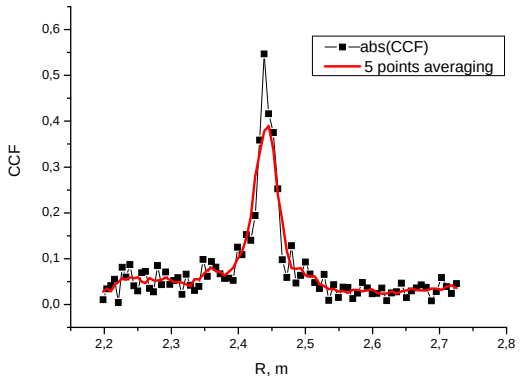

Figure 4.12. Absolute value of experimental signal RCR CCF (black squares) and smoothing interpolation (red line), shot #46323.

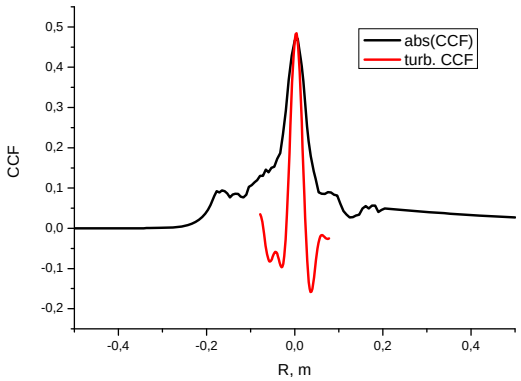

Figure 4.13. Absolute value of signal RCR CCF (black line) compared to normalized reconstructed TCCF (red line), shot #46323.

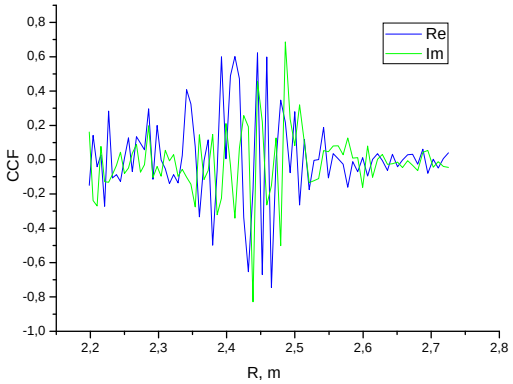

Figure 4.14. Experimental signal RCR CCF real (blue line) and imaginary (green line) parts, shot #46333.

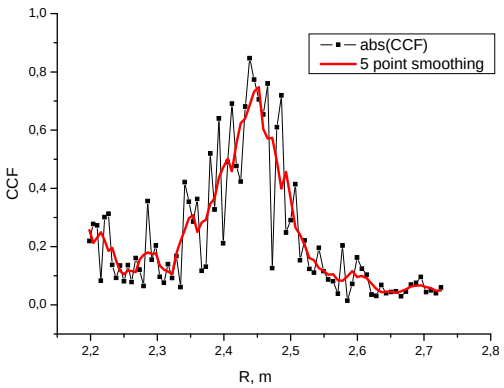

Figure 4.15. Absolute value of experimental signal RCR CCF (black squares) and smoothing interpolation (red line), shot #46333.

Signal RCR CCF real (blue) and imaginary (green) parts shown in figure 4.14 (shot #46333) demonstrate oscillatory behavior with slowly decreasing amplitude with growing distance from the reference cut-off position. The maximum value of the signal RCR CCF absolute value is damped for both shots #46323 (see figure 4.12) and #46333 (see figure 4.15) due to the presence

of background experimental noise caused by hardware and cross talk of the probing signals. Red line in figures 4.12 and 4.15 shows the result of the 5-point averaging smoothing interpolation procedure applied to the CCF functions in order to apply further Fourier transform and inverse procedure (148).

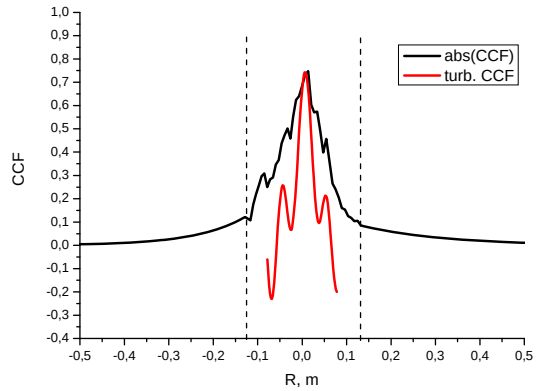

Figure 4.16. Absolute value of signal RCR CCF (black line)
compared to normalized reconstructed TCCF (red line), shot #46323.

In figures 4.13 and 4.16 vertical dashed line shows the positions at which the RCR CCF is cut and further extrapolated by decaying exponential function. TCCF is shown by red in these figures. Obviously the turbulence correlation length is significantly smaller than signal RCR correlation length however this result is preliminary and allows only approximate estimation of turbulence correlation length of the order $l_c \approx 5mm$ at reference cut-off position R=2.45m ($r/a = 0.27$) comparing to the signal RCR correlation length of the order $l_c \approx 4cm$. This also implies that chosen spatial probing step is two times larger than is was required after numerical simulations in Chapter III.

4.2.3.2. Probing with exponentially growing spatial step

RCR measurements have been held at Tore Supra tokamak (shots #47669-47686) during summer 2011 campaign using the D-band of the X-mode reflectometer installed from the low field side of the torus. List of shots is shown in table 4.2.

Table 4.2. List of shots of the campaign on the 23rd of June 2011.

Shot №	Conditions	Frequency range, GHz, (Number of frequencies)	Reference frequencies, GHz
47669	I_t=1250A	133..143 (20)	138, 5 windows
47670	5 plateaus I_p	113..123 (20)	118, 5 windows
47671	---||---	119..129 (20)	124, 5 windows

47672	---||---	125..135 (20)	130, 5 windows
47673	---||---	131..141 (20)	136, 5 windows
47674	---||---	137..147 (20)	142, 5 windows
47675	---||---	143..153 (20)	148, 5 windows
47676	---||---	116..126 (20)	121, 5 windows
47677	---||---	122..132 (20)	127, 5 windows
47679	---||---	145..155 (20)	150, 5 windows
47680	I_p =0.9MA, 4 plateaus n_e	110..120 (20), 113..123 (20)	115, 118
47681	---||---	116..126 (20), 119..129 (20)	121, 124
47682	---||---	122..132 (20), 125..135 (20)	127, 130
47683	---||---	127..137 (20), 131..141 (20)	133, 136
47684	---||---	134..144 (20), 137..147 (20)	139, 142
47685	---||---	140..150 (20), 143..153 (20)	145, 148
47686	---||---	140..160 (20), 147..157 (20)	150, 152
47689	I_p =0.9MA	113..123 (20), 120..140 (20)	118, 130

The target of the campaign was to follow the evolution of the turbulence correlation length at fixed position depending on plasma density or plasma current. Shot #47669 was held with stationary parameters and was performed in order to obtain result with maximum statistics and will be considered further.

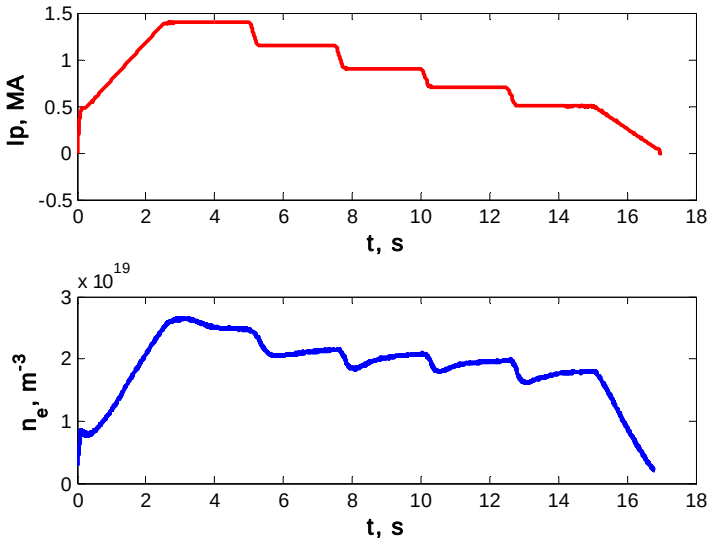

Figure 4.17. Plasma current plateaus (a) and plasma density plateaus (b) evaluation during shot #47670.

During each of shots ##47670-47679 plasma 5 plateaus of plasma current have been realized (see for an example of shot #47670 figure 4.17(a)). As it could be seen from figure 4.17(b) (shot

#47670) plasma density at fixed position $r/a = 0.5$ has been changed as well according to plasma current. Unfortunately during each plateau plasma parameters were not stationary and therefore RCR results are not reliable for this set of shots.

Firstly we discuss the data obtained during the shot #47669 due to sufficient statistic for the analysis, plasma density profile (t=7s, $f_0 = 138GHz$, $R_0 = 2.024m$) is shown in figure 4.18. Black vertical lines show the spatial probing interval Δ which is situated at the high field side of the plasma in the close to linear plasma density profile behavior region.

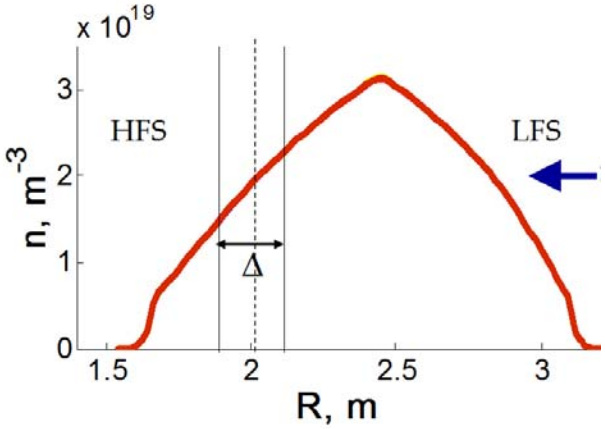

Figure 4.18. Plasma density profile. Shot #47669, t=7s, $f_0 = 138GHz$, $R_0 = 2.024m$.

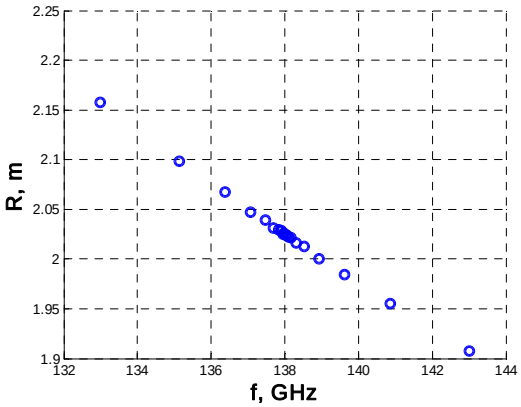

Figure 4.19. Shot #47669. Cut-off position versus probing frequency.

Exponentially growing distance between the cut-off positions was chosen for the experiment (20 points per $\sim 25cm$, corresponding to $f = 138 \pm 5GHz$), see figure 4.19.

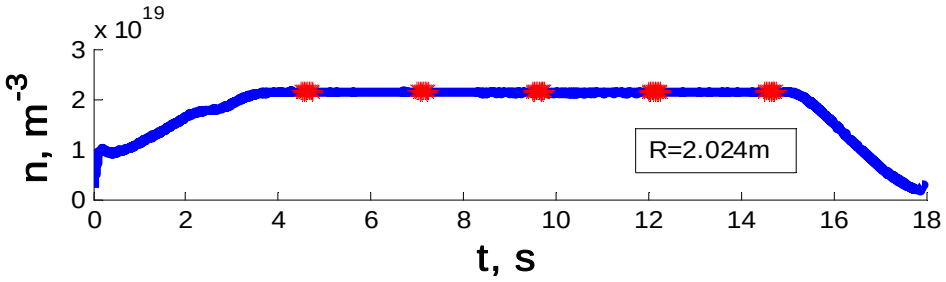

Figure 4.20. Shot #47669. Plasma density, R=2.024m. Red points show the windows of RCR experiment.

In figure 4.20 the plasma density dependence on time at R=2.024m is shown. The window parameters are as follows: N_ω=20, N_s=100, N_Ω=100 that corresponds to the turbulence frequency range $\Delta\Omega = 1MHz$, time step $\delta t = 1\mu s$ window duration $\Delta t = 2s$ .We indicate the time positions of the windows by red circles. It is clearly seen that plasma density is stable from

t=4s till *t=15s*. Frequency spectrum ($f_0 = 138GHz$) is shown in figure 4.21. The averaging is held over 5 windows of the shot #47669.

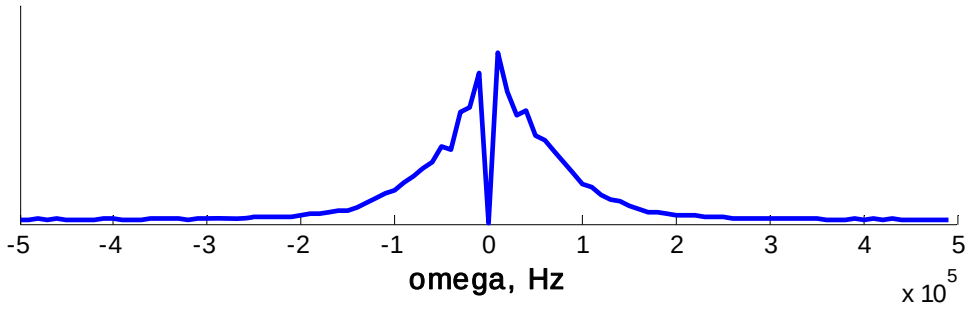

Figure 4.21. Shot #47669. Frequency spectrum.

Exponentially growing sweeping frequency step allows from the one hand to measure the vicinity of the reference cut-off position more carefully and simultaneously to pay less attention to the tail of signal RCR CCF. On the other hand unfortunately this choice of the frequency step introduces additional difficulties into data interpretation. Thus the first step of data analysis according to (148) is FFT applied to measured RCR CCF that requires equidistant spatial step of measurements. In order to compensate the shortage of points in the RCR CCF the cubic spline interpolation procedure is applied. The example of comparison between the RCR CCF before and after interpolation is shown in figure 4.22 (real part) and figure 4.23 (imaginary part) for $\Omega = 160kHz$.

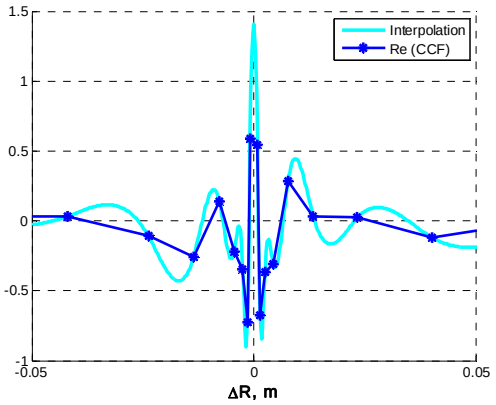

Figure 4.22. RCR CCF and interpolations, real part. $\Omega = 160kHz$

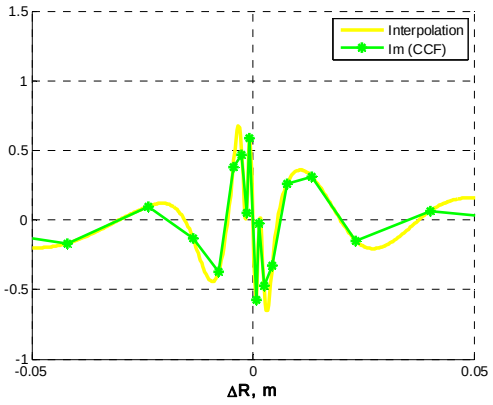

Figure 4.23. RCR CCF and interpolations, imaginary part. $\Omega = 160kHz$

The waveguide dispersion and the vacuum propagation is removed using a wall reflection signal which is acquired before each shot. The calibration phase Φ_{cal} is extracted by unwrapping the angle of the complex signal according to (201). It is clearly seen that after phase correction the real part of the signal RCR CCF almost coincides the absolute value of the CCF and imaginary part oscillates around zero (see figure 4.24).

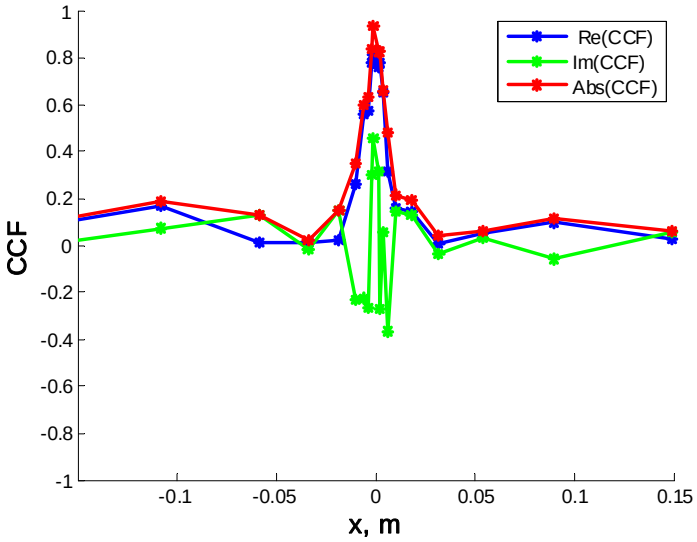

Figure 4.24. Shot #47669. RCR CCF real part (blue), imaginary part (green) and absolute value (red). $\Omega = 100kHz$.

The turbulence radial wave number spectrum was reconstructed according to (148) in the range of turbulence frequencies $\Delta\Omega = 1MHz$ after the extrapolation procedure at $\Delta R = 0.02m$. The spectrum reconstructed from the experiment agrees with the behavior $n_\kappa^2 \propto \kappa^{-3}$ for $5cm^{-1} < |\kappa| < 10cm^{-1}$ obtained with the Doppler reflectometry technique in [47] and [66], the spectrum growth at small wave numbers saturates for $1cm^{-1} < |\kappa| < 5cm^{-1}$ and shows slow decay for $|\kappa| < 1cm^{-1}$, within $\delta\kappa \approx 0.04cm^{-1}$ (see figure 4.25).

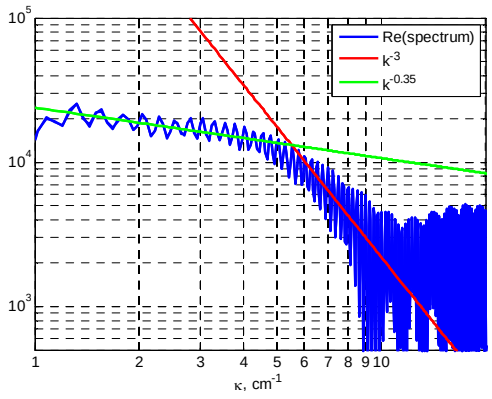

Figure 4.25. Reconstructed turbulence wave number spectrum. $\Omega = 100kHz$

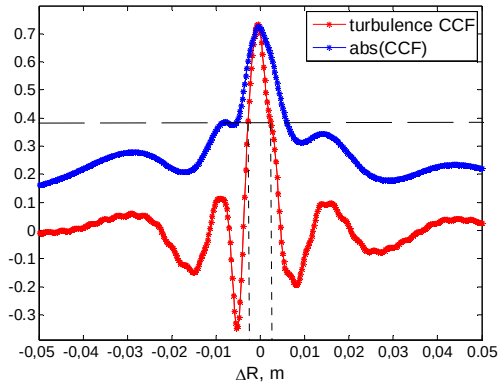

Figure 4.26. Signal RCR CCF (blue) and TCCF (red). $\Omega = 100kHz$

TCCF (red line in figure 4.26) was computed as a Fourier transform of the spectrum and its correlation length was estimated rather low, as $l_c \approx 2\text{mm}$ at *R=2.024*m.

During each of shots ##47680-47686 5 plasma density plateaus have been realized. In figure 4.27 plasma density at the position $r/a = 0.5$ and plasma current evaluation (shot #47685) are shown analogous to figure 4.17. Red circles mark the time position of RCR measurements.

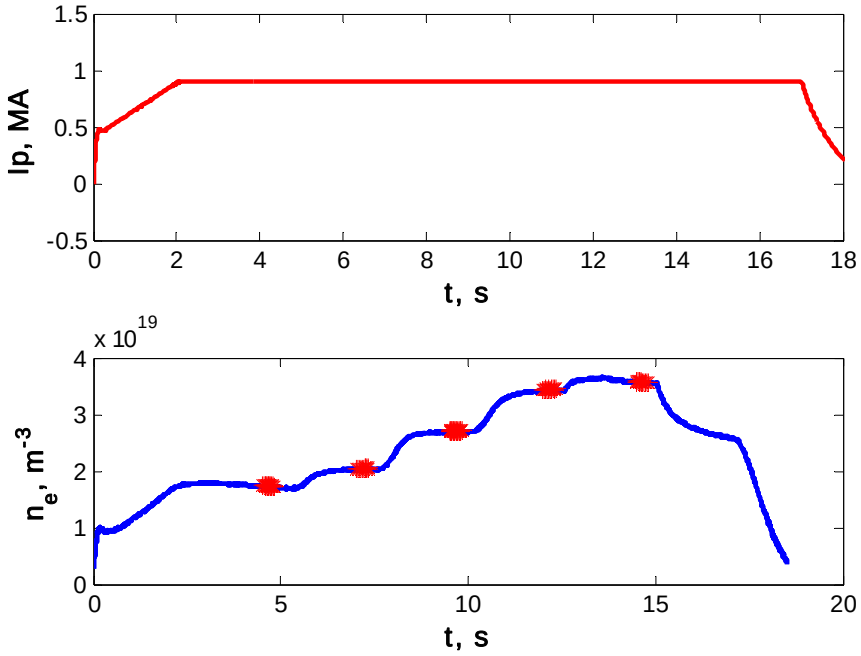

Figure 4.27. Plasma current plateaus (a) and plasma density plateaus (b) evalution during shot #47685.

The analysis of shots #47680-47686 shows the value of the turbulence correlation length of $l_c \approx 0.004 \pm 0.0025m$ at $0.3 < r/a < 0.8$. It was also shown that CCF decays much faster than the signal CCF in agreement with theoretical predictions [106, 76], $L/l_c \approx 5$ where *L* is *1/e* CCF level.

4.2.4. Summary

As an important result of the first RCR experimental campaign at Tore Supra the optimal experimental parameters are determined and the possible behavior on turbulence wave number spectra and the range of turbulence correlation length are estimated. The results obtained after the processing of the data seem to be very promising however some difficulties were faced when computing the spectrum and its spatial correlation function. Thus, exponentially growing probing step introduces addition difficulties when performing FFT while at the same time such a choice allows to measure RCR CCF in wider spatial interval. The choice of the reference cut-off position as well as the probing spatial interval should be accounting for conditions at which the inverse relation was derived, namely in the region of close to linear plasma density profile. During the probing window plasma parameters should be stationary, the phase calibration is also needed. In this section wide possibilities of RCR diagnostic have been demonstrated. To obtain more precise data further experiments are needed.

4.3. Experimental results obtained at FT-2 tokamak

FT-2 tokamak was described in section 1.3.1.2. In this section we present the reflectometry hardware installed at the tokamak, data analysis methods and results of two RCR experiments.

4.3.1. Radial correlation reflectometers at FT-2

First radial correlation reflectometer was installed at FT-2 tokamak in 2009 and then first measurements in X-mode from LFS were held. Measurements from HFS started in summer 2011 and the results from this campaign are presented in this section. Currently a double antenna sets for O- and X-mode are installed from both LFS and HFS and allow measurements in O- and X-modes utilizing Ka (26.5 – 40 GHz) and V (50 – 75 GHz) bands for probing frequencies in RCR experiments.

In figure 4.28. the scheme of 8-mm radial Ka-band correlation reflectometers installed from the HFS of the FT-2 tokamak is shown [136]. The horns are shifted from the equatorial plane of the tokamak by -16mm. Also the horns could be moved for ± 20mm from the equatorial plane.

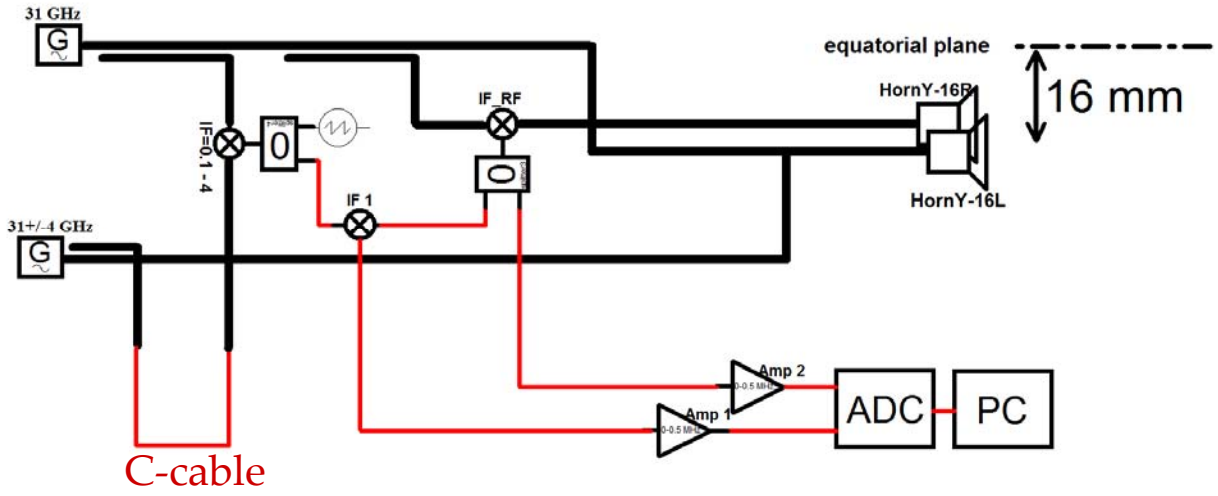

Figure 4.28. Radial correlation reflectometer, $\lambda = 8mm$. The horns are shifted by 16mm from the equatorial plane of the tokamak. C-cable should make equal time delay in arms going to mixer IF 1 at varied frequency channel. [137]

Calibration is realized by the C-cable installed in the probing frequency line. It makes equal time delay in arms going to mixer IF 1 at varied frequency channel. Mathematical calibration is also possible as:

$$\Delta\phi = \phi_0 + \phi(t_d) = \phi_0 + \Delta\omega \cdot t_d \qquad (202)$$

where ϕ_0 is the constant phase shift, t_d is the time delay, $\Delta\omega$ is the frequency shift between probing channels.

The probing is realized as follows: during a series of shots with equal conditions the frequency is shifted, one frequency separation per shot. Hence the statistics collected depends only on conditions of specific shot. Therefore the RCR experiment on FT-2 tokamak is quite hard to realize – to compute a single signal RCR CCF it is required to launch more than N_ω shots with the same conditions instead of Tore Supra or JET tokamaks.

4.3.2. O-mode probing from HFS

Here we present the results obtained on the 12th of July 2011. The measurements were carried out in O-mode in equatorial plane from HFS of the FT-2 tokamak. The experimental plasma density profile is shown in figure 4.29. The plasma density profile behavior in the probing region is close to linear therefore the method developed in Chapter II could be applied.

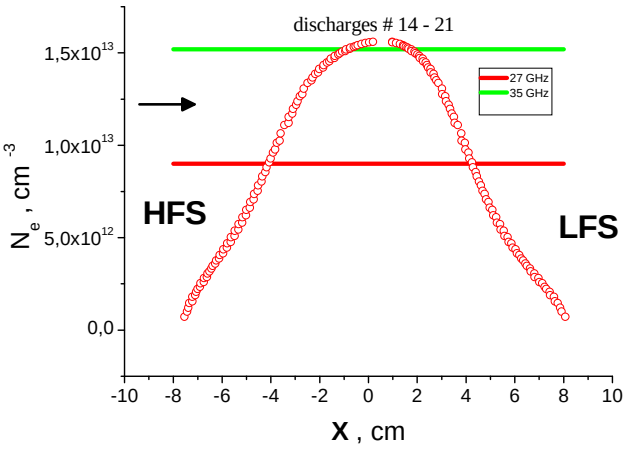

Figure 4.29. Plasma density profile 12 July 2011

In table 4.3 typical plasma and reflectometer parameters of the current experiment are shown. Equidistant frequency step of probing was chosen what is crudely equal to equidistant spatial step in case of close to linear plasma density profile (50 points per $\sim 3cm$, corresponding to $f_0 \pm 4GHz$, $f_0 = 31GHz$). The reference frequency cut-off is defined at $r/a = 0.37$ ($x = -0.055m$). the averaging was made over $N_s = 155$ samples within plateau duration of $t_{plateau} = 2ms$ and time step $t_{step} = 0.4\mu s$.

Table 4.3. Experimental parameters 12 July 2011

Parameter	Value
B_t	2.1 T

I_p	19kA
$n_e(0)$	$1.51 \cdot 10^{13} cm^{-3}$
T_e	200 eV
reference frequency f_0	31 GHz
probing range Δf	± 4 GHz
probing frequency step δf	0.1 GHz
probing interval Δ	3cm (± 1.5cm)

The obtained real (black squares in figure 4.30) and imaginary (black squares in figure 4.31) parts of the signal RCR CCF are shown for the turbulent fluctuation frequency 160kHz. As it is seen in the figure, the imaginary part is much smaller than the real one; however both only slowly decay with growing separation of probing wave cut-offs. As it is seen from figure 4.32 the coherence is low (less than 0.3 a.u.) due to geometry of horn, low mode selectivity of antennae and high noise level. Red line shows the result of 5-point smoothing procedure. The extrapolation procedure by exponential functions was applied to both real and imaginary parts at $|x| > 0.015m$ (see figure 4.32).

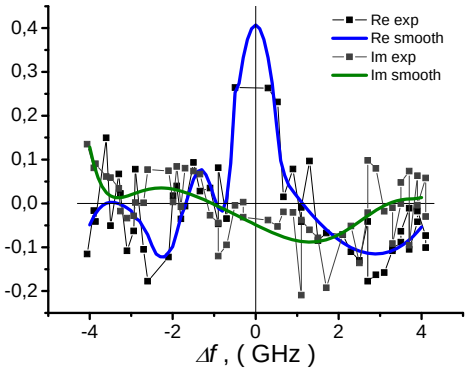

Figure 4.30. Signal RCR CCF, real part, $\Omega = 160kHz$.

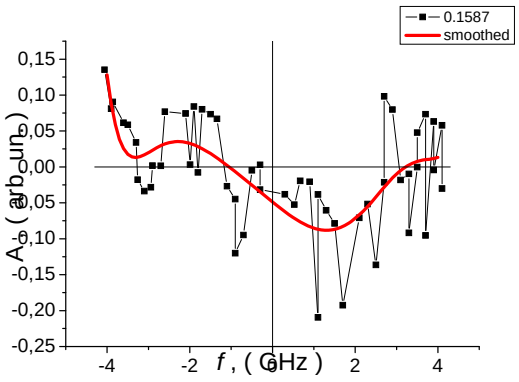

Figure 4.31. Signal RCR CCF, imaginary part, $\Omega = 160kHz$.

A very wide (lasting without decay till the reflectometry Bragg limit equal to 14.7cm^{-1} for maximum probing frequency $f = 35GHz$) turbulence κ-spectrum (real and imaginary parts) obtained using procedures of from the measured CCF is shown in figure 4.33. The accuracy of spectrum reconstruction (estimated using the spectrum imaginary part and negative bursts of real part) is not high, less than 1.5a.u., however sufficient for the spectrum width estimation. It corresponds to the turbulence correlation length substantially smaller than 0.5cm. This estimation agrees qualitatively with the value of typical turbulence spatial scale obtained at FT-2 with enhanced scattering diagnostics [107] and provided for FT-2 by ELMFIRE full-f

gyrokinetic modeling (see figure 4.39.). Long-scale fluctuations are suppressed in the spectrum for $|\kappa| < 1$ cm^{-1}, this suppression is also present in Fourier transform of the signal RCR CCF (shown in figure 4.32 by red line) which is probably a shortcoming of the 1D model used in the reconstruction procedure. Unfortunately the spectrum determined in this experiment does not perform explicit behavior and we do not compare it here to the usual spectra functions shown in section 1.4.4.

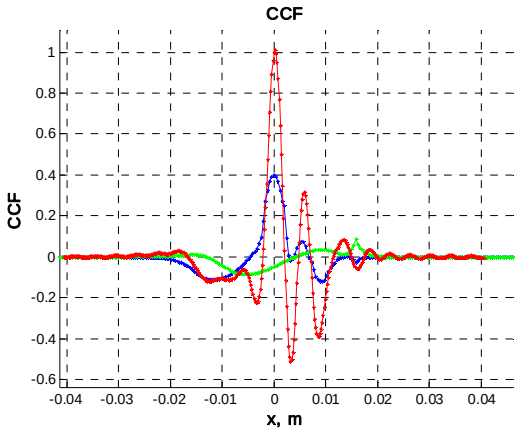

Figure 4.32. Signal RCR CCF (blue real and green imaginary) and TCCF (red), $\Omega = 160kHz$.

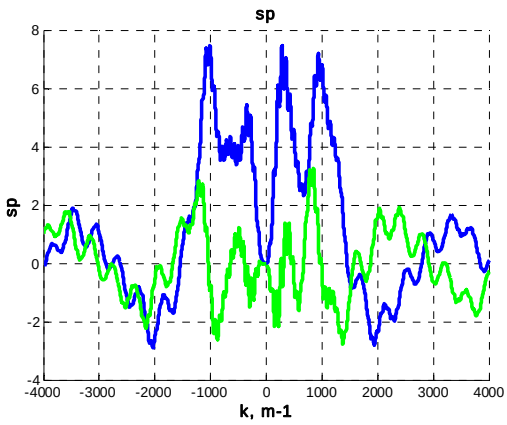

Figure 4.33. Turbulence radial wave number spectrum (blue real and green imaginary), $\Omega = 160kHz$.

The comparison of signal RCR CCF and TCCF is shown in figure 4.32. As it is seen from the figure, the signal RCR CCF possesses slower decay than TCCF however the functions are quite close. The oscillations in the signal RCR CCF and the similarity of the functions could be explained by the suppression of wave number spectrum for low κ as it was shown in 1D numerical computations in the paper [76].

4.3.3. X-mode probing from HFS

The spectrum decay at high wave numbers was studied with 60 GHz X-mode probing from the HFS of the torus on the 19th of April 2012. The experimental plasma density profile is shown in figure 4.34. Analogous to the previous sub-section the probing interval covers region of linear behavior of plasma density profile. In table 4.4., the parameters of the current experiment are shown. Equidistant frequency step of probing was chosen what is approximately equal to equidistant spatial step in case of close to linear plasma density profile (50 points per $\sim 3cm$, corresponding to $f_0 \pm 3GHz$, $f_0 = 60GHz$). Signal wave frequency step δf varied from 0.025 to 0.1 GHz The reference frequency cut-off is defined at $r/a = 0.37$ ($x = -0.055m$). The averaging was made over $N_s = 155$ samples within plateau duration of $t_{plateau} = 2ms$ and time step $t_{step} = 0.4\mu s$ that corresponds to $\Omega_{\max} = 1.25MHz$.

Table 5.4. Experimental parameters 19 April 2012

Parameter	Value
B_t	1.8 T
I_p	19kA
$n_e(0)$	$3 \cdot 10^{13} cm^{-3}$
T_e	500 eV
reference frequency f_0	60 GHz
probing range Δf	± 3 GHz
probing frequency step δf	0.025..0.1 GHz
probing interval Δ	3cm (± 1.5cm)

The double antenna set was shifted out of equatorial plane by 1.5 cm that corresponds to poloidal probing wave number of 3 cm^{-1}. The corresponding reflectometry (Doppler) spectrum shifted by 400 kHz from the probing frequency is shown in figure 4.35.

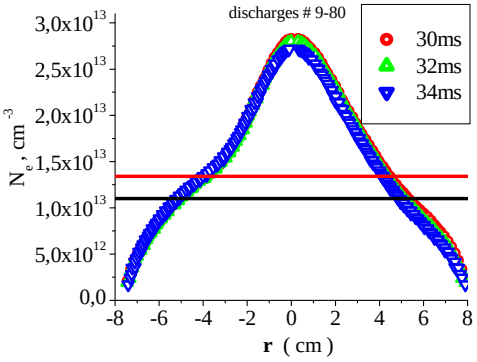

Figure 4.34. Plasma density profile 19 April 2012.

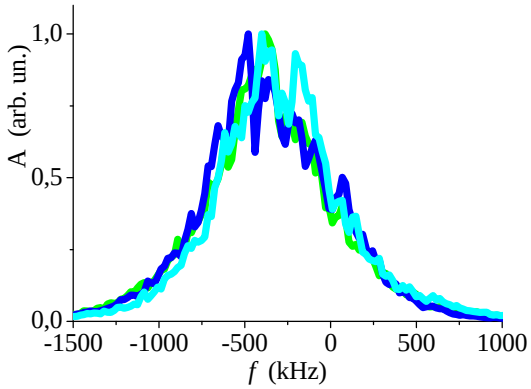

Figure 4.35. Quadrature reflectometer spectrum.

The CCF absolute value (coherence) is shown in figure 4.36. to be finite only for cut-off separation less than 0.5cm. The signal correlation length is decreasing with growing turbulence frequency and reaches the value of 0.05cm at 1.2MHz. The coherence oscillations at small turbulence frequency are produced presumably by contribution of reflection at the plasma boundary to the fluctuation reflectometry signal.

Radial wave number spectrum shown in figure 4.37. The width of this spectrum is growing with the turbulence frequency demonstrating a clear dispersion. The suppression of the spectrum at very small wave numbers is most likely related to the limitations of the 1D model analogous to the previous sub-section. The turbulent density fluctuation two-point correlation function is provided by the Fourier transform of the experimentally obtained spectrum in which only the contribution of physically sensible part within the Bragg limit is accounted for. The result of this transform is shown in figure 4.38.

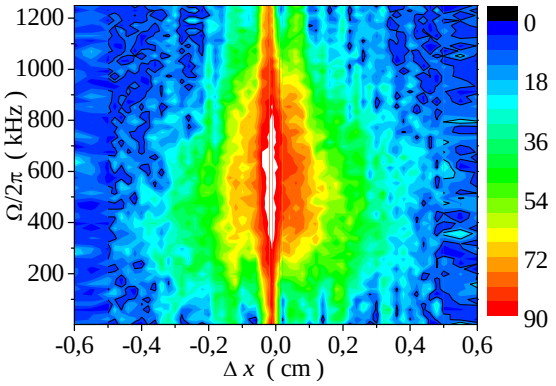

Figure 4.36. CCF coherence.

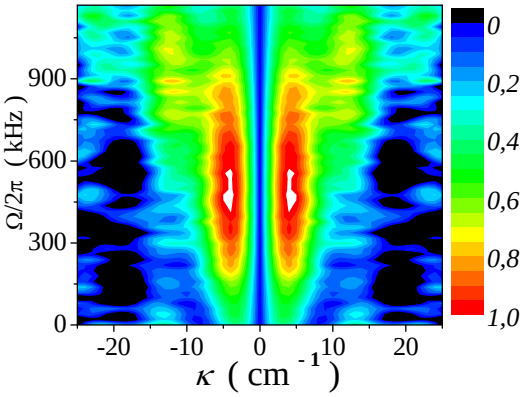

Figure 4.37. Turbulence wave number spectrum.

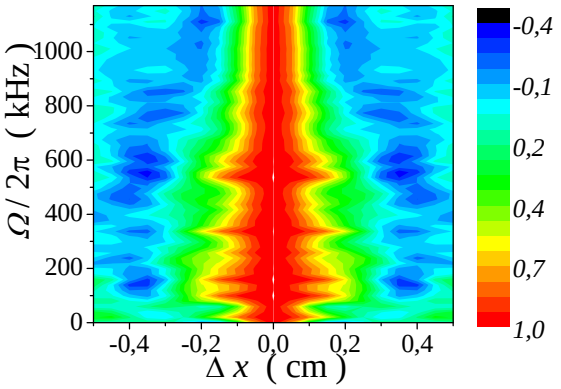

Figure 4.38. TCCF.

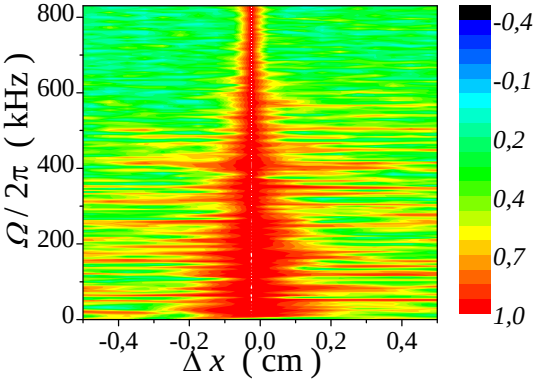

Figure 4.39. TCCF, ElmFire fullwave gyrokinetic global modeling. [137]

TCCF shown in figure 4.38. demonstrates decrease of the correlation length with growing frequency. This result of the turbulence wave number spectrum reconstruction from the experimental signal RCR CCF agrees qualitatively with the density fluctuation CCF obtained for the 1.5 higher density 19 kA FT-2 discharge as a result of ELMFIRE full-f gyrokinetic global modeling and shown in figure 4.39. However there is negative part for $|\Delta x| > 0.2cm$ in the experimental function which is absent in simulations. This could be explained by the suppression of low wave numbers is experimentally obtained spectrum and by shortcoming of 1D theory in application to FT-2 small machine. It should be mentioned as well that very small correlation length values obtained numerically for turbulence frequency higher than 600kHz are smaller than the computation grid and therefore not reliable.

4.3.4. Summary

It is important to underline that all the results presented here are obtained at small tokamak FT-2 where small radius is *a=0.08m* and probing wavelength is $\lambda = 0.004m$ and the relation $L_0 f_0 / c \approx 2..10$. Due to small geometry of the device the 2D effect makes impact on the resulting signal RCR CCF, moreover the multiple reflection between cut-off and antennae takes place in

case of equatorial plane probing and spoils the resulting CCF. Apart from this the hardware quality should be improved. Presented results of experiments give an overview of possible turbulence wave number behaviour and correlation length. These experiments are preliminary and allow us to estimate the experimental parameters for future attempts. Summarizing the results we emphasize the successful application of the turbulence wave number spectrum reconstruction procedure from the RCR data at the FT-2 tokamak.

4.4. Results of experimental campaign at JET

Nowadays JET (described in section 1.3.1.3) is the largest and most powerful tokamak in the world. Its successors are ITER and a demonstration reactor DEMO. The primary task of JET is to prepare for the construction and operation of ITER. Therefore it is quite important to test the new diagnostic technologies in conditions preceding ITER. The goal of the experiments set in March 2012 was to reconstruct turbulence radial wave number spectrum and spatial turbulence cross correlation function and its correlation length using radial correlation reflectometry data at JET.

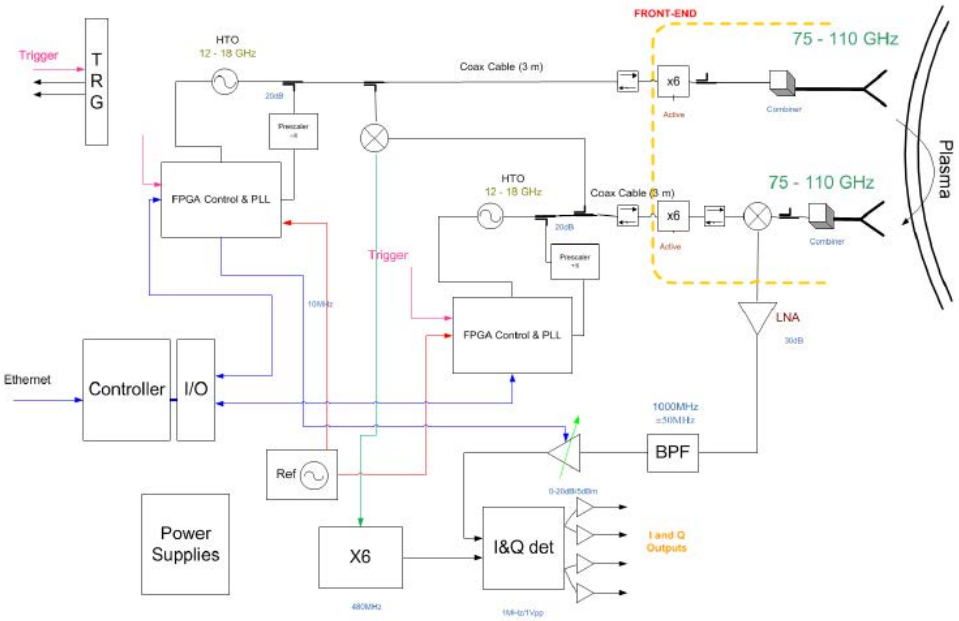

Figure 4.40. System layout, KG8C reflectometer.[138]

4.4.1. RCR diagnostic at JET

For the RCR measurements the usage of new KG8C broadband correlation reflectometer with I/Q detection installed at JET in February 2012 was planned. The new system suggested broadband operation (75 to 110 GHz), fast switching time ($50\mu s$ full band), high sensitivity (-90

dBm), good frequency resolution (100 kHz), low phase noise (-100 dBc/Hz at 100 kHz) and no internal cross talk [138]. The scheme of the KG8C reflectometer is shown in figure 4.13.

The reflectometer operates in in X- mode. The probing is realized in the mid-plane of plasma (z=29cm emitter, z=25cm receiver) JET plasma (see figure 4.14).

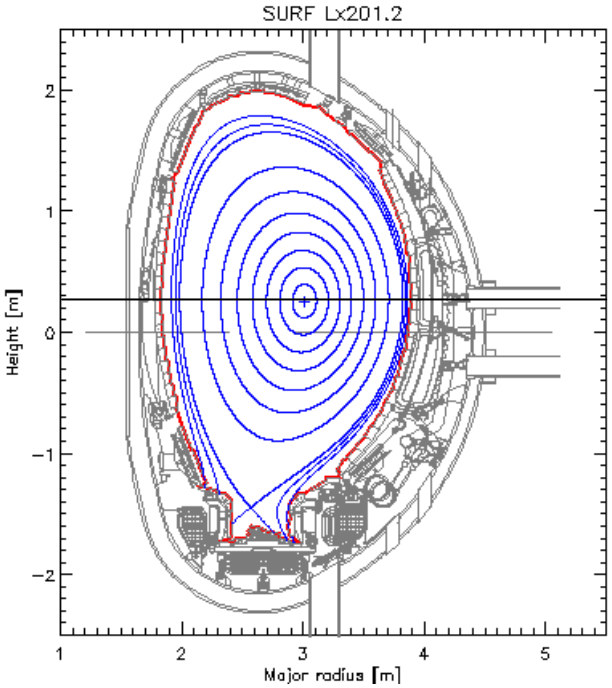

Figure 4.41. Flux surfaces from EFIT. Horizontal black line shows the line of sight of the reflectometer directed to the center of plasma.

Unfortunately in March 2012 the system did not operate completely and only one (master or reference) channel of the KG8C reflectometer was used. The sweeping (slave channel) of the reflectometer did not operate. It was decided to use another reflectometer, KG8B as a reference channel. Possessing less operational flexibility the KG8B reflectometer allowed to operate only at fixed 92 GHz channel and adjustable channel 85-89 GHz. Therefore the combined RCR system was created: the reference channel KG8B (85-89 GHz and 92 GHz) and sweeping channel KG8C (75-100 GHz). The correlation measurements were possible at two different reference radial positions simultaneously however these positions were not flexible. Main parameters of the RCR system are shown in table 4.5.

Table 4.5. Parameters of the RCR system at JET

Parameter	Value
Reference channel KG8B	85-89 GHz and 92 GHz
Sweeping channel KG8C	75-100 GHz
Sweeping time step	$0.5\mu s$

Data acquisition frequency	2MHz
Time of measurements	39-71s (1s before plasma)
Plateau duration	>10ms

4.4.2. Experimental results

During the March 2012 session several shots at JET were studied. As it could be seen from the table 4.6. only few of them (#82633 and #82671) can be analysed.

Table 4.6. List of shots analysed during March 2012.

Shot#	date	KG8B ref frq, GHz	KG8C master channel settings				comments
			start freq, GHz	freq step, MHz	Nstep	dwell time, ms	
82540	08/03/12	88/92	75.36	960	30	10.0	old KG8B settings, large step
82584-82588	12/03/12	88	86.4	30	100	5.0	error in data acquisition – dwell time 10.0ms
82586-82588	12/03/12	92	88.8	100	50	5.0	---||---
82633	**14/03/12**	**87/92**	**81.6**	**480**	**30**	**10.0**	**good for analysis**
82634-82636	14/03/12	-	-	-	-	-	attempt to use KG8C master+slave
82637	14/03/12	87	80.16	480	30	10.0	low density
82650-82667	15/03/12	87/92	76.8	2400	10	100.0	too long dwell t, too large frq step
82668-82670	16/03/12	87	76.8	480	5	100.0	not valid
82671	**16/03/12**	**87**	**80.16**	**480**	**30**	**10.0**	**good for analysis**
82672	16/03/12	87	80.16	480	30	10.0	not valid
82673-82674	16/03/12	87	80.16	240	60	5.0	error in data acquisition – dwell time 10.0ms
82749	26/03/12	87	84.96	480	10	10.0	not valid
82750	26/03/12	87	76.8	1200	18	20.0	---||---

4.4.2.1. Shot #82671 data analysis

Frequency evaluation during a single window in shot #82671 is shown in figure 4.22.

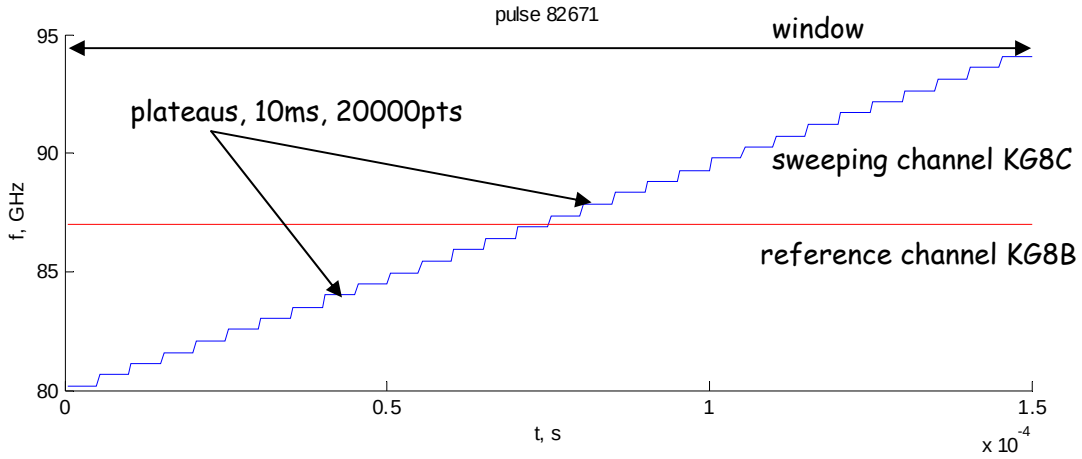

Figure 4.42. Frequency evaluation during a single window.

During 32s of the shot a sequence of 106 windows have been realized, during 1s without plasma and then from 40s till 71s. The settings of the RCR system are given in table 4.7.

Table 4.7. Parameters of the RCR system.

Parameter	Value
N_ω	30
Window duration	0.3s
Plateau duration	10 ms
N_s	200
N_Ω	100
Number of windows per shot	106
Number of points per shot	64000000
Reference frequency	87 GHz
Sweeping start frequency	80.16 GHz
Frequency step	480 MHz

After a shot, 64000000 points of data are acquired by both reference and sweeping channels I and Q parts of signal. To process the data we need to choose a time window of 0.3s (corresponding to probing window duration) during a stationary phase of plasma.

In figure 4.43 the plasma parameters dependence on time is shown. The magnetic field is computed using EFIT [139], plasma density profile is measured by KG10, LIDAR (magenta line in figure 4.43) and HRTS diagnostics. Vertical dashed lines show the time of the window start

positions at t=48.4s and t=59.7. These two windows (#32 and #69) have been chosen due to stationary plasma conditions in L-mode and H-mode. The same system settings give principally different results when measuring in L- or H-mode. Plasma density and magnetic field profiles are shown in figures 4.44 (L-mode) and 4.45 (H-mode).

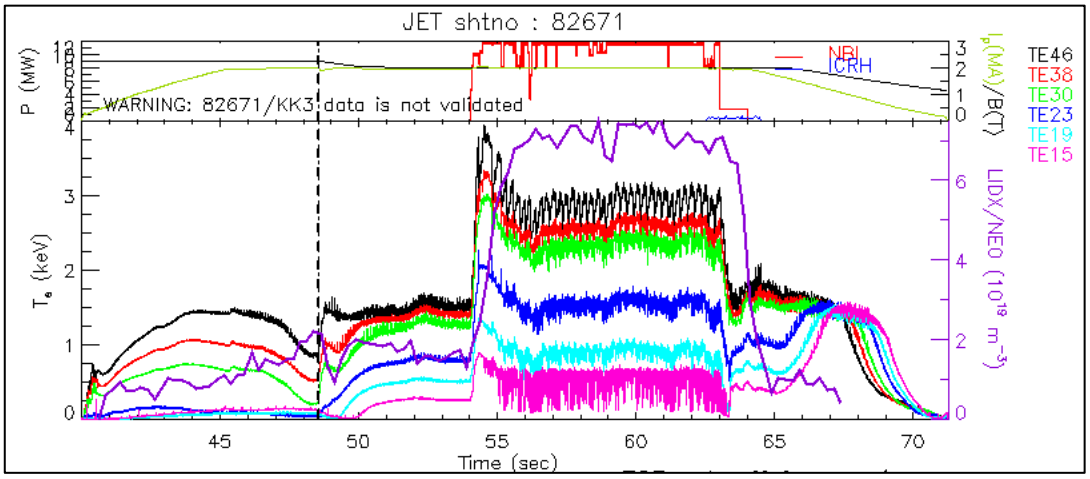

Figure 4.43. Frequency evaluation during a single window. Vertical dached line shows time positions of the two choosen windows in L-mode (t=48.4s) and in H-mode (t=59.7s).

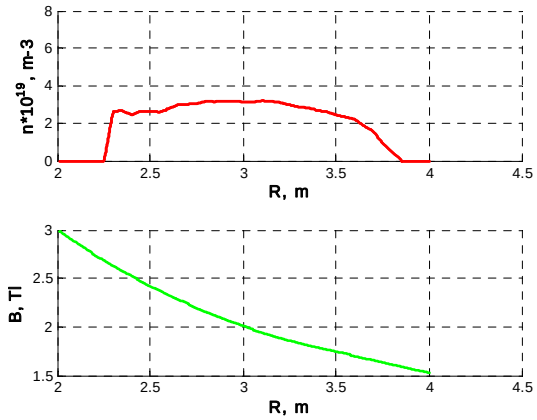

Figure 4.44. Plasma density profile (red) and magnetic field, L-mode, t=48.4s.

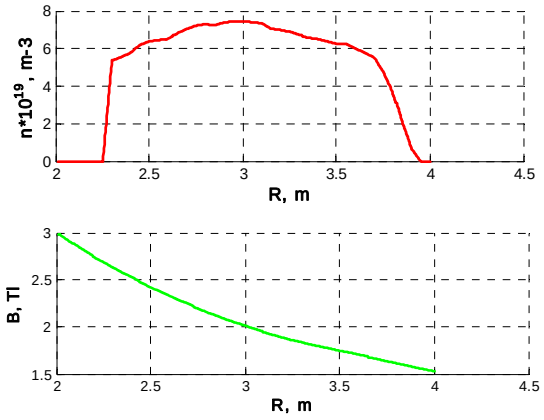

Figure 4.45. Plasma density profile (red) and magnetic field, H-mode, t=59.7s .

When probing in L-mode the probing wave reaches the core and the cut-off position range is quite wide, $2.303m < R < 3.296m$ it covers almost 90cm (see figure 4.46). The spatial step of measurements $\delta\Delta \approx 3cm$ is higher than expected correlation length $l_c \approx 1mm..1cm$. Therefore L-mode measurements require other system settings with lower spatial probing step.

In case of H-mode probing the probing zone is in pedestal zone and covers spatial interval of $2.303m < R < 3.296m$ (figure 4.47). In this case the spatial probing step $\delta\Delta \approx 4mm$ allows to measure qualitatively the turbulence correlation length. Unfortunately currently the probing frequency step is not possible to reduce due to technical limitations of the system.

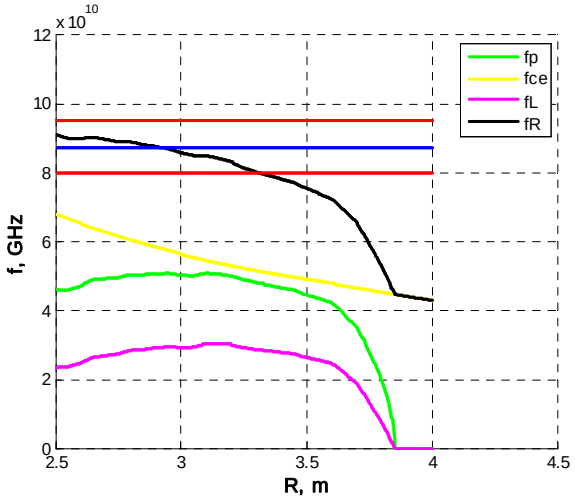

Figure 4.46. Frequency diagram. Black line shows upper cut-off for X-mode. $R_{max} = 3.296m$, $R_{min} = 2.303m$, $R_0 = 2.939m$.

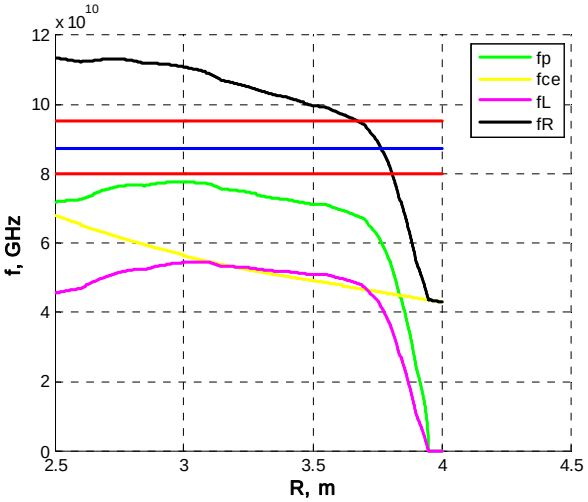

Figure 4.47. Frequency diagram. Black line shows upper cut-off for X-mode. $R_{max} = 3.811m$, $R_{min} = 3.672m$, $R_0 = 3.761m$.

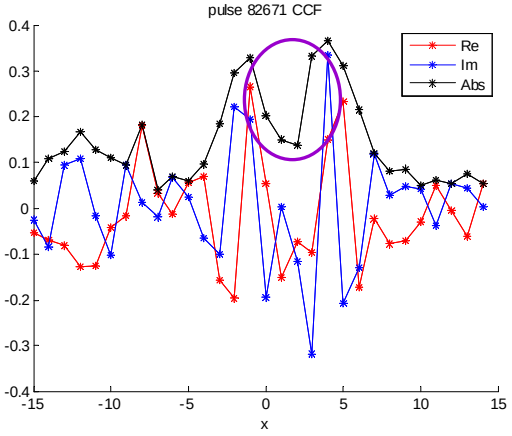

Figure 4.48. Signal RCR CCF, real part (red line), imaginary part (blue line) and absolute value (black line).

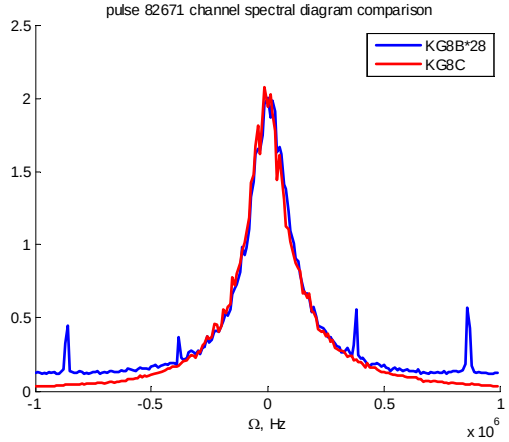

Figure 4.49. Channel spectra diagram comparison.

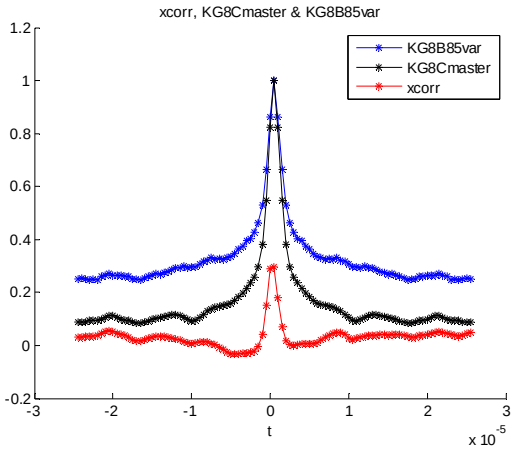

Figure 4.50. Autocorrelation functions, KG8B85var (blue), KG8C master (black) and cross correlation function (red).

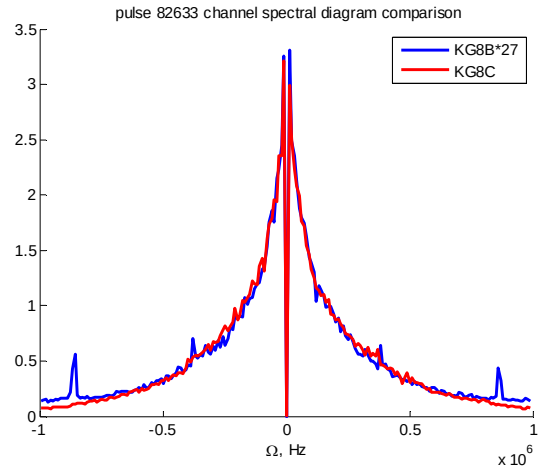

Figure 4.51. Channel spectra diagram comparison

The level of correlation between the two channels, reference KG8B and probing KG8C appeared to be rather low, below 0.4. Moreover the signal RCR CCF is damped for small ΔR (see figure 4.48, marked by magenta circle). Possible low level of turbulence in the top of pedestal comparing to the level of noise give this damping. However slow decay of the RCR CCF could be observed even substantially spoiled by high level of noise. The KG8B spectra turned to be significantly smaller than KG8C spectra as well as the signal level.

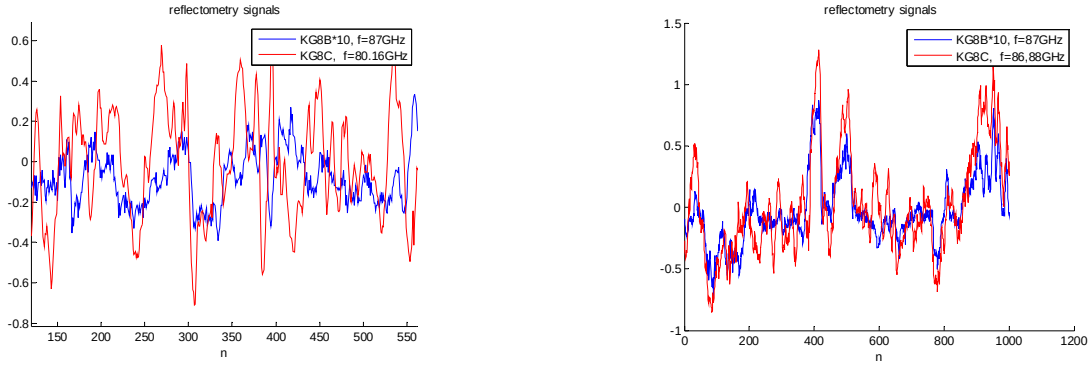

Figure 4.52. Signal comparison between the two channels

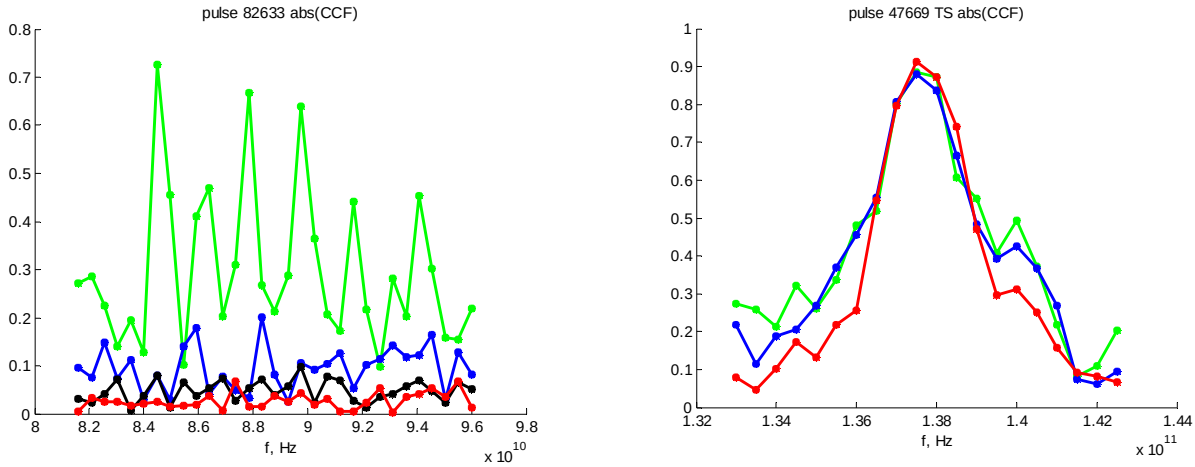

Figure 4.53. Absolute value of RFR CCF depending on number of samples of averaging N_s, $\Omega = 100kHz$, JET (a) and Tore Supra (b), shot #47669. The computations are done for $N_s = 10$ (green), $N_s = 100$ (blue), $N_s = 500$ (black) and $N_s = 1000$ (red).

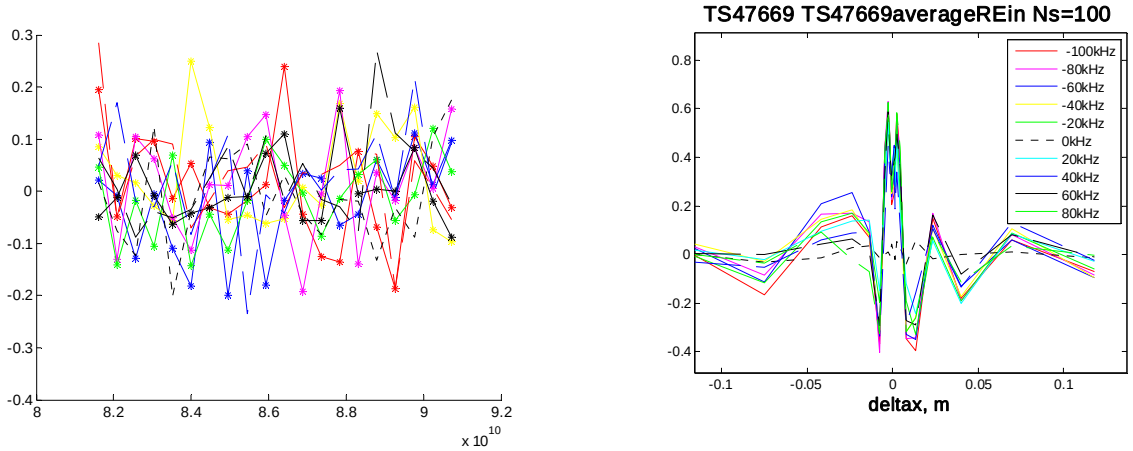

Figure 4.54. Re(CCF) for different turbulence frequencies. JET (a), $\Omega = 0..200kHz$ and Tore Supra (b), shot #47669, $\Omega = -100..80kHz$.

4.4.2.2. Shot #82633 data analysis

Analogous to previous subsection shot #82633 has been analyzed. Autocorrelation functions of the channels KG8B (shown in blue) and KG8C (black line) and cross-correlation function of these channels is shown in figure 4.50. The level of correlation between channels is rather low (<30%) and the correlation time estimated as $2*10^{-6}$ s is comparable to the sweeping time step $0.5*10^{-6}$ s. Channel spectra diagram represents the same result as for the shot #82671: the KG8B signal is damped however as it is seen from figure 4.52. where the signal comparison between the two channels is shown the signals seem to be correlated.

Dependence of RCR CCF absolute value on number of samples for averaging N_s for JET, at $\Omega = 100kHz$ is shown in figure 4.52.(a). The same algorithm has been tested with Tore Supra data, shot #47669 (figure 4.52.(b)). In is clearly seen that the behavior of signal RCR CCF obtained at JET is similar that of the noise with increasing statistics in contrary to the Tore Supra results.

We also compare the real parts of RCR CCF for JET (see figure 4.53.(a)) and Tore Supra (same figure (b)) for different turbulence frequencies. This result confirms the previous conclusion on random nature of the data obtained from JET.

4.4.3. Summary

Due to a problem of synchronization between the KG8B 85var/92fix channel and KG8C master channel no relevant physical result has been obtained. During the experimental session in March 2012 no correlation between channels observed, even signals seem to be correlated. The level of signal CCF decays when number of samples for averaging is increased (Figure 4.52.(a)), as it should be in case of white noise. The behavior of signal CCF depending on turbulence frequency is random (Figure 4.53.(a)). That is not the case for Tore Supra measurements, for example (Figures 4.52.(b), 4.53.(b)). This could be explained by several reasons, such as high level of noise and low level of signal in KG8B 85var/92fix channels; low level of turbulence in the top of pedestal comparing to the level of noise or position of the reference cut-off in transition region from pedestal to core.

Although there are no physical result due to the hardware default the preliminary measurements and system settings determination have been held. Thus, these preliminary experiments held using newly installed equipment allow to predefine the experiments parameters set for JET such as probing frequency step and range, window and plateaus duration according to technical abilities of RCR systems at JET. Apart from that the software focused on JET data processing has been developed and fully prepared for further usage when the hardware problems are resolved.

Conclusion

Turbulence is considered to be the main source of anomalous transport in tokamaks which leads to faster loss of heating than it was predicted by neoclassical theory. Consequently it makes measurements of turbulence properties important for better understanding of turbulence nature. Measurements of plasma density fluctuations are the easiest and provide information not only on the turbulence amplitude but also on its dispertion relation, frequency and wave number spectra and phase. Although plenty of turbulence diagnostic tools are already developed the problem of high quality turbulence properties measurements is still especially acute.

Reflectometry is a widely used method of plasma diagnostic in tokamaks. It provides information on averaged plasma density profile and on fluctuation properties as well. One of its applications, radial correlation reflectometry (RCR), studies correlation between the two signals received from plasma one at fixed frequency and the other with growing frequency difference with growing frequency difference. This correlation decay possesses a logarithmic slow behavior observed in majority of experiments looking at the plasma core [106]. However, numerical computations show that it differs from the turbulence correlation function dependency. The discrepancy predetermined subsequent erroneous approach in experiment data interpretation however it could be explained analytically.

This thesis is focused on new correct RCR data interpretation and covers the development of the innovative method providing from RCR data the turbulence characteristics such as radial wave number spectrum and turbulence radial correlation length from the theoretical model to experimental validation on various machines with completely different parameters.

Theoretical basis in Born approximation framework gives a correct analytical description of RCR signal dependency on turbulence radial wave number and explains the long tail of the signal RCR CCF in one dimensional geometry in linear regime. Furthermore the simple relation between measured in experiment signal RCR CCF and turbulence radial wave number spectrum is developed from the integral equation obtained for RCR CCF. The direct transform forward and inverse kernels are also proposed in order to simplify the calculation of turbulence parameters and reduce errors accumulating during numerical computations.

Numerical simulation is an intermediate step between the theoretical approach and the real world allowing to model real experiment and estimate required experimental settings. It is the first step in developing the methods of experimental data processing.

First application of the method has been realized at Tore Supra tokamak. As the prevalent results of the experiment turbulence radial correlation length was estimated in the range of l_c=0.5..0.8cm and the behavior of radial wave number spectrum for small wave numbers

$\kappa < 5cm^{-1}$ with good resolution of $\kappa \approx 0.04cm^{-1}$ which agrees with two-fluid model discussed in subsection 1.4.3 was studied as well.

Later RCR experiments was realized at small FT-2 tokamak and gave results consistent to the results obtained at Tore Supra: the estimated radial correlation length was in the order of l_c=0.1..0.8cm. However additional difficulties were faced at FT-2 due to small geometry of the machine and subsequent curvature of the cut-off layer. Obviously one dimensional approach gives rough description of electromagnetic wave propagation in the case of $L_0 f_0 / c \approx 2..10$ and does not take into account two dimensional effects such as small angle scattering. The inverse transform of the RCR CCF gives the general shape of radial wave number spectrum and does not allow us to exhibit a clear dependency.

The last, JET experiment was planned as a test of the proposed method for further development for ITER reflectometry systems. Unfortunately the installation of the new RCR system was not finished and great capabilities of new fast sweeping correlation reflectometer have not been used. The problem of synchronization between the two channels of different reflectometers was not resolved however even having no physical result the experimental campaign was quite fruitful. As a result of the experiment the equipments settings have been determined and necessary software for data processing has been developed.

Addressing to applications to ITER we should also discuss the limitations of RCR. On ITER the plasma density profiles are flat that means long probing wave path up to several meters. Therefore the reflectometer can suffer from destructive influence of plasma turbulence which may lead on one hand to multiple small angle scattering or strong phase modulation and on the other hand to a strong Bragg backscattering (BBS) or to an anomalous reflection [140]. This introduces additional difficulties of reflectometry data interpretations. Fortunately RCR is useful in case of strong phase modulation and in strong non-linear regime due to local monitoring of turbulence behaviour [141].

The contribution of the author to this work is in developing of the theoretical basis of the RCR, performing of the numerical modeling, participating the experimental sessions at three machines, Tore Supra in Cadarache, JET in Culham and FT-2 in Saint-Petersburg and all the data processing for these machines.

Future plans

We would like to underline that although the theoretical approach provides a strong basis for turbulence properties reconstruction it is not complete. Thus, the description of the scattering signal and expression for the RCR CCF in two dimensional model should be described and the 2D corrections for the inverse relation for turbulence radial wave number spectrum are required as well. This should explain the RCR CCF behavior in a small machine and discover the influence of 2D effects in huge machine such as ITER. Further the comparison between numerical 1D and 2D computations in Born approximation as well as full wave are needed.

Experimental applications of the method should be established. Future plans include application of the method to study the suppression of radial correlation length due to L-H transition or shear flows. The evolution of the wave number spectrum by the RCR technique could be measured as well.

After the hardware improvement at JET the attempt to apply the diagnostic should be continued as soon as conditions at JET machine are the closest to ITER.

Appendix

Appendix A. Stationary phase method

The main idea of stationary phase methods relies on the cancellation of sinusoids with rapidly-varying phase. It is a generalization of Laplace method for the following integrals:

$$I(x) = \int_a^b g(t) e^{ix\Psi(t)} dt \tag{203}$$

where $g(t)$ and $\Psi(t)$ are real functions. If inside the interval of integration $[a,b]$ a point $t = c$ where $\Psi'(c) = 0$ exists this point is called "stationary point" and it is possible to obtain an asymptotic form of the integral $I(x)$ using the Laplace method. The stationary point provides the main contribution to the integral $I(x)$ in the ε vicinity of the stationary point.

If $\Psi'(a) = 0$ and $\Psi'(t) \neq 0$ for $a < t \leq b$ the integral $I(x)$ can be splitted in two:

$$I(x) = I_1(x) + I_2(x) = \int_a^{a+\varepsilon} g(t) e^{ix\Psi(t)} dt + \int_{a+\varepsilon}^b g(t) e^{ix\Psi(t)} dt \tag{204}$$

The second integral $I_2(x)$ nullifies as $1/x$ if $x \to \infty$ because there is no stationary point in the interval $[a+\varepsilon, b]$. To obtain the asymptotical representation, the functions $g(t)$ and $\Psi(t)$ are replaced by their Taylor series:

$$I(x) \approx g(a) \exp[ix\Psi(a)] \int_a^{a+\varepsilon} \exp[i \frac{x}{p!} (t-a)^p \Psi^{(p)}(a)] dt, \; x \to \infty \tag{205}$$

The integration interval is enlarged by replacing ε by ∞, however the error introduced by this replacement nullifies as $1/x$ if $x \to \infty$ and is negligible. Substituting $s = (t-a)$:

$$I(x) \approx g(a) \exp[ix\Psi(a)] \int_0^{\infty} \exp[i \frac{x}{p!} s^p \Psi^{(p)}(a)] ds, \; x \to \infty \tag{206}$$

If $\Psi^{(p)}(a) > 0$ the contour of integration id turned for $\pi/2p$ otherwise $-\pi/2p$.Using the substitution

$$s = \exp[i \frac{\pi}{2p} \operatorname{sgn}(\Psi^{(p)}(a))] \left[\frac{p!u}{x\left|\Psi^{(p)}(a)\right|} \right]^{1/p} \tag{207}$$

the asymptotic form for $x \to \infty$ is obtained:

$$I(x) \approx g(a) \exp\left[i \left(x\Psi(a) + \frac{\pi}{2p} \operatorname{sgn}(\Psi^{(p)}(a)) \right) \right] \left[\frac{p!u}{x\left|\Psi^{(p)}(a)\right|} \right]^{1/p} \frac{\Gamma(1/p)}{p}, \; x \to \infty \tag{208}$$

For the stationary point $\Psi''(a) \neq 0$:

$$I(x) \approx (2\pi)^{1/2} g(a) \frac{\exp\left[i\left(x\Psi(a) + \frac{\pi}{4}\mathrm{sgn}(\Psi^{"}(a)) \right) \right]}{\left[x\left|\Psi^{"}(a)\right| \right]^{1/2}},\ x \to \infty \tag{209}$$

Appendix B. 4th order Numerov scheme

For the second-order derivative we use Taylor series:

$$\begin{aligned} E_z(x+h) &= E_z(x) + hE_z^{(1)}(x) + \frac{h^2}{2}E_z^{(2)}(x) + \frac{h^3}{6}E_z^{(3)}(x) + \frac{h^4}{24}E_z^{(4)}(x) + O(h^4) \\ E_z(x-h) &= E_z(x) - hE_z^{(1)}(x) + \frac{h^2}{2}E_z^{(2)}(x) - \frac{h^3}{6}E_z^{(3)}(x) + \frac{h^4}{24}E_z^{(4)}(x) + O(h^4) \end{aligned} \tag{210}$$

After adding the two expansions:

$$\frac{E_z(x+h) - 2E_z(x) + E_z(x-h)}{h^2} = E_z^{(2)}(x) + \frac{h^2}{12}E_z^{(4)}(x) + O(h^4) \tag{211}$$

We obtain from here:

$$E_z^{(2)}(x) = \frac{E_z(x+h) - 2E_z(x) + E_z(x-h)}{h^2} - \frac{h^2}{12}E_z^{(4)}(x) - O(h^4) \tag{212}$$

We substitute this expression for the second-order derivative (212) to the Helmholtz equation (169):

$$\frac{E_z(x+h) - 2E_z(x) + E_z(x-h)}{h^2} + 4\pi^2 N_0^2(x)E_z(x) = \frac{h^2}{12}E_z^{(4)}(x) + O(h^4) \tag{213}$$

The key point of the method is to apply the operator $\left[1 + \frac{h^2}{12}\frac{d^2}{dx^2}\right]$ to the Helmholtz equation (169):

$$\left[1 + \frac{h^2}{12}\frac{d^2}{dx^2}\right]E_z^{(2)}(x) + 4\pi^2 N_0^2(x)E_z(x) + \frac{h^2}{12}\frac{d^2}{dx^2}\left[4\pi^2 N_0^2(x)E_z(x)\right] = 0 \tag{214}$$

Again, using (211) we obtain:

$$\begin{aligned} &\frac{E_z(x+h) - 2E_z(x) + E_z(x-h)}{h^2} + O(h^4) + 4\pi^2 N_0^2(x)E_z(x) + \\ &+ \frac{h^2}{12}\frac{d^2}{dx^2}\left[4\pi^2 N_0^2(x)E_z(x)\right] = 0 \end{aligned} \tag{215}$$

All the terms of the fourth-order and higher are negligible. The term $\frac{h^2}{12}\frac{d^2}{dx^2}\left[4\pi^2 N_0^2(x)E_z(x)\right]$ is approximated by using the second-order scheme due to it has the factor h^2. After the expansion into Taylor series:

$$N_0^2(x+h)E_z(x+h) = E_z(x) + hE_z^{(1)}(x) + \frac{h^2}{2}E_z^{(2)}(x) + O(h^2)$$
$$N_0^2(x-h)E_z(x-h) = E_z(x) - hE_z^{(1)}(x) + \frac{h^2}{2}E_z^{(2)}(x) + O(h^2) \quad (216)$$

we add the two expansions and substitute to the equation (215) obtaining:

$$\frac{E_z(x+h) - 2E_z(x) + E_z(x-h)}{h^2} + 4\pi^2 N_0^2(x)E_z(x) +$$
$$+4\pi^2\left[\frac{N_0^2(x+h)E_z(x+h) - 2N_0^2(x)E_z(x) + N_0^2(x-h)E_z(x-h)}{12}\right] = 0 \quad (217)$$

This is a discreet equation with a fourth-order error term.

References

1. United Nations, Department of Economic and Social Affairs, Population Division, http://www.un.org/esa/population
2. Statistical tables from the International Energy Agency (IEA), http://www.iea.org/stats/docs/statistics_manual.pdf
3. The World Energy Council, http://www.worldenergy.org/publications
4. Statistical Review of World Energy, http://www.bp.com/statisticalreview
5. J. Ongena and G. Van Oost, "Energy for future centuries. Prospects for fusion power as a future energy source", Trans. Fusion Sci. Technol., February 2012 – Vol. 61, No. 2T, Proceedings of the Tenth Carolus Magnus Summer School on Plasma and Fusion Energy Physics, September, 4-16, 2011, Weert, The Netherlands
6. F. Joos, "The Atmospheric Carbon Dioxide Perturbation", Europhysics News, 27, 6, 213-218, 1996
7. J. Wesson, "Tokamaks", Third Edition, Clarendon Press, Oxford, 2004
8. H. A. Bethe, "Energy Production in Stars", Physical Review, Vol. 55, Issue 1: 103, January 1, 1939
9. L. A. Arzimovich, "Controlled thermonuclear reactions" (in Russian), M., 1963
10. P. A. Sturrock, T. E. Holzer, D. M. Mihalas and R. K. Ulrich, "Physics of the Sun, Vol. I: The solar interior", B. M. McCormac, Ed., Loockheed Palo Alto Research Laboratory, California, USA, 1986
11. An Abundance of Lithium, March 2008, http://www.worldlithium.com
12. University of Wisconsin-Madison, http://www.iec.neep.wisc.edu/operation.php
13. I. Langmuir, "Oscillations in ionized gases", Proc. Nat. Acad. Sci. U.S., vol. 14, p. 628, 1928; also available in The Collected Works of Irving Langmuir, vol. 5, C. G. Suits, Ed. New York: Pergamon, pp. 111-120, 1961
14. V. E. Golant, A. P. Zhilinskiy, I. E. Sakharov, "Plasma physics basis" (in Russian), 2011
15. "Plasma Physics: an Introductory Course", edited by R. O. Dendy, Cambridge University Press, 1993
16. G. Van Oost and R. Jaspers, "Thermonuclear burn criteria", Trans. Fusion Sci. Technol., February 2012 – Vol. 61, No. 2T, Proceedings of the Tenth Carolus Magnus Summer School on Plasma and Fusion Energy Physics, September, 4-16, 2011, Weert, The Netherlands
17. J. D. Lawson, "Some Criteria for a Power Producing Thermonuclear Reactor", Proceedings of the Physical Society B, Volume 70, p. 6, 1957
18. J. Lindl, "Development of the indirect-drive approach to inertial confinement fusion and the target physics basis for ignition and gain", Phys. Plasmas 2, 3933, 1995
19. J. D. Lindl et al., "The physics basis for ignition using indirect-drive targets on the National Ignition Facility", Phys. Plasmas 11, 339, 2004
20. J. Ongena and A. M. Messiaen, "Heating, Confinement and Extrapolation to Reactors", Trans. Fusion Sci. Technol. 49, 2T, 425, 2006
21. W. M. Stacey, "Fusion. An Introduction to Physics and Technology of Magnetic Confinement Fusion. Second, Completely Revised and Enlarged Edition", WILEY-VCH Verlag Gmbh&Co. KGaA, Weinheim, 2010

22. L. Spitzer, Jr., "A Proposed Stellarator", PM-S-l, USAEC NYO- 993, 1951
23. I. E. Tamm,"Theory of the magnetic thermonuclear reactor, part 1", Plasma Physics and the Problem of Controlled Thermonuclear Reactions (transl), New York: Pergamon, pp 3–19, 1959
24. A. D. Sakharov, "Theory of magnetic thermonuclear reactor, part 2", Plasma Physics and the Problem of Controlled Thermonuclear Reactions (transl), New York: Pergamon, pp 20–30, 1959
25. I. E. Tamm, "Theory of magnetic thermonuclear reactor, part 3", Plasma Physics and the Problem of Controlled Thermonuclear Reactions (transl), New York: Pergamon, pp 31–41, 1959
26. V. P. Smirnov, "Tokamak foundation in USSR/Russia 1950–1990", Nucl. Fusion 50 014003 8pp, 2010
27. L. A. Artzimovich, "Controlled Thermonuclear Reactions" (in Russian), 1963
28. S. Yu. Lukianov, "Hot plasma and controlled nuclear fusion" (in Russian), M., 1975
29. B. B. Kadomtsev, "Tokamak plasma, a complex physical system", Institute of Physics Publishing, Bristol, 1992
30. Culham Centre for Fusion Energy, http://www.ccfe.ac.uk
31. All-the-World's Tokamaks, http://www.tokamak.info
32. National Research Centre "Kurchatov Institute", http://www.kiae.ru
33. Ioffe Physical-Technical Institute of the Russian Academy of Sciences, http://www.ioffe.ru
34. Commissariat à l'Énergie Atomique (CEA) Cadarache, http://www.cea.fr/le-cea/les-centres-cea/cadarache
35. EAST tokamak homepage, http://english.hf.cas.cn/ic/ip/east
36. KSTAR tokamak homepage, http://www.nfri.re.kr
37. Japan Atomic Energy Agency, Naka Fusion Institute, http://www-jt60.naka.jaea.go.jp
38. B. Saoutic et al.,"Contribution of Tore Supra in preparation of ITER" Nucl. Fusion 51 094014, 2011
39. T. Kurki-Suonio et al., "Formation and detection of internal transport barriers in low-current tokamaks", Plasma Phys. Control. Fusion 44 301–323, 2002
40. D. V. Kouprienko et al., "Dynamics of the Electron Thermal Diffusivity at Improved Energy Confinement during Lower Hybrid Plasma Heating in the FT-2 Tokamak", Plasma Physics Reports, Vol. 36, No. 5, pp. 371–380, 2010
41. S. I. Lashkul et al., "Effect of the Radial Electric Field on Lower Hybrid Plasma Heating in the FT-2 Tokamak", Physics Reports, Vol. 27, No. 12, pp. 1001–1010, 2001
42. S. I. Lashkul et al.,"Analysis of the Efficiency of Lower Hybrid Current Drive in the FT-2 Tokamak", Plasma Physics Reports, Vol. 36, No. 9, pp. 751–761, 2010
43. V. N. Budnikov and M. A. Irzak, "Mechanism of ion and electron LH heating on the FT-2 tokamak", Plasma Phys. Control. Fusion 12A A135, 1996
44. V. N. Budnikov, V. V. D'yachenko, L. A. Esipov et al., "Improved confinement by lower-hybrid heating in the FT-2 tokamak", JETP Lett. 59, 685, 1994
45. European Fusion Development Agreement, http://www.efda.org
46. ITER official website, http://www.iter.org
47. P. Hennequin et al., "Scaling laws of density fluctuations at high-k on Tore Supra", Plasma Phys. Control. Fusion. 46 B121, 2004

48. A. Gurchenko and E. Gusakov, "Evolution of ETG mode scale turbulence and anomalous electron transport in dynamic tokamak experiments", Plasma Phys. Control. Fusion. 52 124035, 2010
49. S.-I. Itoh, "Project Review Plasma Turbulence - Structure Formation, Selection Rule, Dynamic Response and Dynamics Transport" (in Japaneese), J. Plasma Fusion Res. 86 334, 2010
50. S. Inagaki et al., "Observation of Long-Distance Radial Correlation in Toroidal Plasma Turbulence", Phys. Rev. Lett. 107 115001, 2011
51. P. A. Politzer, "Observation of Avalanchelike Phenomena in a Magnetically Confined Plasma", Phys. Rev. Lett. 84 1192, 2000
52. A. Fujisawa et al., "Identification of Zonal Flows in a Toroidal Plasma", Phys. Rev. Lett. 93 165002, 2004
53. T. Yamada et al., "Anatomy of plasma turbulence", Nature Phys. 4 721-725, 2008
54. P. Diamond et al., "Zonal flows in plasma—a review", Plasma Phys. Control. Fusion 47 3 R35, 2005
55. A. Fujisawa, "A review of zonal flow experiments", Nucl. Fusion 49 013001, 2009
56. N. Bretz, "Diagnostic instrumentation for microturbulence in tokamaks", Rev. Sci. Instrum. 68 8, 1997
57. D. W. Ross, Commenta Plasma Phys. Control Fusion XII 155, 1989
58. D. W. Ross, "On standard forms for transport equations and quasilinear fluxes", Plasma Phys. Control. Fusion 34 137, 1992
59. W. Horton and R. D. Estes, "Anomalous drift-wave transport analysis of tokamak discharges", Nucl. Fusion 19 203, 1979
60. L. Spitzer, Jr., "Particle Diffusion across a Magnetic Field", Phys. Fluids 3 659, 1960
61. B. B. Kadomtsev and O. P. Pogutse, "Theory of electron transport in a strong magnetic field", JETP Lett. 39 269, 1984
62. D. R. Thayer and P. H. Diamond, "Thermally driven convective cells and tokamak edge turbulence", Phys. Fluids 30 3724, 1987
63. R. Sabot et al., "Measurements of density profile and density fluctuations in Tore Supra with reflectometry", Proc. 20th IAEA Fusion Energy Conference 1st-6th November 2004, Villamoura, Portugal EX/P6-25
64. W. Horton, "Drift waves and transport", Rev. Modern Physics 71 735, 1999
65. Z. Lin et al., "Size Scaling of Turbulent Transport in Tokamak Plasmas", Phys. Rev. Lett. 88 195004, 2002
66. L. Vermare et al., "Wavenumber spectrum of micro-turbulence in tokamak plasmas", C R Physique 12 115-122, 2011
67. P. H. Diamond, S.-I. Itoh and K. Itoh, "Modern Plasma Physics. Volume 1: Physical Kinetics of Turbulent Plasmas", Cambridge University Press, 2010
68. A. N. Kolmogorov, Dokl. Akad. Nauk SSSR 30 301, 1941, (reprinted in Proc. R. Soc. Lond. A434 9, 1991)
69. A. N. Kolmogorov, Dokl. Akad. Nauk SSSR 32 16, 1941, (reprinted in Proc. R. Soc. Lond. A434 15, 1991)
70. R. H. Kraichnan, "Inertial Ranges in Two-Dimensional Turbulence", Phys. Fluids 10 1417, 1967

71. G. Boffetta, A. Celani, S. Musacchio and M. Vergassola, "Intermittency in two-dimensional Ekman-Navier-Stokes turbulence", Phys. Rev. E 66 026304, 2002
72. R. H. Kraichnan, "Inertial-range transfer in two- and three-dimensional turbulence", J. Fluid Mech. 47 525, 1971
73. N. Bretz, "One-dimensional modeling of the wavelength sensitivity, localization, and correlation in reflectometry measurements of plasma fluctuations", Physical Fluids B4(8) 2414, 1992
74. E. Mazzucato, "Small-Scale Density Fluctuations in the Adiabatic Toroidal Compressor", Phys. Rev. Lett. 36 792, 1976
75. R. E. Slusher and C. M. Surko, "Study of density fluctuations in plasmas by small-angle CO_2 laser scattering", Phys. FIuids 23 472, 1980
76. N. Bretz et al., Proc. 17th European Conference on Controlled Fusion and Plasma Physics, Amsterdam, 1990 edited by K. Bethge (EPS, Petit-Lancy, Switzerland 1990),Vol. IV, p. 1544
77. G. Leclert et al., "Full-wave test of the radial correlation reflectometry analytical theory in linear and nonlinear regimes", Plasma Phys. Control. Fusion 48 1389, 2006
78. C. Fanack et al., "Ordinary-mode reflectometry: modification of the scattering and cut-off responses due to the shape of localized density fluctuations", Plasma Phys. Control Fusion 38 1915-1930, 1996
79. F. Wagner et al., "Regime of Improved Confinement and High Beta in Neutral-Beam-Heated Divertor Discharges of the ASDEX Tokamak", Phys. Rev. Lett. 49 1408, 1982
80. S.-I. Itoh and K. Itoh, "Model of L to H-Mode Transition in Tokamak", Phys. Rev. Lett. 60 2276, 1988
81. H. Biglari, P. H. Diamond and P. W. Terry, "Influence of sheared poloidal rotation on edge turbulence", Phys. Fluids B2 1, 1990
82. F. Chen, "Plasma Diagnostic Techniques", edited by R. H. Huddleston and S. L. Leonard, Academic, New York, p. 113, 1975
83. P. Staib, "Probe measurements in the plasma boundary layer", J. Nucl. Mater. 111&112, 109, 1982
84. I. Hutchinson, "Principles of Plasma Diagnostics", Second Edition, Cambridge University Press, 2002
85. M. Stanojevic et al., "Fluid model of the magnetic presheath in a turbulent plasma", Plasma Phys. Contr. Fusion 47 (2005) 685
86. R. L. Hickok, IEEE Trans. Nucl. Sci. NS-28 18, 1981
87. Yu. N. Dnestrovskii, L. I. Krupnik, A. V. Mel'nikov and I. S. Nedsel'skii, Sov. J. Plasma Phys. 12 130, 1986
88. L. I. Krupnik and V. I. Tereshin, Plasma Phys. Rep. 20 146, 1994
89. R. C. Isler, "An overview of charge-exchange spectroscopy as a plasma diagnostic", Plasma Phys. Control. Fusion 36 171, 1994
90. R. Cano and A. Cavallo, Proceedings of the 5th International Conference on Infrared and Millimeter Waves, Wurtzburg (1980)
91. F. Simonet, "Etude de la réflectométrie hyperfréquence en modes ordinaire et extraordinaire pour la mesure du profil radial et des fluctuations locales de la densité electronique dans les tokamaks", PhD thesis, Université de Nancy I, 1985
92. V. L. Ginzburg, "The Propagation of Electromagnetic Waves in Plasmas", Pergamon, Oxford, 1964
93. A. I. Anisimov et al., Soviet Phys. Technical Phys. 5 9, 1961

94. R. J. Colchin ORMAK Technical Memo 93/105, 1973
95. I. Hutchinson, "One-dimensional full-wave analysis of reflectometry sensitivity and correlations", Plasma Phys. Control. Fusion 34 1225, 1992
96. A. E. Costley et al., "Recent developments in microwave reflectometry at JET (invited)", Rev. Sci. Instr. 61 2823, 1990
97. M. Gilmore, W. A. Peebles, X. V. Nguyen, "Investigation of dual mode (O-X) correlation reflectometry for determination of magnetic field strength", Plasma Phys. Control. Fusion 42 655, 2000
98. E. Mazzucato and R. Nazikian, "Radial scale length of turbulent fluctuations in the main core of TFTR plasmas", Phys. Rev. Lett. 71 1840, 1993
99. G. D. Conway et al., "Fluctuation and reflectometer simulation studies on ASDEX Upgrade", 5th Intl. Reflectometry Workshop, IRW5 NIFS Japan, March 5th-7th, 2001
100. E. Gusakov and A. Surkov, "Spatial and wave number resolution of Doppler reflectometry", Plasma Phys. Control. Fusion **46** (2004) 1143
101. E. Z. Gusakov, A. V. Surkov and A. Yu. Popov, "Multiple scattering effect in Doppler reflectometry", Plasma Phys. Control. Fusion 47 959, 2005
102. A. Yu. Popov, E. Z. Gusakov, "Spatial Resolution of Poloidal Correlation Reflectometry", 32nd EPS Conference on Plasma Phys. Tarragona, 27 June - 1 July 2005 ECA Vol.29C P-1.088, 2005
103. V. A. Vershkov et al., "Direct Comparison of Turbulence Measurements with Langmuir Probes and Reflectometry at the same Radial Locations in T-10 and Reflectometry Simulations with 2D Full-Wave Code", Proc. 30th Conf. Control. Fusion Plasma Phys. ECA Vol. 27A P-2.56, 2003
104. E. Z. Gusakov and A. Yu. Popov, "Measurements localization in poloidal correlation reflectometry", Nucl. Fusion 46 S829–S835, 2006
105. Y. Lin et al., "Plasma curvature effects on microwave reflectometry fluctuation measurements", Plasma Phys. Control. Fusion 43 L1, 2001
106. R. Nazikian et al., "Measurement of Turbulence Decorrelation during Transport Barrier Evolution in a High-Temperature Fusion Plasma", Phys. Rev. Lett. 94 135002, 2005
107. E. Gusakov and B. Yakovlev, "Two-dimensional linear theory of radial correlation reflectometry diagnostics", Plasma Phys. Control. Fusion 44 2525, 2002
108. G. J. Kramer et al., "Correlation reflectometry for turbulence and magnetic field measurements in fusion plasmas (invited)", Rev. Sci. Instrum. 74 1421, 2003
109. E. Gusakov, V. Bulanin, O. Rozhdestvensky, "Modelling of Radial Correlation Reflectometry in Cylinder Geometry", Proc. of 3rd France-Russian Seminar NAMES 2007 Metz EDP Sciences 133, 2008
110. E. Gusakov and A. Popov, "Non-linear theory of fluctuation reflectometry", Plasma Phys. Control. Fusion 44 2327, 2002
111. E. Gusakov and A. Popov, "Two-dimensional non-linear theory of radial correlation reflectometry", Plasma Phys. Control. Fusion 46 1393, 2004
112. International Atomic Energy Agency, Conference Proceedings, http://www-naweb.iaea.org/napc/physics/PS/conf.htm

113. E. Mazzucato, "Microwave reflectometry for magnetically confined plasmas", Rev. Sci. Instrum. 69 2201, 1998
114. H. Bindslev, "Dielectric effects on Thomson scattering in a relativistic magnetized plasma", Plasma Phys. Control. Fusion 33 1775, 1991
115. B. B. Afeyan, A. E. Chou, B. I. Cohen, "The scattering phase shift due to Bragg resonance in one-dimensional fluctuation reflectometry", Plasma Phys. Control. Fusion 37 315, 1994
116. F. da Silva, "Studies on O-mode reflectometry spectra simulations with velocity shear layer", Nucl. Fusion 46 S816–S823, 2006
117. L. D. Landau and E. M. Lifshitz, "Quantum Mechanics" (in Russian), 1963
118. A. B. Migdal, "Qualitative methods in quantum theory" (in Russian), M. Nauka, 1975
119. M. Abramovitz and I. Stegun, "Handbook of Mathematical Functions with Formulas, Graphs, and Mathematical Tables", New York: Dover Publications, 1970
120. H. Bottolier and G. Ichtchenko, "Microwave reflectometry with the extraordinary mode on tokamaks: Determination of the electron density profile of Petula-B", Rev. Sci. Instrum. 58 539, 1987
121. F. Clairet et al., "Fast sweeping reflectometry upgrade on Tore Supra", Rev. Sci. Instrum. 81 10D903, 2010
122. A. D. Piliya and A. Yu. Popov, "On application of the reciprocity theorem to calculation of a microwave radiation signal in inhomogeneous hot magnetized plasmas", Plasma Phys. Control. Fusion 44 467, 2002
123. L. D. Landau and E. M. Lifshitz, "Electrodynamics of Continuous Media", Oxford: Pergamon, 1981
124. J. Murray, "Asymptotic Analysis", New York: Springer, 1984
125. S. Heuraux et al., "Radial wave number spectrum of density fluctuations deduced from reflectometry phase signals", Rev. Sci. Instrum. 74 1501, 2003
126. E. Gusakov and M. Tyntarev, "The two-dimensional theory of reflectometry diagnostics of plasma fluctuations", Fusion Engineering and Design 34-35 501-505, 1997
127. A. Gurchenko et al., "Observation of the ETG mode component of tokamak plasma turbulence by the UHR backscattering diagnostics", Nucl. Fusion 47 245–250, 2007
128. R. Sabot et al., "Advances of reflectometry on Tore-Supra: from edge density profile to core density fluctuations", Int. J. Infrared Millim. Waves 25 229–46, 2004
129. A. Gurchenko et al., "Observation of turbulence exponential wave number spectra at ion sub-Larmor scales in FT-2 tokamak", Plasma Phys. Control. Fusion 52 035010, 2010
130. E. Blanco, T. Estrada and T. Happel, "Study of radial correlation reflectometry using a 2D full-wave code", Proc. of 9th International Reflectometry Workshop (IRW9) Lisbon, Portugal, 4th - 6th May 2009
131. E. J. Doyle et al., "Demonstration of ITER operational scenarios on DIII-D", Nucl. Fusion 50 075005, 2010
132. M. Gilmore et al., Letter to the editor "Detailed comparison of plasma turbulence correlation length measurements using microwave reflectometry and a Langmuir probe array", Plasma Phys. Control. Fusion 42 L1–L7, 2000

133. F. Clairet et al., "New signal processing technique for density profile reconstruction using reflectometry", Rev. Sci. Instrum. 82, 083502, 2011
134. P. Hennequin et al., "Doppler backscattering system for measuring fluctuations and their perpendicular velocity on Tore Supra", Rev. Sci. Instrum., 75(10): 3881-3883, 2004
135. A. Sirinelli et al., "Density and fluctuation profiles obtained with the D-band reectometer in Tore-Supra", Proc. of 7th International Reflectometry Workshop 4-6 May 2007 Saint-Petersburg, Russia
136. M. Kramer et al., "Anomalous helicon wave absorption and parametric excitation of electrostatic fluctuations in a helicon-produced plasma", Plasma Phys. Control. Fusion 49 A167–A175, 2007
137. A. Altukhov et al., "Turbulence wave number spectra reconstruction from radial correlation reflectometry data at FT-2 tokamak", Proc. of the 39th EPS Conference on Plasma Physics, Vol.36F, P4.092, 2012
138. L. Meneses, Group meeting talk 10/02/2012 Culham, UK
139. General Atomics Fusion Theory and Computational Sciences, https://fusion.gat.com/theory/Efithistory
140. E. Gusakov et al., "Reflectometry diagnostics operation limitations caused by strong Bragg back scattering", Proc. of the 37th EPS Conference on Plasma Physics, Vol. 34A, P5.110, 2010
141. K. Syisoeva, "Propagation of electromagnetic waves in turbulent inhomogeneous plasma" (in Russian), Master thesis, Saint-Petersburg State Polytechnical University, 2012

Publications

1. Papers:

1.1. N. Kosolapova, E. Gusakov and S. Heuraux,
"Numerical modeling of microturbulence wave number spectra reconstruction using radial correlation reflectometry: I. O-mode reflectometry at the linear plasma density profile",
Plasma Phys. Control. Fusion 54 (2012) 035008, doi: 10.1088/0741-3335/54/3/035008

1.2. E. Gusakov and N. Kosolapova,
"Fluctuation reflectometry theory and the possibility of turbulence wave number spectrum reconstruction using the radial correlation reflectometry data",
Plasma Phys. Control. Fusion 53 (2011) 045012, doi: 10.1088/0741-3335/53/4/045012

1.3. S. Heuraux, F. da Silva, E. Gusakov, A. Popov, E. Beauvier, N. Kosolapova and K. Syisoeva,
"Reflectometry Simulations on Different Methods to Extract Fusion Plasma Turbulence Characteristics and Its Dynamics",
Contrib. Plasma Phys. 51, No. 2-3, (2011) 126–130, doi: 10.1002/ctpp.201000050

1.4. N. Kosolapova, K. Itoh, S.-I. Itoh, E. Gusakov, S. Heuraux, S. Inagaki, M. Sasaki,
T. Kobayashi, Y. Nagashima, S. Oldenbürger, A. Fujisawa,
"On turbulence-correlation analysis based on correlation reflectometry",
submitted to Phys. Scripta

2. Conference proceedings:

2.1. N. Kosolapova, A. Altukhov, A. Gurchenko, E. Gusakov , S. Heuraux, R. Sabot, F. Clairet,
"Turbulence wave number spectra reconstruction from radial correlation reflectometry data at Tore Supra and FT-2 tokamaks", // 24th IAEA Fusion Energy Conference, October 8-13, 2012, San Diego, California, USA

2.2. A. Altukhov, A. Gurchenko, E. Gusakov, N. Kosolapova, S. Leerink, L. Esipov,
"Turbulence wave number spectra reconstruction from radial correlation reflectometry data at FT-2 tokamak", // 39th EPS Conference on Plasma Phys. Strasbourg, 2-6 July 2012, ECA Vol. 36F, P4.092 (2012) (4pp), http://ocs.ciemat.es/EPSICPP2012PAP/pdf/P4.092.pdf

2.3. E. Gusakov, N. Kosolapova and S. Heuraux,
“Modeling of the turbulence wave number reconstruction using radial correlation reflectometry data with applications to FT-2, JET, Tore Supra like cases”, // 39th Conference on plasma physics and controlled fusion, Zvenigorod (Moscow reg.), February 6—10, 2012

2.4. E. Gusakov, N. Kosolapova and S. Heuraux,
“On possibility of turbulence wave number spectra reconstruction using radial correlation reflectometry in Tore Supra and FT-2 tokamaks”, // 38th EPS Conference on Plasma Phys., Strasbourg, 27 June – 1 July, 2011, ECA Vol. 35G, P2.060 (2011) (4pp),
http://ocs.ciemat.es/EPS2011PAP/pdf/P2.060.pdf

2.5. E. Gusakov, N. Kosolapova and S. Heuraux,
“On possibility of turbulence wave number spectra reconstruction using radial correlation reflectometry in Tore Supra and FT-2 tokamaks”, // 10th International Reflectometry Workshop (IRW10), Padova, Italy, 4th-6th May 2011, proceedings (6pp),
http://www.igi.cnr.it/irw10/proceedings/KosolapovaNV.pdf

2.6. E. Gusakov, N. Kosolapova and S. Heuraux,
“Numerical modelling of tokamak plasma microturbulence wave number spectrum reconstruction using radial correlation reflectometry data”, // New Achievements in Materials and Environmental Sciences (NAMES 2010) Nancy, France October 27-29, 2010, to be published in Journal of Physics: Conference Series (JPCS)

2.7. S. Heuraux, F. da Silva, E. Gusakov, A. Popov, N. Kosolapova, K.V. Syisoeva,
"Numerical modeling of tokamak plasma microturbulence wave number spectrum reconstruction using radial correlation reflectometry data", // New Achievements in Materials and Environmental Sciences (NAMES 2010) Nancy, France October 27-29, 2010, to be published in Journal of Physics: Conference Series (JPCS)

2.8. E. Gusakov, N. Kosolapova and S. Heuraux,
“Numerical modelling of microturbulence wave number spectra reconstruction using radial correlation reflectometry data”, // International Conference on Plasma Diagnostics, April 12-16, 2010, Pont-à-Mousson, France,http://plasma2010.ijl.nancy-universite.fr

2.9. E. Gusakov, N. Kosolapova and S. Heuraux,
“Numerical modelling of microturbulence wave number spectra reconstruction using radial correlation reflectometry data”, // 37th Conference on plasma physics and controlled fusion,

Zvenigorod (Moscow reg.), February 8—12, 2010

2.10. E. Gusakov, N. Kosolapova and S. Heuraux,
"Procedure of the turbulence wave number spectra reconstruction using the radial correlation reflectometry data", // 9th International Reflectometry Workshop (IRW9), Lisbon, Portugal, 4th-6th May 2009, proceedings (7pp), http://www.ipfn.ist.utl.pt/irw9/papers/egusakov_paper.pdf

2.11. E. Gusakov, N. Kosolapova and S. Heuraux,
"Modelling of the turbulence wave number spectra reconstruction from the radial correlation reflectometry data", // 36th EPS Conference on Plasma Phys., Sofia, June 29 - July 3, 2009, ECA Vol.33E, P-4.217 (2009) (4pp), http://epsppd.epfl.ch/Sofia/pdf/P4_217.pdf

2.12. E. Gusakov, N. Kosolapova and S. Heuraux,
"Numerical modeling of microturbulence wave number spectra reconstruction using radial correlation reflectometry data", // 36th Conference on plasma physics and controlled fusion, Zvenigorod (Moscow reg.), February 9—13, 2009

2.13. E. Gusakov, N. Kosolapova and S. Heuraux,
"Turbulence wave number spectra reconstruction using radial correlation reflectometry", // 35th EPS Conference on Plasma Phys. Hersonissos, 9 - 13 June 2008 ECA Vol.32D, P-1.082 (2008) (4pp), http://epsppd.epfl.ch/Hersonissos/pdf/P1_082.pdf

2.14. E. Gusakov, V. Bulanin, O. Rozhdestvenskiy, N. Kosolapova,
"On possibility of turbulence wave number spectra reconstruction using radial correlation reflectometry data", // 34th EPS Conference on Plasma Phys. Warsaw, 2 - 6 July 2007 ECA Vol.31F, P-5.100 (2007) (4pp), http://epsppd.epfl.ch/Warsaw/pdf/P5_100.pdf

2.15. E. Gusakov, V. Bulanin, O. Rozhdestvenskiy, N. Kosolapova,
"On possibility of turbulence wave number spectra reconstruction using radial correlation reflectometry data", // 8th International Reflectometry Workshop (IRW9), Saint-Petersburg, Russia, 2nd-4th May 2007, proceedings (8pp),
http://plasma.ioffe.ru/irw8/proceedings/Gusakov_paper.pdf

Awards

Oct. 2011

Grant of Russian Ministry of Education (Order #2477 14.10.2011)

Jul. 2011

Winner of the 7th Itoh Project Prize in Plasma Turbulence at the 38th European Physical Society Conference on Plasma Physics, 27th June – 1st July 2011, Strasbourg, France

May 2010

Awarded the medal "For the best scientific work" of students of Universities of the Russian Federation and the CIS countries (Order #470 27.05.2010)

Acknowledgements

During the three years of my work on the thesis I have taken efforts in this project, however it would not have been possible without the kind support and help of a large number of people. I would like to thank all of them.

First of all I would like to express my profound gratitude and deep regards to Professor Stéphane Heuraux and Professor Evgeniy Gusakov, my research supervisors, for their patient guidance, enthusiastic encouragement and useful critiques; their valuable and constructive suggestions during the planning and development of this research work. Their willingness to give their time so generously has been very much appreciated.

I would like to thank the Administration and staff of Institute Jean Lamour, Université de Lorraine; Nancy, France and Ioffe Institute, Saint-Petersburg, Russia for the great opportunity to work on the thesis as a student of two countries.

I wish to thank the FT-2 tokamak team, especially Aleksey Altukhov and Aleksey Gurchenko for providing me with results of reflectometry experiments, for detailed explanations and enlightening discussions.

I am highly indebted to Roland Sabot for giving me a great opportunity to work with him on Tore Supra and JET reflectometry experiments.

Without explanations of Antoine Sirinelli I would not have managed to perform my work at JET reflectometers and obtain required data.

Thanks to Frédéric Clairet who has thoughtfully revised my papers and gave me essential advices.

I would like to thank Jean-Claude Giacalone and Sébastian Hacquin for all their valuable assistance in the experimental work.

I am also grateful to all the staff of Tore Supra and JET tokamaks for helping me to participate in experiments and feel comfortable during my work there.

I am obliged to Filipe da Silva for his significant help with numerical computations performed in 2D.

I highly appreciate the invitation of Professor Sanae-I. Itoh and Professor Kimitaka Itoh to visit Kyushu University and National Institute for Fusion Science in Japan. This visit became a great discovery for me and the reception I recived was exceptionally warm. I would like also to thank Stella Oldenbürger, Shigeru Inagaki and all the members of Itoh Plasma Turbulence Laboratory for their help and collaboration during my stay in Japan.

I would like to thank Roger Jaspers, Greg de Temmerman, Tony Donné and all 10th Carolus Magnus Summer School team for great organization of education process and time spent during two weeks in September 2011 in Weert, the Netherlands.

I could not manage to complete the work without the invaluable support of my beloved parents and family.

I would like to express my heartfelt thanks to my husband Dmitry. Your faith and loving patience colored my life and made me feel your support through distance and time.

Natalia Kosolapova,

16th of November, 2012